Velocity and Q from reflection seismic data

by

Berkan G. Ecevitoglu

Dissertation submitted to the Faculty of the

Virginia Polytechnic Institute and State University

in partial fulfillment of the requirements for the degree of

Doctor of Philosophy

in

Geophysics

APPROVED:

John K. Costain, Chairman

G. A. Bollinger

Cahit Çoruh

Edwin S. Robinson

J. Arthur Snoke

July, 1987

Blacksburg, Virginia

Department of Geological Sciences

Virginia Polytechnic Institute and State University
Blacksburg, VA 24061

14 July 1987

MEMORANDUM

TO: The Graduate School, Virginia Tech

FROM: Arthur Snoke, Ecevitoglu's Dissertation Committee Member

SUBJECT: Letter of Dissent on Ecevitoglu's Dissertation

Berkan Ecevitoglu's PhD dissertation, titled ***Velocity and Q from reflection seismic data***, introduces some novel concepts and techniques which may eventually evolve into improved methods to estimate crustal attenuation from seismic reflection data. Of particular interest are his methods for extracting and utilizing waveform distortion or, equivalently, phase. However, because of inaccuracies and incompleteness in the theoretical sections of the dissertation providing the background and/or justifying his techniques, I am writing this letter of dissent to be included with the dissertation. My specific objections are that he misrepresents the current theory of anelastic attenuation (caused, I believe, by an imperfect comprehension of that theory); he mistakenly applies "periodic" Fourier theory in his analysis of attenuation; and there are fundamental errors in his development of the technique to determine attenuation in the time domain. I elaborate on these points in the following paragraphs.

From both the abstract and the body of the dissertation one gets the impression that there are inadequacies in the present theory of anelastic attenuation in the earth that Ecevitoglu's approach addresses and overcomes. Specifically he mentions that "the selection of arbitrary constants and cutoff frequencies are no longer necessary" in his treatment, and on page 6 he includes a quote from the textbook by Aki and Richards which is intended to demonstrate problems with the current theory. This is an erroneous interpretation both of the current theory and of Aki and Richards' presentation of that theory.

Anelastic attenuation in the earth can be viewed as a causal, minimum-phase filter. The physical mechanisms acting are not completely understood, and the effects of this filter can be measured over only a limited frequency range, the seismic band which, including all data, runs from less than 0.001 Hz to about 100 Hz. To a first approximation, the amplitude attenuation is linear over that range--at least for any single experiment, which necessarily covers only a small portion of that band. Attenuation is therefore usually modeled as a low pass filter with a "constant Q". We have no direct evidence of what the attenuation is outside that band, and the quote from Aki and Richards notes the difficulty of making the simplest mathematical assumption: that Q is constant for all frequencies. Ecevitoglu makes a big point about the problem of the current theory because it results in an unbounded phase as frequencies approach infinity. However, all physical models included among their references (e.g., Futterman (1962) and subsequent pages to the quoted passage in Aki and Richards) note that the attenuation must go to zero at both frequency extremes. An unbounded phase at infinite frequency would imply an extremely unphysical infinite wave speed. On page 10 Ecevitoglu mentions a paper by Liu et al. (1976) as having developed, from physical models, analytic expressions for the amplitude and phase for attenuation which is approximately constant over a finite band. The only "problem" anyone has found with that model in the

lst ten years is the limits of the band and whether or not Q has some small frequency dependence over some parts of that band.

My next point is that Ecevitoglu exhibits an incomplete understanding of concepts such as *causality*, *minimum phase* and the appropriate conditions for applying "periodic" Fourier theory. As an example of his confusion regarding the first two terms, on the bottom of page 99 he says that "although the pulse is now minimum delay, it is no longer causal." In all definitions I have seen, "minimum delay" is a subset of causal.

Ecivitoglu uses periodic Fourier theory erroneously in two ways: he mistakenly asserts that truncation in the frequency domain solves the problem cited in his quote from Aki and Richards about how a constant Q at all frequencies leads to a violation of the Paley-Wiener criterion, and he assumes that one can use the periodic theory version of the Hilbert transform to calculate the amplitude from the phase (or vice versa) for the attenuation filter.

When one uses discrete data, one must use numerical techniques to process the data. If the seismic signal before recording can be thought of as the convolution of minimum phase filters, digitizing and truncating that signal (that is, recording it) result in a function that is not minimum phase but only an approximation of a minimum phase function. If one wants to derive amplitudes from phases, or vice versa, one works with what you have, not with artificially created functions which are minimum phase. All numerical methods for calculating Hilbert Transforms are not equivalent in all cases. Using the periodic transform method, as he does, implicitly assumes that the function is periodic with a period of twice the Nyquist. The attenuation filter is not such a function. For some functions which are not periodic the Fourier Hilbert transform works adequately; for those cases the function is effectively zero except in a finite region far from the Nyquist. For some functions, perhaps including an approximately linear attenuation, there are simple relationships between the "real" phase and that derived by taking the periodic Hilbert transform of the log of the amplitude. Ecevitoglu's demonstration of this for both the Brune pulse and Futterman's pulse in Appendix 1 demonstrate this, and this observation may be one of the more important things to come out of this project. However, the way the technique is presented is incorrect. The following statement from page 25 is simply wrong: "The difference between discrete and continuous Hilbert transformation is then the finiteness versus the infiniteness of the process."

The final point I will address is the discussion on pages 21-23 on the proposed method to determine Q from time-domain measurements. The equation at the bottom of page 21 relating the phase velocities at zero frequency and the Nyquist simply has to be wrong. It says that the phase velocity at the Nyquist depends only on the phase velocity at zero frequency and the constant Q. This is inconsistent with dispersion because it implies that the phase velocity is independent of frequency because one gets the same answer if one changes the Nyquist frequency. When I raised this question at the (5 1/2 hour) defense, I was told that the phase velocities in this expression were not the "usual" definition. However, the comparisons on page 22 with other studies presumably used the conventional definitions. Furthermore, the dispersive time delay, ΔW , as defined on page 22 cannot in general be related simply to pulse broadening in the time domain. And finally, on page 37 the prescription given for measuring pulse broadening is probably invalid: It is stated that one measures peak-to-peak or trough-to-trough the input and output wavelets and takes the difference. That is not the complete pulse width, nor do they show how that measurement is related to their ΔW.

Velocity and Q from reflection seismic data

by

Berkan G. Ecevitoglu

John K. Costain, Chairman

Geophysics

(ABSTRACT)

This study has resulted in the discovery of an exact method for the theoretical formulation of the effects of intrinsic damping where the attenuation coefficient, $\alpha(\nu)$, is an arbitrary function of the frequency, ν. Absorption-dispersion pairs are computed using numerical Hilbert transformation; approximate analytical expressions that require the selection of arbitrary constants and cutoff frequencies are no longer necessary. For constant Q, the dispersive body wave velocity, $p(\nu)$, is found to be

$$p(\nu) = \frac{p(\nu_N)}{1 + \frac{1}{2Q}\frac{H(-\nu)}{\nu}} \tag{1}$$

where H denotes numerical Hilbert transformation, $p(\nu)$ is the phase velocity at the frequency ν, and $p(\nu_N)$ is the phase velocity at Nyquist. From (1) it is possible to estimate Q in the time domain by measuring the amount of increase, ΔW, of the wavelet breadth after a traveltime, $\Delta\tau$, by

$$Q = \frac{2\Delta\tau}{\pi\Delta W} \tag{2}$$

The inverse problem, i.e., the determination of Q and velocity is also investigated using singular value decomposition (SVD). The sparse matrices encountered in the acquisition of conventional reflection seismology data result in a system of linear equations of the form $AX = B$, with A the design matrix, X the solution vector, and B the data vector. The system of normal equations is $A^TAX = A^TB$ where the least-squares estimate of $X = \hat{X} = V\frac{1}{S}U^TB$ and the SVD of A is $A = USV^T$. A technique to improve the sparsity pattern prior to decomposition is described.

From an application of equation (2) using reference reflections from shallower reflectors, crystalline rocks in South Carolina over the depth interval from about 5 km to 10 km yield values of Q in the range $Q = 250 - 300$.

Non-standard recording geometries ("Q-spreads") and vibroseis recording procedures are suggested to minimize matrix sparseness and increase the useable frequency bandwidth between zero and Nyquist. The direct detection of body wave dispersion by conventional vibroseis techniques may be useful to distinguish between those crustal volumes that are potentially seismogenic and those that are not. Such differences may be due to variations in fracture density and therefore water content in the crust.

ACKNOWLEDGEMENTS

Financial support was provided during academic year 1985-86 by NSF Grant EAR-8420858 to J. K. Costain, and by a Conoco Fellowship during academic year 1986-87. Support for six weeks during the summer of 1987 was provided by NRC Contract NRC-04-85-106 to Lynn Glover, III, J. K. Costain, C. Çoruh, and G. A. Bollinger.

TABLE OF CONTENTS

LIST OF ILLUSTRATIONS

LIST OF TABLES

INTRODUCTION AND PURPOSE OF STUDY

The most commonly used measures of attenuation in rocks are the attenuation coefficient, $\alpha(\nu)$, the quality factor, Q, its inverse 1/Q (internal friction or dissipation factor), and the logarithmic decrement, δ. Generally speaking, except for unconsolidated, water-saturated sediments, the specific dissipation constant, or quality factor, Q, is believed to be essentially independent of frequency and is related to the rate at which the mechanical energy of vibration is converted irreversibly into heat. The definition of Q does not depend on the detailed mechanism by which the energy is dissipated (Waters, 1987). These quantities are related as follows:

$$\frac{1}{Q} = \frac{\alpha(\nu)p}{\pi\nu} = \frac{\delta}{\pi}$$

where p is velocity and ν is frequency in hertz.

Absorption is frequency dependent and may be computed from

$$A_2(\nu) = A_1(\nu)\, e^{-\alpha(\nu)\, a}$$

Then

$$\alpha(\nu) = -\frac{1}{a} \ln \left[\frac{A_2(\nu)}{A_1(\nu)}\right] \qquad (1)$$

where the knowns are the travel distance a and $A_1(\nu)$ and $A_2(\nu)$, the input-output amplitude spectra, respectively. For most rocks, a plot of $\alpha(\nu)$ versus ν appears to be linear with frequency (Knopoff

and MacDonald, 1958; Gutenberg, 1959; Gardner et al., 1964; Gordon and Davis, 1968; Pandit and Savage, 1973; Toksoz et al., 1979; Waters, 1987). The attenuation coefficient, α, may be expressed in nepers/unit length (or simply inverse length) or in dB/unit length. The relationship between the two is given by α(dB/unit length) = 8.686 α(nepers/unit length). Also, $\alpha(dB/\lambda) = 8.686\ \pi/Q$. Absorption must be accompanied by body wave dispersion so that causality can be satisfied. The consequences of causal and acausal absorption are shown in Figure 1.

If b is the slope of a least-squares fit of a straight line to the data computed from equation (1) then

$$\alpha(v)\, a = bv \tag{2}$$

The equation

$$\alpha(v) = \frac{\pi v}{Qp} \tag{3}$$

gives the relationship between the absorption coefficient and the quality factor Q. Here p stands for the body wave phase velocity. From (2) and (3)

$$a\, x = b \tag{4}$$

where

$$x = \frac{\pi}{Qp} \tag{5}$$

The desired unknown, x, is in fact the product of two other unknowns, i.e. the quality factor, Q, and the body wave phase velocity, p. As discussed below, values of b are weighted by equation (54). The matrix form of (4) will be one of the overdetermined systems of equations to be solved using SVD techniques.

The main problem in the determination of the Q lies in the fact that the true loss mechanism is difficult to separate out from other and often stronger damping mechanisms, such as geometric spreading, reflections transmissions, and scattering. For the near future it might be sufficient to use

only as a rough description of major crustal units, where internal reflection, transmission, and scattering losses may all still be incorporated in a rough "effective Q".

Time delays are introduced by highly attenuating rocks (Q = 20, say). These delays affect estimates of velocity and can influence a geologic interpretation (Angeleri and Loinger, 1984). Attenuation can also result from layering by a combination of transmission losses and intrabed multiples (O'Doherty and Anstey, 1971). Schoenberger and Levin (1974) reported that attenuation due to layering accounted for 30 - 50% of the total frequency dependent attenuation estimated from field seismograms at two well locations. Sherwood and Trorey (1965) showed the complete response of Shoenberger and Levin's isolated reflection has minimum phase property.

Recent interpretations of reflections from the base of the crust indicate layering near the M-discontinuity; this may affect determinations of values of Q at these lower depths. It would be necessary to correct for all of these effects to obtain the true intrinsic damping.

For completeness, we will also refer to the methods for the assessment of Q from surface waves, although they are hardly used for laboratory investigations (Meissner ,1986, p.158). Surface waves provide only average Q values for the whole crust and a certain region. In this methods Q is obtained from the coda of local earthquakes. The assumption is made that the dominant coda frequency is caused by surface wave scattering and is a function of the source spectrum, the instrument response, and the "Q-filter" of the crust (Herrmann, 1980). The effect of the source spectrum may be ignored if its corner frequency is greater then the peak instrument response, which is known. Aki (1969) proposed an empirical relationship between coda amplitudes, coda frequencies, and Q, and Herrmann (1980) provides some master curves for easy assessment.

The relative constancy of Q may not apply under the conditions of elevated temperature and pressure encountered in the interior of the earth. Solomon (1972) summarized some seismic evidence for frequency dependence of Q. This and the data of Takano (1971) and Yoshida and Tsujiura (1975) suggest that Q generally increases with frequency in the mantle. This trend is consistent with the results of Berckhemer et al. (1979) who observed creep in mantle peridotite at 1200 and 1300 °C which implies that Q has a power law dependence on frequency. Anderson and Minster (1979) demonstrated that Chandler wobble, tidal dissipation, and free oscillation data are

consistent with a power law dependence of Q on frequency. The model Q of Anderson and Hart (1978) assumes that Q is independent of frequency and shows acceptable agreement with body wave, surface wave, and free oscillation data.

The influence of small amounts of water has been extensively studied by Tittmann (1977) and Tittmann et al. (1980). The laboratory measurements of Q indicate that in sedimentary rocks, relaxation peaks for Q are found in saturated rock samples, while Q was much greater for dry samples (Spencer, 1981). For lunar rock samples under a high vacuum a Q of nearly 5000 was obtained, in agreement with the Q values from Apollo experiments on the lunar crust and mantle. A small amount of absorbed volatiles caused the Q values to drop into the range below Q of 100. Water turned out to be the most effective volatile. Injections of only half percent of carbon-dioxide into a fully saturated sand or sandstone caused the p-wave Q value drop sharply while s-wave Q values remained quasi-constant (Muckelmann, 1982).

One objective of reflection seismology is the two dimensional imaging of subsurface geological structures and their corresponding absorptive properties. Absorption requires body wave dispersion. The direct detection of body wave dispersion by conventional vibroseis techniques may be useful to distinguish between those crustal volumes of crystalline rock that are potentially seismogenic and those that are not. Such differences may be due to variations in fracture density and therefore water content in the crust. This study is concerned with the determination of velocity and Q in crystalline rocks of the southeastern U.S. Piedmont.

REVIEW OF PUBLISHED ABSORPTION-DISPERSION PAIRS

Aki and Richards (1980, p. 172-177) summarized difficulties with analytic expressions that involve the total phase (linear-with-frequency phase plus dispersive phase) and frequency limits of integration that extend to infinity. From Aki and Richard's equation (5.73)

$$\frac{\omega}{c(\omega)} = \frac{\omega}{c_\infty} + H[\alpha(\omega)] \qquad \text{(Aki and Richards Eq. 5.73)}$$

where the first term on the right-hand side is the phase due to the traveltime, the second term is the phase due to the body wave dispersion, and H denotes Hilbert transformation. If one is concerned with the "real, physical" phase velocity at some specific frequency, then using the continuous Hilbert integral from zero to infinity then he can expect an unbounded phase function that implicitly includes three terms:

1. A linear phase corresponding to the traveltime,
2. A dispersive phase which comes from the Hilbert integral,
3. Another linear phase "hidden" in the unbounded phase function obtained from the Hilbert integral of (2). We elaborate on this below. The hidden early and late phases are graphically summarized on Figure 2a.

Assuming known velocities, $c(\omega)$, at different frequencies one could compute Q from, for example, Aki and Richard's equation (5.77):

$$\frac{c(\omega_1)}{c(\omega_2)} = 1 + \frac{1}{\pi Q} \ln\left(\frac{\omega_1}{\omega_2}\right) \qquad \text{(Aki and Richards Eq. 5.77)}$$

However, if one wants to generate a synthetic seismogram using equation (5.77), then from the third item in the list above, he will detect an additional amount of nondispersive traveltime.

Aki and Richards (1980, p. 175) state that "It appears at this stage that the problem of finding values of $c(\omega)$ is essentially solved. We have merely to take the Hilbert transform of a constant-Q attenuation factor and then use (5.73)." They note that from

$$A(x) = A_0 e^{-\left(\frac{\omega x}{2cQ}\right)} \qquad \text{(Aki and Richards, Eq. 4, Box 5.7)}$$

we require

$$\frac{\omega}{c_\infty} + H[\alpha(\omega)] = 2Q\,\alpha(\omega) \qquad \text{(Aki and Richards, Eq. 5.74)}$$

and there is no Hilbert transform pair for which this relation is satisfied with constant Q. "(If it *were* satisfied, we could Hilbert transform (5.74). But this cannot be done since the transform for ω/c_∞ is a divergent integral.) Instead, we must tolerate a frequency-dependent Q, satisfying (5.74), but with an attenuation chosen to make Q effectively constant over the seismic frequency range."

We suggest that these problems can be overcome by invoking discrete Hilbert transformation and by recognizing that the total phase spectrum can be split up into a linear-with-frequency nondispersive phase defined by the traveltime of a reflected event, plus a pure dispersive phase spectrum that is associated with body wave dispersion brought about by causal absorption. Our numerical calculations are in excellent agreement with those of earlier workers, but our results are more general because no arbitrary constants are required to determine dispersion at any frequency between zero and Nyquist.

Cizek (1970) and Kak (1970) indicated that "continuous" Hilbert transformation and "discrete" Hilbert transformation are completely analogous and the theorems defined for the former can be easily extended to include the latter. Bolduc et al. (1972) suggested a scheme for the determi-

nation of the seismograph phase response from the amplitude response which is later used also by Luh (1977). For the Earth's dispersive-absorption problem we found Kolmogorov's technique more suitable because it avoids the early or late arrivals of the high frequency sinusoids and therefore provides a pure dispersive effect. The implementation of Kolmogorov's method is described in Claerbout (1985, p.62) and also in Taner et al. (1979).

We begin with a review of published absorption-dispersion pairs.

Seismic body wave dispersion was extensively investigated following the classical work of Futterman (1962). Futterman's relations are:

The absorption coefficient is

$$\alpha(\nu) = b\nu\,; \qquad \text{for } \nu > \nu_0$$

$$\alpha(\nu) = 0; \qquad \text{for } \nu \leq \nu_0$$

where b is a constant, and ν_0 is the low-cut frequency which is chosen below the frequency range of interest. The phase velocity:

$$c(\nu) = \frac{c_0}{1 - \frac{1}{2\pi Q} \ln \left| \frac{\nu^2}{\nu_0^2} - 1 \right|}$$

where c_0 is the velocity that corresponds to ν_0, and Q is the quality factor.

The phase-lag spectrum is

$$\theta(\nu) = 2\pi\nu\tau - \frac{\tau}{Q}\nu \ln \left| \frac{\nu^2}{\nu_0^2} - 1 \right|$$

where τ is the arrival time of the ν_0 frequency with c_0 speed. The phase-lag spectrum is shown in Figure 2a. The straight line $2\pi\nu\tau$ depicts the pure time delay of the frequency ν_0. If the other frequencies had the same amount of time-delay, there would be no dispersion; however, the second term in the phase-lag relation introduces the dispersion together with some amount of pure time advance. Futterman's approach is known in the literature as "the truncated-frequency attenuation".

Strick (1967, 1970, 1971) introduced the power-law attenuation. The absorption coefficient

$$\alpha(\nu) = K \cos(\frac{s\pi}{2}) |2\pi\nu|^s \quad 0 < s < 1$$

where s is the power, and K is a constant that depends on s.

The phase velocity is

$$c(\nu) = \frac{c_\infty}{1 + c_\infty K \sin(s\frac{\pi}{2}) |2\pi\nu|^{s-1}}$$

where c_∞ is the phase velocity at infinite frequency.

The phase-lag spectrum is

$$\theta(\nu) = 2\pi\nu\tau + K \sin(\frac{s\pi}{2}) |2\pi\nu|^s$$

where τ is the arrival time of the infinite frequency with c_∞ speed. The phase-lag spectrum is illustrated in Figure 2a. The straight line $2\pi\nu\tau$ depicts the pure time-delay of the infinite frequency. The second term in the phase-lag relation introduces the dispersion, but again with some amount of extra pure time-delay. We cannot consider this second term as a pure dispersive phase. When a phase spectrum is unbounded, there is always an implicit pure time-delay associated with it. (For Brune's pulse that has a bounded phase spectrum, there is no such pure time-delay contribution. See Appendix 1). Strick (1970) analytically derived (i.e., without using inverse Fourier transform) a relation that generates the shape of the time domain pulse. He then observed an amount of time elapse between the theoretical arrival time and the actual rise time of the pulse onset. He called this extra time-delay the "pedestal effect", and argued that this was a real physical effect in nature. Apparently, he was delaying the pulse more than he actually intended, i.e., $\tau + \tau_p$ instead of just τ. For a chosen high-cut frequency, ν_h, the duration of the "pedestal", τ_p, may be computed from

$$\tau_p = k \tan(s\frac{\pi}{2}) |2\pi\nu_h|^{s-1}$$

and in agreement with his discussion, τ_p becomes infinite when the power approaches 1. Therefore, to remove the "pedestal effect", based on our choice of ν_h, we subtract a pure time-delay of $2\pi\nu\tau_p$ from $\theta(\nu)$.

Strick (1970) also felt that Futterman's low-cut frequency ν_0 was conceptually and practically unnecessary; hence, he did not include a low-frequency cutoff in his expressions (not including ν_0 merely amounts to assuming $\nu_0 = 1$ Hz). Later, White and Walsh (1972) indicated that the mathematical behavior of these expressions outside the band, particularly at low frequencies, is physically unacceptable, and they introduced a "lumped-element" model of absorption-dispersion. It is well known that the logarithmic functions like $\ln \nu$ and exponential functions like $\nu^{0.1}$ change rapidly within $0 < \nu < 1$, and may not fit real data over this interval. Therefore, ν_0 may "monitor" the behavior of the functions and prevent these peculiar parts of the functions from being included in the frequency range of interest.

Kjartansson (1979) reports the following expressions. The absorption coefficient is

$$\alpha(\nu) = \frac{2\pi\nu_0}{c_0 \tan(s\frac{\pi}{2})} \left|\frac{\nu}{\nu_0}\right|^s$$

where ν_0 is an arbitrary frequency that may be chosen inside the frequency range of interest, c_0 is the phase velocity at ν_0., s is the power (for example, $s = 0.9$).

The phase velocity is

$$c(\nu) = c_0 \left|\frac{\nu}{\nu_0}\right|^{1-s}$$

where c_0 is the phase velocity at frequency ν_0.

The phase-lag spectrum is

$$\theta(\nu) = 2\pi\nu_0\tau \left|\frac{\nu}{\nu_0}\right|^s$$

where τ is the arrival time of the v_0 frequency with c_0 speed. Although this kind of phase expression may provide the necessary dispersion so that the causality is achieved, the exact traveltime of the pulse is uncertain. This kind of formulation for $\alpha(v)$ and $c(v)$ allows a constant Q behavior:

$$Q = \frac{\pi v}{\alpha(v)c(v)} = \frac{1}{2}\tan(s\frac{\pi}{2}) \quad = \text{constant}$$

Inspection of the phase lag expressions we have seen so far reveals that there are three different approaches (Figure 2a) to the dispersion problem:

1. Subtract an aperiodic dispersive phase term from the linear-with-frequency pure time delay (Futterman, 1962)
2. Add an aperiodic dispersive phase term to the linear-with-frequency pure time delay (Strick, 1967).
3. Bend the linear-with-frequency pure time delay to introduce dispersion (Kjartansson, 1979).

The important point to note is that the aperiodic dispersive phase terms are unbounded; therefore, they always implicitly subtract (as in Futterman) or add (as in Strick) or both add and subtract (as in Kjartansson) some amount of pure time delay.

Liu et al. (1976) showed that it is possible to construct a band-limited constant Q model by using a linear viscoelastic model. Based on the Liu et al. constant Q model, Kanamori and Anderson (1977) indicated the importance of physical dispersion in surface wave and free oscillation problems.

Azimi et al. (1968) published four absorption coefficient expressions and their corresponding phase velocities. Here, we reproduce the absorption coefficients only:

$$\alpha_1(v) = b_0 v^s$$

$$\alpha_2(v) = \frac{b_0 v}{1 + b_1 v}$$

$$\alpha_3(\nu) = \frac{b_0 \nu}{1 + b_2\sqrt{\nu}}$$

$$\alpha_4(\nu) = \frac{b_0 \nu^2}{1 + b_1 \nu^2}$$

where b_0, b_1, and b_2 are constants and s is the power. They called $\alpha_1(\nu)$, $\alpha_2(\nu)$, $\alpha_3(\nu)$ "almost linear" absorption laws, and $\alpha_4(\nu)$ an "almost quadratic" absorption law. $\alpha_1(\nu)$ and $\alpha_3(\nu)$ are unbounded, but $\alpha_2(\nu)$ and $\alpha_4(\nu)$ are bounded functions (with horizontal asymptotes of b_0/b_1); however, all of their absorption coefficient curves are upward convex, because they have to satisfy the Paley-Wiener condition for a continuous time process. On the other hand the absorption law suggested by Ricker (1977) has a square dependence on frequency and it is downward convex, but the aperiodic theory cannot provide an answer to it as it violates the Paley-Wiener condition of the continuous time process.

The Paley-Wiener condition for a continuous time process restricts the permissible choices of $\alpha(\nu)$ versus ν to those that increase slower than the first power of the frequency as the frequency becomes infinite; therefore, none of the absorption coefficient relations that we have discussed so far can have the power $s > 1$. In fact, for the case of a power-law attenuation, s must be strictly less than 1. This restriction mathematically forces the quality factor Q to become "slightly" frequency dependent (except in the case of Kjartansson).

If one takes out the pure time-delay parts (by simply subtracting a straight line of slope $\theta(\nu_h)/\nu_h$ from these phase-lag spectra), he will notice the curves so obtained are all tilted toward the left (Figure 2b). The particular shape of these pure dispersive phase-lag curves indicates that whatever the forms of the absorption coefficient expressions, they are all convex upward. This is dictated by the Paley-Wiener condition for a continuous time process.

In the present study, we overcome this difficulty by invoking periodic theory in which Kolmogorov's condition (the Paley-Wiener condition for the discrete time process) is always satisfied for any finite value of the power s.

Summary Table

Absorption - dispersion pairs		
Absorption coefficient	Phase velocity	Total phase
Futterman, 1962		
$\alpha(\nu) = b\lvert\nu\rvert$	$c(\nu) = \dfrac{c_0}{1 - \dfrac{1}{2\pi Q}\ln\left\lvert\dfrac{\nu^2}{\nu_0^2} - 1\right\rvert}$	$\theta_F(\nu) = 2\pi\nu\tau - \dfrac{\tau}{Q}\nu\ln\left\lvert\dfrac{\nu^2}{\nu_0^2} - 1\right\rvert$
Strick, 1970		
$\alpha(\nu) = K\cos(\dfrac{s\pi}{2})\lvert 2\pi\nu\rvert^s$	$c(\nu) = \dfrac{c_\infty}{1 + c_\infty K\sin(\dfrac{s\pi}{2})\lvert 2\pi\nu\rvert^{s-1}}$	$\theta_s(\nu) = 2\pi\nu\tau + K\sin(\dfrac{s\pi}{2})\lvert 2\pi\nu\rvert^s$
Kjartansson, 1979		
$\alpha(\nu) = \dfrac{2\pi\nu_0}{c_0\tan(\dfrac{s\pi}{2})}\left\lvert\dfrac{\nu}{\nu_0}\right\rvert^s$	$c(\nu) = c_0\left\lvert\dfrac{\nu}{\nu_0}\right\rvert^{1-s}$	$\theta_K(\nu) = 2\pi\nu\tau\left\lvert\dfrac{\nu}{\nu_0}\right\rvert^{s-1}$
This study		
$\alpha(\nu) = \dfrac{\pi}{Q\,p(\nu_N)}\nu$	$p(\nu) = \dfrac{p(\nu_N)}{1 + \dfrac{1}{2Q}\dfrac{H(-\nu)}{\nu}}$	$\theta(\nu) = 2\pi\nu\tau + \dfrac{\pi\tau}{Q}H(-\nu)$

THE MEASUREMENT OF ABSORPTION

Time domain.

The present study has resulted in the discovery of an exact method for the theoretical formulation of the effects of intrinsic damping where the attenuation coefficient, $\alpha(\nu)$, is an arbitrary function of the frequency, ν. As a result of this study, for any finite value of travel distance, a, absorption-dispersion pairs can now be determined. Approximate analytical expressions (see "Review of published absorption-dispersion pairs") that require the selection of arbitrary constants and cutoff frequencies are no longer necessary.

The derivations that follow have for their basis two assumptions:

1. The absorption coefficient $\alpha(\nu)$ is linear with frequency, ν. One of the important results of the present work, however, is to demonstrate that this is an unnecessary restriction; it is now possible to examine directly body wave dispersion for any behavior of $\alpha(\nu)$ vs. ν. Limitations are imposed only by the signal-to-noise ratio of the data.
2. Absorption in rocks is minimum-phase. This implies that the phase spectrum of the Earth's absorption may be uniquely recovered from the amplitude spectrum of the attenuated seismic event. Although we state here this minimum-phase property as an assumption, we later describe results from real multifold reflection seismic data that support the assumption; i.e., results of this study may be the first direct evidence that the mechanism for intrinsic damping is indeed a minimum delay physical process.

The Hilbert transform as given in Lee (1960, equation 65) is used to formulate the relation between the amplitude and phase spectra of an absorptive filter:

$$B(v) = -4\int_0^\infty \sin 2\pi vt\, dt \int_0^\infty \ln[A(u)]\cos 2\pi ut\, du \tag{6}$$

where A(v) and B(v) are the amplitude and phase spectra, respectively, of the absorptive filter. Here u is a dummy equivalent of v in integral expressions.

According to the first assumption:

$$A(u) = e^{-\alpha(u)a} = e^{-bu}$$

and

$$\ln[A(u)] = \ln[e^{-bu}] = -bu \tag{7}$$

Substituting (7) in (6) we obtain:

$$B(v) = 4\int_0^\infty \sin 2\pi vt\, dt \int_0^\infty bu \cos 2\pi ut\, du \tag{8}$$

Integration of the rightmost integral yields:

$$\int_0^\infty bu\cos 2\pi ut\, du = \frac{b}{2\pi t}\left| u\sin 2\pi ut + \frac{1}{2\pi t}\cos 2\pi ut\right|_{u=0}^{u=\infty} \tag{9}$$

When we apply the limit of integration of $u = \infty$ to (9), the rightmost integral becomes infinite. This is the difficulty encountered by earlier workers who used "aperiodic theory" (i.e., $u = \infty$) when $\alpha(u)a = bu^\gamma$ with $\gamma = 1$, as reviewed in the section "Review of published absorption-dispersion pairs". To overcome this difficulty others have chosen γ close to 1 (say $\gamma = 0.9$) thereby providing the necessary convergence of (9). This approach has been called (Strick, 1967) "power-law attenuation", $\alpha(u)$ is chosen such that Q is essentially constant over the frequency range of interest.

Instead of relaxing Q and allowing it to become "slightly" frequency dependent, in the present study we retain the assumption of strict linear-with-frequency behavior of $\alpha(u)$, but this time proceed directly and select some arbitrary Nyquist cutoff frequency. This step and examination of the consequences thereof is the step that was not considered by earlier workers including Strick (1967), Futterman (1962), Azimi et al. (1968), and Kjartansson (1979). Our new results are in excellent agreement with these earlier approximations, but are more general.

Equation (8) then becomes:

$$B(v) = 4\int_0^{T/2} \sin 2\pi v t \, dt \int_0^{v_N} bu \cos 2\pi u t \, du \tag{10}$$

where v_N is the Nyquist frequency, and T is the period.

The leftmost integral becomes:

$$\int_0^{v_N} bu \cos 2\pi u t \, du = \frac{b}{2\pi t} \left| u \sin 2\pi u t + \frac{1}{2\pi t} \cos 2\pi u t \right|_{u=0}^{u=v_N} \tag{11}$$

which has a finite value. Applying the limits of integration $u = 0$ and $u = v_N$ to (11) and substituting in (10) one obtains:

$$B(v) = \frac{2bv_N}{\pi} I_1 + \frac{b}{\pi^2} I_2 - \frac{b}{\pi^2} I_3$$

where

$$I_1 = \int_0^{T/2} \frac{1}{t} \sin 2\pi v_N t \sin 2\pi v t \, dt$$

$$I_2 = \int_0^{T/2} \frac{1}{t^2} \cos 2\pi v_N t \sin 2\pi v t \, dt$$

$$I_3 = \int_0^{T/2} \frac{1}{t^2} \sin 2\pi v t \, dt$$

Further investigation of these integrals yields (for simplicity we omit the limits of integration):

$$I_1 = \frac{1}{2}(J_1 - J_2)$$

$$I_2 = -\frac{1}{t}\sin 2\pi\nu t \cos 2\pi\nu_N t + \pi[(\nu - \nu_N)J_1 + (\nu + \nu_N)J_2]$$

$$I_3 = -\frac{1}{t}\sin 2\pi\nu t + 2\pi\nu J_3$$

where

$$J_1 = \int \frac{1}{t}\cos 2\pi(\nu - \nu_N)t \, dt$$

$$J_2 = \int \frac{1}{t}\cos 2\pi(\nu + \nu_N)t \, dt$$

$$J_3 = \int \frac{1}{t}\cos 2\pi\nu t \, dt$$

Solutions to integrals J_1, J_2, and J_3 may be found in Dwight (1961):

$$J_1 = \ln|2\pi(\nu - \nu_N)t| - \frac{[2\pi(\nu - \nu_N)t]^2}{2 \cdot 2!} + \frac{[2\pi(\nu - \nu_N)t]^4}{4 \cdot 4!} - \frac{[2\pi(\nu - \nu_N)t]^6}{6 \cdot 6!} + \cdots$$

$$J_2 = \ln|2\pi(\nu + \nu_N)t| - \frac{[2\pi(\nu + \nu_N)t]^2}{2 \cdot 2!} + \frac{[2\pi(\nu + \nu_N)t]^4}{4 \cdot 4!} - \frac{[2\pi(\nu + \nu_N)t]^6}{6 \cdot 6!} + \cdots$$

$$J_3 = \ln|2\pi\nu t| - \frac{[2\pi\nu t]^2}{2 \cdot 2!} + \frac{[2\pi\nu t]^4}{4 \cdot 4!} - \frac{[2\pi\nu t]^6}{6 \cdot 6!} + \cdots$$

The phase spectrum in terms of J_1, J_2, and J_3 becomes:

$$B(\nu) = \frac{b}{\pi^2}\left|\frac{1}{t}(1 - \cos 2\pi\nu_N t)\sin 2\pi\nu t\right|_{t=0}^{t=T/2} + \frac{b}{\pi}\nu\left|J_1 + J_2 - 2J_3\right|_{t=0}^{t=T/2}$$

Now apply the limits of integration to the first term on the right hand side and represent the second term by J. We obtain

$$B(\nu) = \frac{4bv_N}{\pi^2} \sin\pi\frac{\nu}{v_N} + J \qquad (12)$$

The shape of $B(\nu)$ defined by this equation is the general shape found in the real data as discussed in the section "Applications to real data: the ADCOH reflection seismic data" and illustrated later in Figure 27.

The first term on the right-hand side of (12) represents a half-period sine wave for $0 \leq \nu \leq \nu_N$. The half-period sine wave dominates the shape of the phase spectrum curve (Figure 3). The second term J which contains the series part is the perturbation to the half-period sine wave. The contribution of J to the phase spectrum is small but not negligible. The convergence of the series in J is slow. In any case, instead of computing a phase spectrum analytically, we can use numerical Hilbert transformation. The dominant half-period sine wave, the phase spectrum curve from numerical Hilbert transformation, and the shape of the perturbation term J for the entire series are shown in Figure 3.

We do not use equation (12) above to compute phase spectra, $B(\nu)$, because $B(\nu)$ can be determined directly by numerical Hilbert transformation.

Let $\theta(\nu)$ be the total (dispersive phase spectrum plus the linear-with-frequency phase corresponding to nondispersive traveltime) phase spectrum:

$$\theta(\nu) = B(\nu) + 2\pi\nu\tau \qquad (13)$$

where $B(\nu)$ is defined here as the pure body wave "dispersive phase" and $2\pi\nu\tau$ is the phase angle that corresponds to some pure traveltime, τ. Thus,

$$\theta(\nu) = 2\pi\nu t = 2\pi\nu\frac{a}{p(\nu)} \qquad (14)$$

where t is now total time (the sum of the traveltime plus a frequency-dependent time delay due to body wave dispersion), a is the travel distance, and $p(\nu)$ is the dispersive phase velocity.

From (13) and (14) one may derive p(v). Once p(v) is known, the group velocity is obtained from:

$$g(v) = \frac{p(v)}{1 - \frac{v}{p(v)}\frac{dp(v)}{dv}} \tag{15}$$

A New Approximate Analytical Approach

In order to gain insight into the details of body wave dispersion, an approximate analytical expression, $\bar{B}(v)$, for B(v) may be examined by neglecting the series term J in (12). We do, in fact, require the approximation in order to determine B(v) at v = 0. We write:

$$\bar{B}(v) = \frac{4bv_N}{\pi^2}\sin(\pi\frac{v}{v_N}) \tag{16}$$

Let also,

$$\tau = \frac{a}{p(v_N)} \quad \text{and} \quad b = \frac{\pi a}{Q\, p(v_N)} \tag{17}$$

where τ is the traveltime, $p(v)_N$ is the phase velocity at Nyquist frequency, a is the travel distance.

From (13), (14), (16), and (17) the phase velocity is:

$$\bar{p}(v) = \frac{p(v_N)}{1 + \frac{2v_N}{\pi^2 Q}\frac{1}{v}\sin(\pi\frac{v}{v_N})} \tag{18}$$

From (15) and (18) the group velocity is:

$$\bar{g}(\nu) = \frac{p(\nu_N)}{1 + \frac{2}{\pi Q}\cos(\pi\frac{\nu}{\nu_N})} \tag{19}$$

The approximate phase and the approximate group velocity curves are shown in Figure 4.

A New Exact Numerical Procedure

The preceding discussion included a review of the literature relevant to dispersion-absorption pairs, a new derivation of the analytical result of Hilbert transformation of linear-with-frequency attenuation (section "Time domain."), and an analytical expression that approximates the body wave dispersion that accompanies intrinsic damping (section "A New Approximate Analytical Approach"). We seek an exact procedure to compute attenuation-dispersion pairs for an arbitrary behavior of $\alpha(\nu)$ versus ν.

To derive an exact expression for body wave dispersion, we follow the same procedure as in the approximate analytical approach. It should be noted that, although a linear-with-frequency attenuation is used here as an example, the numerical approach discovered in this study is appropriate for *any* behavior of $\alpha(\nu)$ versus ν. This means that the inverse problem, that of determining $\alpha(\nu)$ versus ν from Hilbert transformation of the phase spectrum as derived from real data, will reveal the nonlinear dependence of $\alpha(\nu)$ versus ν *if it is present in the data.* This should have important implications for detecting frequency ranges over which values of Q are different but constant over limited segments. For example, an increased amount of water in a fractured crust might change the slope of $\alpha(\nu)$ versus ν as ν increases. This "exact numerical procedure" is possible because of the direct application of discrete Hilbert transformation.

The phase spectrum, $B(\nu)$, for linear-with-frequency absorption as obtained by the exact numerical procedure is:

$$B(\nu) = H[\ln A(\nu)] = H[\ln e^{-b\nu}] = bH(-\nu) \tag{20}$$

Here, H stands for numerical Hilbert transformation. Again, from (13), (14), (17), and (20) the phase velocity is:

$$p(\nu) = \frac{p(\nu_N)}{1 + \frac{1}{2Q}\frac{H(-\nu)}{\nu}} \tag{21}$$

and from (15) and (21) the group velocity is:

$$g(\nu) = \frac{p(\nu_N)}{1 + \frac{1}{2Q}\frac{dH(-\nu)}{d\nu}} \tag{22}$$

Although $H(-\nu)/\nu$ and $dH(-\nu)/d\nu$ give the exact shapes of the phase velocity and group velocity curves, respectively, for all values of ν, they do not provide information about the limiting values for $\nu = 0$ and $\nu = \nu_N$. Equation (12) can be used to compute the limits of the corresponding phase and group velocities obtained from numerical Hilbert transformation, or the limiting values may be obtained as follows:

Comparison of (21) with (18) yields:

$$\frac{H(-\nu)}{\nu} \cong \frac{4\nu_N}{\pi^2}\frac{1}{\nu}\sin(\pi\frac{\nu}{\nu_N}) \tag{23}$$

Comparison of (22) with (19) yields:

$$\frac{dH(-\nu)}{d\nu} \cong \frac{4}{\pi}\cos(\pi\frac{\nu}{\nu_N}) \tag{24}$$

Then, following the relations (23) and (24) we obtain:

$$\lim_{\nu \to 0}\frac{H(-\nu)}{\nu} = \frac{4}{\pi} \text{ and } \lim_{\nu \to \nu_N}\frac{H(-\nu)}{\nu} = 0 \tag{25}$$

$$\lim_{\nu \to 0}\frac{dH(-\nu)}{d\nu} = \frac{4}{\pi}; \lim_{\nu \to \nu_{N/2}}\frac{dH(-\nu)}{d\nu} = 0 \text{ and } \lim_{\nu \to \nu_N}\frac{dH(-\nu)}{d\nu} = -\frac{4}{\pi}$$

Now every dispersive velocity value can be computed from (21) and (22) from $v = 0$ to $v = v_N$, inclusive. There are no arbitrary constant(s) to choose.

The exact phase and the exact group velocity curves are shown in Figure 4. The effects of different absorption levels on absorption coefficient, dispersive phase, and impulse response are shown in Figure 5.

Derivation of Dispersion, D, and Q

The percent, D, of body wave dispersion over the entire bandwidth from $v = 0$ to $v = v_N$ for a linear-with-frequency attenuation may be defined as

$$D = \frac{p(v_N) - p(0)}{p(v_N)} \tag{26}$$

As described in the section "A New Exact Numerical Procedure", it is possible to determine a value for D over any frequency interval. For example, for a vibroseis sweep of between 14 and 56 Hz and a medium of Q = 250; then

$$\frac{p(56) - p(14)}{p(56)} = 1.846 \text{ X } 10^{-3} = 0.1846 \text{ percent}$$

which can be interpreted to mean that a seismic pulse broadens by about 2.2 milliseconds per second of traveltime. The higher frequencies travel faster.

From equation (21) and equation (25), the phase velocity at $v = 0$ is:

$$p(0) = \frac{p(v_N)}{1 + \frac{2}{\pi Q}}$$

and body wave dispersion, D, over the entire band width from $v = 0$ and $v = v_N$ for a linear-with-frequency absorption coefficient is

$$D = \frac{p(v_N) - p(0)}{p(v_N)} = 1 - \frac{1}{1 + \frac{2}{\pi Q}} = \frac{1}{1 + \frac{\pi}{2} Q} \qquad (27)$$

Equation (27) says that the value of D is independent of any frequency cutoff. Wuenschel (1965) reports 2.6 percent of phase velocity variation between 25 and 400 Hz for the Pierre Shale to which he assigns an approximate value of $Q \cong 30$. According to our equation (27) such a value of Q corresponds to D = 2.1 percent. Waters (1987, p. 33) gave an average value from 17 samples of Pierre Shale to which he assigned a value of Q = 17 for phase velocity determinations over the frequency range 75-555 Hz. According to (27) a value of Q = 17 corresponds to D = 3.6 percent. Equation (27) determines the values of dispersion over the entire frequency band. Considering the apparent range of values of Q for the Pierre Shale, our computed values of total dispersion are in excellent agreement with published values over restricted frequency ranges.

We now compute the difference in dispersive time delay, ΔW, between frequencies $\nu = 0$ and $\nu = \nu_N$. Since both of these frequencies traveled the same distance a, then:

$$a = p(\nu_N)\,\tau = p(0)(\tau + \Delta W)$$

where τ is the pure travel-time. Then

$$\Delta W = \frac{p(\nu_N) - p(0)}{p(0)}\,\tau$$

From the expression for body wave dispersion we have

$$\frac{p(\nu_N) - p(0)}{p(0)} = D\,\frac{p(\nu_N)}{p(0)} = \frac{1 + \frac{2}{\pi Q}}{1 + \frac{\pi Q}{2}} = \frac{2}{\pi Q}$$

Therefore,

$$\Delta W = \frac{2\tau}{\pi Q}$$

or,

$$Q = \frac{2\tau}{\pi \Delta W} \tag{28}$$

Equation (28) makes possible time-domain measurements of Q. τ is the total (two-way) traveltime and ΔW is the amount of wavelet breadth increase during the time τ. Gladwin and Stacey (1974), and Kjartansson (1979) gave a similar, but empirical, relation; i.e., the broadening is proportional to the traveltime and is related to Q by the equation

$$W_2 = \frac{C}{Q}(\tau_2 - \tau_1) + W_1 \tag{29}$$

where W_2 is the pulse width at the time τ_2, W_1 is the pulse width at the time τ_1, and C is an arbitrary constant to be determined empirically from some other means of Q measurements (spectral techniques, for example). There is no consensus in the literature, however, on the exact value of C (Blair and Spathis, 1984). Kjartansson (1979) used C = 0.485, Gladwin and Stacey (1974), Badri and Mooney (1987) used C = 0.5 in their time domain computations of Q.

Here, we give the exact value of C on the basis of the above derivations; i.e.,

$$C = \frac{2}{\pi}$$

Discussion

We have seen that analytic attempts to force convergence of the integral (9) restrict the value of γ for power-law attenuation to

$$0 < \gamma < 1$$

This is unfortunate because the approximation imposed by aperiodic theory cannot provide a solution for cases where $\gamma \geq 1$. For example, $\gamma = 1$ which is widely observed in most rocks, and $\gamma = 2$ reported by Ricker (1977) for viscoelastic absorption, are not solvable. When direct numerical Hilbert transformation is used, however, the difficulty with integral (9) is removed.

The possibility of obtaining a phase spectrum by Hilbert transformation of the amplitude spectrum to generate a realizable minimum-delay wavelet may be predicted from the Kolmogorov (1941) condition:[1]

$$\int_{-\Omega}^{+\Omega} |\ln A(\omega)|\, d\omega < \infty \tag{30}$$

For a power-law attenuation:

$$A(\omega) = e^{-b|\omega|^{\gamma}} \tag{31}$$

where $\gamma > 0$ and $b > 0$ are constants.

Since (31) is an even function, (30) becomes:

$$2\int_{0}^{\Omega} |\ln e^{-b\omega^{\gamma}}|\, d\omega = \frac{2b}{\gamma + 1}\Omega^{\gamma+1} < \infty$$

for any finite Ω, γ, and b Kolmogorov's condition is therefore satisfied.

Different examples of power-law attenuation are shown in Figure 7. As predicted by the Kolmogorov condition, the roots of the z-transform polynomial of each impulse-response are outside the unit circle and the impulse responses are therefore minimum-delay.

The group velocity g(v) as shown in Figure 4 is larger than the phase velocity, except at zero frequency where they are equal. This is known as an anomalous group velocity and

[1] Also known as the Paley-Wiener criterion for a discrete-time process.

is associated with frequency-dependent absorption. Following Brillouin (1960, p. 129) and White (1983, p. 90), we merely state that the concept of group velocity is not applicable here, and do not consider it further. However, the energy transport velocity is a useful parameter. In an absorptive medium it is less than the phase and the signal velocity.

Effect of the Nyquist Frequency on the Dispersive Phase Spectrum

We have examined the shape of the minimum-phase curve obtained from discrete Hilbert transformation of the strictly linear with frequency absorption coefficient, $\alpha(\nu)$. In general, minimum-phase curves obtained from discrete Hilbert transformation start with zero value at zero frequency, stay as close as possible to the frequency axis, may cross the frequency axis several times, or may not cross it at all; they are continuous (if unwrapped) but not continuously zero. Eventually they converge back to zero at the Nyquist frequency.

Discrete Hilbert transformation computes a finite number of minimum-phase spectrum components from a given finite number of amplitude spectrum components so that the corresponding finite time domain pulse possesses the minimum-delay property. On the other hand, continuous Hilbert transformation with limits of integration that extend to infinity considers the entire frequency content; hence, the corresponding time domain pulse which is defined for entire positive time is also minimum-delay. The difference between discrete and continuous Hilbert transformation is then the finiteness versus the infiniteness of the process. This point was illustrated by this study, Appendix 1, using Brune's pulse (Brune, 1968).

When we desire a minimum-phase property in a discrete process, for a given Nyquist frequency there is only one phase spectrum that can provide this property. The same uniqueness holds also for the continuous process. For a discrete process, however, each cutoff frequency has a different phase spectrum that is computed from a related amplitude spectrum corresponding to the same Nyquist frequency. We now investigate the relationship between these different phase spectra for the case of the dispersive phase spectrum, $B(\nu)$.

In Figure 8 four dispersive phase curves are shown. Their corresponding values of $\alpha(v)$ are not shown because they make up a simple straight line that continues across the consecutive Nyquist frequencies. The dispersive phase curves correspond to folding frequencies of 62.5, 125, 250, and 500 Hz, respectively.

One can generate the corresponding impulse-responses, f(t), from:

$$f(t) = \int_{-v_N}^{+v_N} A(v)\, e^{+i2\pi vt} dv = \int_{-v_N}^{+v_N} e^{-bv}\, e^{iB(v)}\, e^{+i2\pi vt} dv$$

$$= \int_{-v_N}^{+v_N} e^{-bv}\, e^{ibH(-v)}\, e^{+i2\pi vt} dv$$

For our display purposes, before examining the shape of f(t), a choice must be made for the constant, b. In recording band-limited data, an anti-alias filter is always used so that no frequencies are sampled above the Nyquist frequency. If this were not the case aliasing would occur. A value of b is thus chosen such that

$$e^{-bv} \cong 0 \quad \text{for} \quad v \geq \frac{1}{2\Delta t}$$

The Earth and our instruments conspire to satisfy this condition automatically. If $\exp(-bv) \cong 0$ for a given Nyquist, then it certainly will for any Nyquist higher than this. Once the choice of b is made, f(t) can be examined.

The impulse response, f(t), can be interpreted as the Earth's impulse response for absorption. These impulse-responses for several Nyquists are shown in Figure 8. As expected, a visual examination discloses that they have the same shape; they are, however, separated from each other by a pure time-delay. In fact, if the appropriate time delays, as shown in Figure 8 with straight lines extending from zero to some value on the reference dispersive phase curve for 500 Hz, are applied to each dispersive phase curve, one obtains the time-delayed dispersive phase shown in Figure 9. As shown in Figure 9, the impulse-responses corresponding to different folding-frequencies are identical in shape. Thus, although dispersive phase spectra related to each Nyquist frequency are different, their corresponding impulse-

responses are identical in shape but are separated from each other by a constant pure time-delay.

The reason for this pure time delay (about 16 ms in this particular example) is obvious from Figure 10. Since the amplitude spectrum of the impulse response effectively covers the phase spectrum related to the Nyquist of 62.5 Hz, high-frequency sinusoids with a substantial amount of amplitude rush up and build the onset of the impulse at the theoretical traveltime; however, when the selected Nyquist frequency is greater than the effective range of the amplitude spectrum of the impulse response, then the high frequency sinusoids still rush to build up the impulse onset at the theoretical traveltime, but they do not have enough amplitude to contribute to the visible onset of the impulse. Therefore, their location in time; i.e. the first tens of milliseconds (depending on the amount of absorption) immediately after the (maximum) theoretical traveltime remains vacant. On the other hand the dispersion of the effective amplitude spectrum band of the impulse response is performed by the corresponding segment of the phase spectrum generating the expected minimum delay pulse. For synthetically created data, this delay can be eliminated by simply choosing a Nyquist frequency close to the upper limit of the frequency content of the synthetic data. The SVD determinations of Q described below have for their basis the assumption of a pure dispersive minimum phase spectrum; therefore, the analyses are unaffected by the simple time shift displayed in Figure 8.

Generalization to any frequency dependent Q

We have demonstrated that for a given linear-with-frequency absorption coefficient $\alpha(v)$, even though we obtain different dispersive phase spectra for different cutoff frequencies, we can still generate time-domain impulse responses that are identical in shape that correspond to those folding frequencies. We need only be concerned with aliasing in the frequency domain; i.e., the Nyquist frequency must chosen such that the shape of the Earth's impulse response is time invariant for any higher Nyquist.

Having shown that the effect of different folding frequencies is a simple time-shift of Earth impulse-responses for the case of $\alpha(v) = bv^{\gamma}$ with $\gamma = 1$, we now generalize this for all $\gamma > 0$. Dispersive phase spectra for $\gamma = 0.5$ corresponding to folding frequencies 62.5, 125, 250, and 500 Hz are shown on Figure 11. The appropriate time delays (i.e., linear phase shifts) are also shown. The impulse-responses related to those dispersive phase spectra are shown in Figure 11. They differ from each other by a constant amount of time. Time-delays applied (i.e., linear phase shifts added) and dispersive phase spectra are shown in Figure 12, and their corresponding impulse-responses, which are identical in shape are also shown in Figure 12.

In the same manner, dispersive phase spectra for $\gamma = 1.5$ corresponding to folding frequencies 62.5, 125, 250, and 500 Hz are shown in Figure 13. Again, the appropriate straight lines for a time-delay are also shown. The impulse-responses prior to the time-delays are shown in Figure 13. They differ from each other by a constant amount of time. After application of the time-delays, the dispersive phase spectra and their related impulse-responses are shown in Figure 14. Note again the perfect resemblance among them when they are superimposed.

Since the shapes of the impulse-responses are independent of the Nyquist frequency, any absorption and dispersion computations based on them are also independent of the folding frequency.

Comparison of exact absorption-dispersion curves with Futterman (1962)

Futterman's (1962) velocity dispersion expression is superimposed in a piecewise manner upon our exact curve as seen in Figure 15. We generated our dispersive velocity curve for ν_N = 125 Hz and Q = 250 from 0 to 125 Hz. We computed pieces of Futterman's phase velocity curve using the same Q. For a chosen frequency interval, we searched for a ν_0 at the lower frequency end of the interval. For each trial ν_0 we obtained the corresponding reference velocity, c_0 from our curve. We supplied ν_0 and c_0 so obtained to the Futterman's phase velocity relation. The best fit constants of Futterman are shown above each segment in Figure 15. The excellent agreement using appropriate constants c_0 and ν_0 for Futterman is apparent in the figure. Note that it is not possible to superimpose Futterman's entire results with a single selection of his constants. In our relation, there is no arbitrary constant other than Q that governs the shape of the velocity dispersion curves computed from discrete Hilbert transformation; $p(\nu_N)$ is merely a scale factor.

Frequency Domain

We start with the traveltime equation:

$$ay = t \tag{32}$$

where a is the travel distance, y is the slowness (to be determined), and t is the traveltime. Once y is computed, then from

$$p = \frac{1}{y} \; ; \; \delta p = p\frac{\delta y}{y} \tag{33}$$

we obtain the phase velocity p (i.e., $p(v_N)$, the velocity at the Nyquist frequency) and its uncertainty δp.

Input-output relation

The frequency domain representation of the input-output wavelets in the form we are presently using is:

$$G(v)e^{ig(v)} = F(v)e^{if(v)}Re^{ir}A(v)e^{iB(v)} \tag{34}$$

$F(v)$ and $G(v)$ are the amplitude spectra, $f(v)$ and $g(v)$ are the phase spectra of the input and output wavelets, respectively. R is a frequency-independent real scale factor representing geometrical spreading, transmission and reflection coefficients, and free surface effects; i.e., any constant that does not distort the wavelet shape. r is the frequency-independent phase-shift due to complex reflection coefficients which occur beyond critical incident angles, if any. For the ADCOH data set used in this study, critical angles are not anticipated because of the depth to the target and the recording geometry used. $A(v)$ and $B(v)$ are the amplitude and phase spectra for causal-absorption, respectively, and v is the frequency.

Equation (34) does not include source and receiver side directivity functions and array responses, source and receiver ground coupling, instrument response, or scattering due to stratigraphic filtering.

The causal-absorption terms in (34) are:

$$A(v) = e^{-\alpha(v)a} \; ; \; B(v) = H[\ln A(v)]$$

where the absorption coefficient $\alpha(v)$ is

$$\alpha(v) = \frac{\pi v}{Qp}$$

Now let,

$$\alpha(v)a = bv \quad \text{and} \quad x = \frac{\pi}{Qp} = \frac{\pi y}{Q}$$

Then,

$$ax = b \tag{35}$$

a is the travel-distance, x is the parameter to be determined, and b is the slope of bv. Once the slowness y is computed from equation (32), then the value of Q is obtained from

$$Q = \pi \frac{y}{x} \; ; \; \delta Q = Q\left[\left(\frac{\delta x}{x}\right)^2 + \left(\frac{\delta y}{y}\right)^2\right]^{1/2} \tag{36}$$

where δQ. is the uncertainty on Q.

The quantities t and b in (32) and (35), respectively, are obtained from the seismic data traces. t is observed in the time domain from the data, and b is computed in the frequency domain from a least-squares analysis.

Express equation (34) in terms of b

$$G(v)e^{ig(v)} = F(v)e^{if(v)}Re^{ir}e^{-bv}e^{ibH(-v)} \tag{37}$$

If we separate (37) into its amplitude and phase components we obtain:

$$\ln R - b_A v = \ln\left[\frac{G(v)}{F(v)}\right] \tag{38}$$

$$r + b_P H(-v) = g(v) - f(v) \tag{39}$$

These are the two spectral techniques for the determination of absorption. Equation (38) is the usual spectral ratio method; equation (39) is the new phase method. To use either method, the spectrum of the source pulse must be known or approximated.

Equations (38) and (39) are in suitable form for a least-squares analysis. Equation (38) is the conventional amplitude spectrum ratio technique where R and b_A are the estimated values along with their uncertainties δR and δb_A; $\ln [G(\nu)/F(\nu)]$ is computed from the data over a specified frequency interval, and $(- \nu)$ is the function to be fitted.

Equation (39) defines the new technique named "phase spectrum difference" by Ecevitoglu and Costain (1985) where r and b_P are the estimated values with their uncertainties δr and δb_P. The phase difference $[g(\nu) - f(\nu)]$ is computed from the data over the desired frequency interval, and $H(- \nu)$ is the function that is fitted to the data. Note that we do not attempt to fit the *total* phase spectrum to the observed data, only the pure dispersive part is considered. The *total* phase spectrum is dominated by the phase introduced by the time-shifting theorem. By using a dynamic analysis window over the wavelets, the pure time delay part of the phase spectrum is stripped away.

The related linear regression formulae and their derivations can be found in Taylor (1982, Chapter 8).

SINGULAR VALUE DECOMPOSITION (SVD)

Ecevitoglu (Appendix 2) summarized differences between various least squares procedures and the advantages and disadvantages of singular value decomposition over conventional least squares methods.

The most reliable method for computing the coefficients for a general least-squares problem is based on an orthogonal matrix factorization known as Singular Value Decomposition (SVD). This method is efficient in dealing with errors in the data, round-off errors, and linear dependence. It is important to identify rank deficient situations when solving least-squares problems. The only fully reliable way to treat rank deficiency is to compute the SVD. The procedure used is described in detail in Appendix 2. A brief overview is given here.

Sparsity Considerations

The kind of matrices encountered when using conventional multifold reflection seismic data are sparse. Sparsity patterns are sensitive to row and column interchanges. It would be desirable to improve the sparsity patterns by judicious choice of row and column interchanges to minimize the fill-in. When a matrix is arbitrarily sparse (as with reflection seismology data), the rows and columns can be reordered so that it is in approximate "dual-angular" structure in which the fill-in will be restricted to the diagonal and vertical blocks (Gill and Murray, 1976). In addition, this kind of preprocessing allows a simpler data structure to be used and

has, especially for problems requiring backing store, substantial implementation advantages (Bjorck, 1976).

Ecevitoglu (Appendix 2) gave an algorithm suitable for multichannel seismic processing for generating the matrix A (the design matrix) which possesses the approximate dual-angular structure.

Least-squares Problem

The system of linear equations arising from seismic applications has the form

$$AX = B \tag{40}$$

where A is the design matrix, X is the solution vector, and B is the data vector. The least-squares method is defined as

$$A^TAX = A^TB \tag{41}$$

Equation (41) is known as the system of "normal equations". The least-squares estimates of X which we denote by $\hat{X}$ would be

$$\hat{X} = A^TB \tag{42}$$

However, the singular value decomposition (SVD) of A is

$$A = USV^T \tag{43}$$

From equation (43), recalling $U^TU = V^TV = I$ and $S^T = 1/S$ we obtain

$$A^T = V\frac{1}{S}U^T \tag{44}$$

The least-squares solution is (Appendix 2)

$$\hat{X} = V\frac{1}{S}U^{T}B \tag{45}$$

For computer implementation, express matrix equations (40) and (45) *element wise* (each element of upper case lettered matrix represented by its lowercase equivalent)

$$\sum_{j=1}^{n} a_{ij}x_j = b_i \tag{46}$$

with $1 \leq i \leq m$ and $1 \leq j \leq n$. Here m and n ($m > n$, i.e. overdetermined case) stand for the number of observations and number of unknowns, respectively. The least-squares estimates of the solution vector

$$\hat{x}_j = \sum_{k=1}^{r} v_{jk}\frac{p_k}{s_k} \tag{47}$$

where

$$p_k = \sum_{i=1}^{m} u_{ik}b_i \tag{48}$$

with $1 \leq k \leq r$. Here r ($r \leq n$) stands for pseudorank

$$\sigma = \left[\frac{1}{m-n}\sum_{i=1}^{m}(b_i - \sum_{j=1}^{n} a_{ij}x_j)^2\right]^{0.5} \tag{49}$$

The number σ can be interpreted as an unbiased estimate of the standard deviation of errors in the data vector B.

Lawson and Hanson (1974, p. 198) reported that inspection of the columns of the matrix V associated with small singular values is an effective technique for identifying the sets of columns of A that are nearly linearly dependent. Following this idea we derive

$$\delta\hat{x}_j = \sigma\left[\frac{1}{r}\sum_{k=1}^{r}(\frac{v_{jk}}{s_k})^2\right]^{0.5} \tag{50}$$

We interpret $\delta\hat{x}_j$ as the estimated error of the j^{th} least-squares solution. Note that $\delta\hat{x}_j$ includes both the error coming from the data (i.e. σ) and the error introduced by the decomposition process of the design matrix.

In this particular application the matrix form of the equations (32) and (35) are

$$AY = T \tag{51}$$

$$AX = B \tag{52}$$

The data vectors are T and B, and the unknowns are the vectors Y and X. The "design" matrix, A, is the same for both unknown vectors, Y and X.

PROCEDURE

Time domain

Application of equation (28) or (29) with $C = \frac{2}{\pi}$ to a seismogram involves the following procedure:

1. Measure the input Klauder wavelet breadth (peak-to-peak or trough-to-trough time duration).
2. Measure the output wavelet travel time, τ, and breadth (same peak to peak or trough to trough time duration, although the wavelet is now distorted by causal absorption).
3. Subtract the output wavelet breadth from the input wavelet breadth. This is ΔW.
4. Substitute τ and ΔW so found in equation (28).

The steps described above have been applied to Figure 6 to compute an average Q between the surface and the reflectors, or between a shallow reference reflector and the deeper reflectors. Values of Q determined in the time domain may then be compared with values of Q found from the SVD average solutions for the ADCOH data.

Frequency domain

The first step in spectral analysis is to extract the reflected wavelet from the seismic trace using a time window. We have seen that when a wavelet travels through an attenuating medium its shape and breath continuously change; therefore, it is practically impossible to pursue a selected peak or trough in the wavelet along the entire ray-path.

Length of the analysis window

The analysis time window should be large enough to appropriately cover the frequency range of interest. For the unattenuated Klauder wavelet the analysis window, w, should be (Ecevitoglu, 1984).

$$w \geq \frac{1}{2\,\nu_L} \tag{53}$$

where ν_L is the lower frequency bound of the Vibroseis sweep.

In an attenuating medium, the breath of the wavelet continuously increases as the wavelet progresses along the ray-path. Therefore, if w is initially set according to (53) it must be increased as the offset (source to receiver distance) increases, or as the wavelet is returned from deeper reflectors.

One can decide on the analysis window length by examining the reflected wavelets themselves. It would be tedious to do this for every wavelet due to the large number of traces encountered in reflection seismology. In practice, a limited number of analysis window lengths may be selected and applied to the group of traces which are either attributed to the same reflector (if the data contains reflections from more than one reflector) or to a range of offset distance (if there is one reflector only).

The analysis window length should be large enough to cover as much information as possible without including any neighboring event (other reflections or converted phases) which

may contaminate the primary reflection. This is, of course, not possible in the general case, and the excellent agreement between a synthetically attenuated wavelet and the real data (Figure 16) indicates that the analysis criteria used are robust in the presence of overlapping wavelets.

Positioning of the analysis window

This is the crucial part of the windowing operation that requires some method of "dynamic positioning". Although the amplitude spectrum ratio technique is not too sensitive to the position of the analysis window over the reflected wavelet (i.e., a deviation of the analysis window over the event for a few sample intervals does not cause much of a discrepancy in the computation of Q), the technique of using the phase spectrum difference is extremely sensitive to the position of the analysis window (Figure 17); therefore, a simple visual travel-time pick of the reflected wavelet may introduce severe errors in Q computations.

Computations with synthetic data show that the correct window position over an absorbed wavelet for purely dispersive phase (no additional phase due to traveltime) is such that the window sits over the earlier part of the absorbed wavelet rather than over a more "visually" reasonable position that, for example, might be intuitively selected on the basis of symetrically disposed zero crossings or wavelet geometry. This is because causal absorption introduces a real delay of the peaks and troughs of the absorbed wavelet. The positioning is done in the frequency domain in an iterative manner.

If we know what kind of behavior of $\alpha(v)$ versus v to expect in the data (in this particular study we expect a linear-with-frequency absorption coefficient and its corresponding approximate half sine wave dispersive phase spectrum), then a number of criteria can be devised that will lead to the optimal positioning of the analysis window. The following steps were performed in the present study:

1. Observe the reflected wavelet on the seismic records and pick an approximate traveltime.

2. Select the analysis window length and the amount of deviation in time of the analysis window around the approximate travel-time of (1).
3. Within the given deviation range, the analysis window is shifted one sample interval at a time. For each assumed position, a least-squares analysis is performed on the time samples that fall inside the analysis window. The computed quantities are $b_A, \delta_A, \delta b_A$ from the amplitude spectrum ratio technique, and $b_P, r, \delta_P, \delta b_P, \delta r$ from the phase spectrum difference technique. b_A and b_P are estimated values of the absorption coefficient, δb_A and δb_P are their respective uncertainties, δ_A and δ_P are the sum of squares of the residual errors based on the data and estimated values, r and δr are the estimated phase shift value and its uncertainty.
4. Evaluate the following physical conditions:

$$b_A - \delta b_A > 0$$

$$b_P - \delta b_P > 0$$

5. If both of the physical conditions in (4) are satisfied then evaluate the following statistical conditions:

$$\delta = \delta_A + \delta_P$$

6. Among the δ's computed in (5), the position of the optimal analysis window is the one which has the smallest value of δ.

At this stage the optimal analysis window position is determined. We may now compute the following:

7. Replace the approximate travel-time of (1) with its exact value.
8. Compute the weighted average of the absorption coefficient for each trace from

$$b = \frac{b_P \cdot \delta_A + b_A \cdot \delta_P}{\delta_A + \delta_P} \tag{54}$$

and its average uncertainty from

$$\delta b = \frac{\delta b_P \cdot \delta_A + \delta b_A \cdot \delta_P}{\delta_A + \delta_P}$$

9. Evaluate the following physical conditions:

$$r + \delta r < 0$$

$$r - \delta r > -2\pi$$

If r satisfies both of the above physical conditions, and if the velocity at the reflecting interface is low above and high below together with enough offset distance so that critical incident angles may occur, then r may be viewed as a frequency independent phase shift due to a complex reflection coefficient; hence, r and δr may be used to compute lateral velocity variations and their uncertainties immediately beneath the reflector (Ecevitoglu, 1984). Otherwise, r may be treated as "noise" in the data. We do not expect critical angles for reflections from a depth of 9 km with the recording geometry used for the ADCOH data used in this study. The most common form of noise will undoubtedly be in the form of contamination from overlapping and interfering wavelets. In spite of this, however, excellent results can be recovered using the methods described herein as attested by the agreement between synthetic and real data shown in Figure 16. The agreement provides, therefore, a measure of the interference that can be tolerated and still recover meaningful results.

When using phase spectrum difference techniques in absorption measurements, the phase obtained from the data should be unwrapped prior to the least-squares analysis.

Performance of the dynamic analysis window

The performance of the dynamic window was examined for synthetic data (Figure 17). To test the dynamic window constraints on real data five reflected wavelets were selected from each one of the five reflectors. Portions of the traces that contain these wavelets were shown in Figure 6. Each wavelet was analyzed by the dynamic window. The results are shown in Figure 18, Figure 19, Figure 20, Figure 21, Figure 22 corresponding to the wavelets from reflectors 1, 2, 3, 4, 5, respectively.

The number of traces participating in each SVD computation related to the segments and amplitude and/or phase choices is shown in Table 5. Table 5 also contains minimum, maximum, and average uncertainties in b (amplitude and phase) coming from the data. These uncertainties are needed to estimate the pseudorank during SVD computations. The "Number of Observations" (NOBS) in Table 5 is the number of survivor traces out of about 18,000 (150 shots X 120 traces) into an SVD analysis. First they are visually edited for obviously noisy traces contaminated by noise, surface waves, etc. Then the selection criteria associated with the dynamic analysis window are imposed. NOBS traces survive. Other entries in Table 5 are described elsewhere.

Effect of sampling on the dynamic analysis window

Inspection of Table 4 reveals the difference in value of the Q measurements obtained from amplitude spectrum ratio and Q measurements obtained from phase spectrum difference: The latter is smaller in value than the former. This fact did not show up in the synthetic tests because the purely dispersive phase associated with the synthetic data always began exactly at some integer number of sampling intervals, i.e., the arrival time of a synthetic wavelet coincided exactly with a sample point. For real data, this will not happen, and the initial onset of reflected events will most likely occur in between samples. Thus, a measurement of the phase of a wavelet will include two parts: a small linear phase shift on the order of a fraction of the

sampling interval and a purely dispersive phase. As a result of this, phase measurements are sensitive to the sampling interval, and we believe that there are two reasons for the differences found in Table 4 for Q from amplitude and Q from phase:

1. The time-shifts on the order of fractional sample rates
2. Contamination of the reflected wavelets due to overlap

The first item above may be handled by introducing an extra coefficient in the least-squares expression for the "Phase spectrum difference" technique; i.e., Equation (39):

$$b_P H(-\nu) + 2\pi\tau\nu + r = g(\nu) - f(\nu) \tag{55}$$

where τ is some fraction of the sampling interval, Δt; i.e., 0.42 Δt or 2.673 Δt, and/or by re-sampling the data to smaller sample rates. Preliminary analyses using single-trace synthetic data indicate that both of these criteria, i.e., finer sampling interval and equation (55) will be required; however, resampling the real data for comparable SVD computations is beyond the present memory capacity of our VAX 11/780. If the data contains "noise" in the form of overlapping wavelets then there is nothing much to do at the present stage.

APPLICATIONS TO REAL DATA: THE ADCOH REFLECTION SEISMIC DATA

The ADCOH Project

The ADCOH site selection study is an investigation sponsored by the National Science Foundation in the Piedmont and Blue Ridge of the southeastern United States (Figure 23) for the purpose of siting a 10-km deep hole for scientific purposes. The investigation is a cooperative one by a five-university consortium comprised of the University of Tennessee, Virginia Tech, Princeton, Stanford, and Lamont-Doherty. The project was conceived to be conducted in four overlapping phases: Site selection, engineering design, main phase core drilling, and a post-drilling phase of additional scientific study. The primary objectives of the site study during the first two years were the collection, collation, and interpretation of geological and geophysical data in the site study area, including geologic surface data, gravity, heat flow, in situ stress, and reflection seismic data. The reflection seismic program was divided into three phases:

1. Data acquisition for regional seismic lines,
2. High-resolution,
3. Expanding spread profiles for velocity control.

Phase 1 began on May 1, 1985, and was successfully completed two months later. A portion of these data is used in the present study.

Geologic framework at the ADCOH site

The following discussion is summarized from Costain and others (1986), Çoruh and others (1987), and Hatcher and others (1987). The Appalachian orogen is considered to be one of the classic orogenic belts of the Earth. It has recently been concluded that large portions of the southern Appalachian orogen are allochthonous, and were transported westward along a master decollement beneath the Blue Ridge and much of the Inner Piedmont. The first geophysical evidence for the interpretations of Hatcher (1971, 1972) was provided by Clark and others (1978), and later confirmed by COCORP surveys (Kaufman, 1979; Cook and others, 1979).

If current interpretations of the new ADCOH seismic data are correct, the ADCOH hole will penetrate five major lithotectonic units, in order from top to bottom:

1. Crystalline Inner Piedmont and Chauga belt rocks, including the Brevard fault zone,
2. Allochthonous crystalline basement of Grenville age,
3. Relatively unmetamorphosed Paleozoic paraautochthonous shelf strata (including Knox, Rome Formation, Shady Dolomite equivalents)
4. Eocambrian basin,
5. Autochthonous crystalline basement of Grenville age at 10-12 km.

Each of these units is tectonically separated; confirmation of their thickness and identification by the drill will have important implications for palinspastic reconstructions in the eastern United States. The hole will begin in the crystalline Inner Piedmont (Figure 23).

The ADCOH seismic data

Locations of seismic lines in the ADCOH project site area are shown in Figure 23. Data acquisition for the ADCOH seismic data was done by Western Geophysical under the direction of Virginia Tech. Approximately 113 miles of 30- to 60-fold data were acquired and were processed at Virginia Tech. Acquisition parameters for the ADCOH lines are given in Table 1.

Interpretation of the ADCOH seismic data

A conventional stack of the portion of ADCOH dip Line 1 used in this study is shown in Figure 24 from Çoruh and others (1987). The line is not annotated in order to allow maximum display of the data at this scale. ADCOH Line 1 was acquired over the crystalline Inner Piedmont allochthon. Reflections at times less than 2.6 sec over the southern third of Line 1 are representative of the highly reflective crystalline rocks of the Inner Piedmont. Slight offsets in the continuity of reflections from within the Inner Piedmont block are consistent with a geometry of refolding of early recumbent folds by a later set of reclined to recumbent folds which dominate the outcrop pattern. Shallow (300 m) hole number 4 (Figure 23) in the Inner Piedmont drilled for a heat flow determination (Costain and Decker, 1987) penetrated granitic gneiss and amphibolite; these contrasts are responsible for much of the reflectivity of this part of the Inner Piedmont. At the present stage of our interpretation of the seismic data, the Blue Ridge master (greatest horizontal displacement) decollement is placed at 1.8-2.0 sec beneath station 500, and 2.6 sec beneath station 100 on Line 1. The deeper reflections at 3 sec are interpreted to originate from tectonically imbricated parautochthonous Lower Cambrian Rome Formation and Shady Dolomite. The relatively transparent zone at 2.4-3.0 sec at the southern end of Line 1 above the basal reflections is interpreted to result from a relatively nonreflective interval of Knox dolomite. It may be from this structural and stratigraphic level that exotic slices of upper Knox(?) dolomite (Hatcher and others, 1973) were tectonically

Table 1. Recording Parameters for ADCOH reflection seismic data

Recording parameters	ADCOH
Group int (feet)	220
Channels	120
Fold	60
Vibrators	5
Pilot sweep (Hz)	14-56
Sweep duration (sec)	24
Listening time (sec)	32
60-Hz notch filter on	

transported to the northwest and upward along the Brevard fault zone. The discovery by Hatcher (1971, 1972) of these largely unmetamorphosed platform carbonate slices provided the key that suggested, before any geophysical data were available for this area, that the entire Blue Ridge might be allochthonous.

The Brevard fault zone (Figure 23) is a major linear structural feature of the southern crystalline Appalachians, extending from the Alabama Piedmont to near the Virginia-North Carolina border and perhaps beyond. It is a ductile deformation zone marked by the occurrence of recrystallized mylonitic rocks whose protoliths were graphitic schist, marble, metagraywacke, and metaigneous rocks of granitic composition which form a narrow, but continuous belt. The protoliths of the Brevard sequence are not confined to the Brevard zone (Hatcher, 1971), but the distinctiveness of the zone lies in the continuity of such units within it as well as the intensity of mylonitization. It has experienced a complex history of multiple ductile motions and both prograde and retrograde metamorphism, as well as local late Paleozoic faulting. The persistent, characteristic lithologies in the Brevard zone suggest that this linear feature may be, in part, stratigraphically controlled; the abundance of graphitic schists and phyllites along most of its length suggest that the presence of graphite might have exerted some stratigraphic control over localization of the fault zone. Brittle deformation is confined mostly to the northwestern edge of the zone, and may represent one of the few vestiges of the Alleghanian orogeny in the internal parts of the crystalline southern Appalachians. The tectonic significance of the Brevard fault zone in the numerous models of the southern crystalline Appalachians has varied from model to model since 1905, and the zone remains one of the principal targets of the ADCOH Project.

ADCOH Line 1 intersects the surface trace of the Brevard zone between stations 705 and 710. The BFZ is clearly imaged on ADCOH Line 1 northwest of Westminster. A new conclusion (Çoruh and others, 1987) from the ADCOH seismic data is that the zone appears to merge at depth with the Blue Ridge master decollement at a shallower depth than previously proposed (Cook and others, 1979); i.e., 5 km (1.8-2.0 sec) at Station 500 on ADCOH Line

1. If this interpretation is correct, it implies a thicker section of relatively unmetamorphosed Paleozoic shelf strata above the reflectors at 3 sec.

The wedge of Blue Ridge allochthonous basement to the southeast beneath the Chauga belt is relatively acoustically transparent (ADCOH Line 1). This is a seismic characteristic of Grenville basement reported by others at locations in the southeast United States. It is anticipated that the ADCOH hole will penetrate a relatively thin wedge of allochthonous Grenville basement before entering Paleozoic shelf strata.

Eocambrian(?) rift basins are clearly imaged on both Lines 1 and 3, as, for example, from 3-3.3 sec between stations 455-555 on Line 1. Deeper reflections were recorded from within Grenville basement on the ADCOH lines, but they are considerably weaker and less continuous.

Discussion of the solutions

The ADCOH seismic data used for velocity and Q analyses are shown in Figure 24. The seismic section was partitioned digitally into six intervals separated by five prominent reflections. Reflectors are numbered 1-5 starting from top to bottom (Figure 25). Each reflector was further subdivided into reflecting segments, numbered in increasing order from left to right. Thus, R5S3 refers to reflector 5, segment 3. The depth-velocity tables used in conventional stack and the average velocities obtained using the stack data as the input model to the SVD are shown in Table 7 in the Appendix.

SVD analyses were performed using data from various reflector segments. For example, spatial distribution of velocity and Q from tomographic SVD analyses of reflections from reflector R5S3 using both spectral amplitude ratio and phase difference techniques ("Frequency Domain") are shown in Figure 28. A similar analysis was performed on R4S2 (Figure 29). The high velocities at the left-hand side of Figure 29at 4-6 km may be real or may be an artifact of the solution. This part of the model section is not frequently visited by seismic raypaths; therefore the SVD solution is less reliable (see Figure 34 and Figure 39). In in-

specting a tomographic solution one should not focus on one particular motif. A global view that includes neighboring motifs is a more accurate indication of the best solution. Comparison of solutions from other reflector segments, i.e., from R5S3 and R4S2 (Figure 28 and Figure 29, respectively).

The vibroseis source.

The vibroseis method provides the most controlled land source available. Although each pad position for each sweep of the vibrator undoubtedly results in a different source wavelet, conventional field procedure is to sum individual sweeps from a 4 − or 5 −vibrator array over a distance equal to one station interval (70 meters for the data used in this study). Thus, differences in the source spectrum from station to station are hopefully smoothed out and the spectral content of the source remains essentially constant. Inspection of the shape of the reflected pulse from a single interface generally resembles the autocorrelation of the pilot sweep, so this assumption appears to be justified. In any case, the SVD analysis used in this study would tend to minimize errors due to differences in source and receiver coupling from station to station. This is not to say that the near-field spectrum of the source signature does not change rapidly. Our results, as discussed below, suggest that this is indeed the case. We assume that the spectrum of the source is known. In order to compute Q the initial spectrum of the data at the source must be known, or the spectrum of the reflected wavelet must be compared to that from a shallower reflection. There are advantages and disadvantages for each approach.

Advantages of comparing deeper reflection with shallower reference reflection.

1. Source effects are removed.
2. Low-velocity and low-Q effects of the unconsolidated weathered rocks (saprolite) are removed.
3. Interval Q values may be computed.

4. Lateral changes in Q between the reference reflection and the deeper reflection may be detected if a separate reference reflection is used for each offset.
5. The redundancy in CDP data offers a way of checking interval values of Q for traces in the same CDP gather.

Disadvantages of comparing deeper reflection with shallower reference reflection.

1. Using different wavelets recorded at the same offset may still have different travelpath histories (except at normal incidence) because of the different angles of incidence to each reflector and the consequent possibility of encountering differences in rock type.
2. Uncertainty in the exact arrival time of the shallower reflected reference wavelet. The reference wavelet has also undergone absorption and consequent distortion and delay of peaks and troughs. Note, however, that computation of Q by use of equation (28) is free of concerns about window placement.
3. Requires a different reference wavelet for each CDP.
4. The reference wavelet may be contaminated by overlapping events.

Advantages of comparing deeper reflection with the autocorrelation of the sweep trace (input Klauder wavelet).

1. The input amplitude and phase spectra are completely known.
2. The t_0 "shot" time is the central peak of the input Klauder wavelet.
3. There is no prior traveltime history in the input Klauder wavelet.
4. The same input Klauder wavelet may be used for every trace.
5. The source wavelet is noise-free; i.e., no overlapping event problems.

Disadvantages of comparing deeper reflection with the autocorrelation of the sweep trace (input Klauder wavelet).

1. Source coupling and low-Q, low-velocity highly absorptive surface material (saprolite) cannot be isolated.
2. Only average Q values from the surface to target reflectors may be obtained; however, tomographic solutions may be an alternative if only relative values of Q are of concern.

Time-domain solutions for Q

Single-trace, time-domain solutions for Q are possible by application of the equation

$$Q = \frac{2\tau}{\pi \Delta W} \tag{28}$$

The values so obtained are average values over the ray path. This equation was applied to waveforms on Figure 6.

The source input wavelet for part of this study was determined from the autocorrelation of the vibroseis sweep trace as recorded on the field tapes. This is undoubtedly not the effective source wavelet that propagates from the vibrator pad. In this part of the Piedmont, low-velocity (and low Q) saprolite extends from the surface to maximum depths of about 30 m. The value of Q = 135 as determined from the real data (R5S4) and then used to generate a synthetic wavelet matches the real data extremely well (Figure 16), but the question is, where has most of the absorption taken place? Most of the absorption must be taking place close to the vibrator in the near-surface where we have no reflections that can be used to monitor any rapid changes in Q as a function of depth. The cause may be a combination of coupling effects at the ground surface as well as non-elastic, irreversible deformation associated with the near field. This interpretation is supported by the SVD tomographic results displayed in Figure 28. The SVD solution clearly assigns lower Q values to the uppermost motifs (upper

1.1 km). If the uppermost motifs were to be further subdivided into smaller sized motifs then SVD would undoubtedly be able to continue to assign the lowest Q values to the shallowest (saprolite) depths within the constraints of having a solution with small variance (Appendix 2).

In addition to comparing reflected wavelets with the autocorrelation of the sweep, equation (28) may also be used to compute Q by comparing reflections from deeper reflectors with a reference shallower reflection. This eliminates the effect of the low-Q weathered layer of saprolite at the surface. The results are shown in Table 2. From equation (28) Q is directly proportional to the traveltime, τ, and inversely proportional to the spread of the wavelet. A sampling interval of 4 ms is too large for high-Q rocks because the spread of the wavelet is small and cannot be accurately measured. The data were therefore resampled at a sampling interval of 1 ms. For example, from (28)

$$Q = \frac{2\tau}{\pi \Delta W}$$

or

$$\frac{\Delta W}{\tau} = \frac{2}{\pi Q} = 0.0025 = \frac{2.5\,\text{ms}}{\text{sec}}$$

for Q = 250; i.e., the wavelet breadth increases by 2.5 ms per second of traveltime, and a sampling interval of 4 ms therefore does not provide enough resolution for accurate determinations of ΔW if Q is high.

Iverson (1987) reported that near-surface Q values are often as low as 10, which means that a significant amount of the seismic energy is consumed on the way down and then again on the way up. Winterstein (1987) indicated that energetic surface sources such as vibrators, in combination with sensitives geophones arrayed on the surface, make surface seismic recording possible in areas with highly attenuating near-surface layers.

Interval time-domain Q-values are shown in Table 2. Q determinations having for their basis equation (28) and using reflected waveforms (related shot and channel numbers are

shown on Figure 6) from five different depths compare well with SVD tomographic solutions from SVD methods, as shown in Table 2 and Table 3.

SVD solutions for Q

A summary of the Q determinations from the five reflectors using time domain, frequency domain, and SVD techniques is given in Table 2. Assuming the input wavelet is the autocorrelation of the sweep trace, the results of the determination of Q from both Q_{SVD} (Q_{SVD} = average values of Q using both Q_{amp} and Q_{phase} statistically averaged by equation (54) from the surface to a given reflector), and time-domain (Q_{time} from equation 28) methods are shown in Table 3.. Under the assumption that the reference wavelet is the autocorrelation of the sweep trace, the values of Q are low, lower than would be expected from crystalline rock on the basis of published values. Published values for crystalline rock vary widely (e.g., Waters, 1987, p. 33) from $\cong$ 64-300. The low value of Q = 64 listed by Waters is a determination that was made over a frequency range of 100-200 kHz; all of the other determinations were also made in the kilohertz range.

Values of velocity and Q obtained from spectral methods (Q_{SVD}) using average SVD methods as well as values of Q obtained in the time domain (Q_{time}) from equation (28) are shown in Table 3. They correspond to average values from the surface down to the five principal reflectors shown in the data model (Figure 25). In the table, each velocity-Q pair represents the average physical rock property between the surface and the corresponding reflector, or between two reflectors.

For the *tomographic* results, magnitudes of velocity and Q are proportional to the sizes of the squares (for velocity) and circles (for Q). There are also relative numbers beside them to provide more detail.

All analyses, using either just phase or just amplitude, or both, suggest a low-velocity zone beginning at a depth of about 4-6 km. This is in agreement with geologic interpretations

Table 2. Time domain Q measurements from Equation (28)

Reflector	τ_2	τ_1	W_2	W_1	Q_{time}
R0 - R1	768	0	45	29	31
R0 - R2	1768	0	49	29	56
R0 - R3	2248	0	50	29	68
R0 - R4	3174	0	52	29	88
R0 - R5	3586	0	53	29	95
R1 - R2	1768	768	49	45	159
R1 - R3	2248	768	50	45	188
R1 - R4	3174	768	52	45	219
R1 - R5	3586	768	53	45	224
R2 - R3	2248	1768	50	49	306
R2 - R4	3174	1768	52	49	298
R2 - R5	3586	1768	53	49	289
R3 - R4	3174	2248	52	50	295
R3 - R5	3586	2248	53	50	284
R4 - R5	3586	3174	53	52	262

by Hatcher and others (1987) who interpreted this interval to be made up primarily of the Rome Formation and composed dominantly of lower-velocity shales.

Table 3. Q values relative to pilot sweep as input

Reflector	Segment	Velocity (m/s)	Q_{SVD}	Q_{time}	window (ms)
R0 - R1	R1S2, R1S3	6095	29	31	100
R0 - R2	R2S2, R2S3	5708	53	56	108
R0 - R3	R3S1, R3S2	5607	75	68	116
R0 - R4	R4S2, R4S3	5440	101	88	140
R0 - R5	R5S3, R5S4	5300	141	95	148

Minimum phase absorption

The ADCOH data were recorded at a sampling interval of 4 ms using a sweep of 14-56 Hz. The instrument anti-alias filter starts down at 62.5 Hz with a slope of about 78 db/octave. If the signal-to-noise ratio is high, therefore, it is possible to discard every other sample without introducing aliasing. The Nyquist then becomes 62.5 instead of 125 Hz, and much more of the pure dispersive phase spectrum, B(v), can be recovered between zero and Nyquist. This means that SVD techniques become considerably more sensitive as a larger fraction of the spectrum is spanned.

Examination of the results on Figure 18show that the determination of $Q_{single\text{-}trace}$ frequency-domain computations for the interval from the surface to the first reflector agrees well with the single-trace Q_{time} (Table 2), i.e., $Q_{amp} = 30$, $Q_{phase} = 33$, $Q_{both} = 31$, and $Q_{time} = 31$.

Some general considerations that emerge from a pre-SVD single-trace study of the determination of Q from amplitude ratios and from the phase difference technique are:

1. In all analyses for every reflector, the analysis window was moved from a position that was clearly too early to a position that was clearly too late with respect to the reflected event. Only the panel that brackets the best Q-determinations are shown in Figure 18 through Figure 22, i.e., that satisfies the criteria for the dynamic analysis window. A definitive behavior for Q determined from phase was found in all cases.
2. The sign of $b_P - \delta b_P$ remains negative as the window approaches the correct event arrival time. Near the correct arrival time this quantity becomes briefly positive (over one to three 4-ms sample intervals where the best determination of Q as well as traveltime is found). As the window passes over the correct traveltime then the above quantity again becomes negative until another event is encountered.
3. The phase difference computation thus serves as an event detector and traveltime adjustor. Angeleri and Loinger (1984) note that time delays are introduced by highly attenuating

rocks, and that these delays can effect estimates of velocity and therefore a geologic interpretation.

The constraints involved in the placement of the analysis window were discussed in the section "Procedure". The purpose of the "dynamic analysis window" is to center the window over the absorbed, now asymmetric reflected event in order to recover $B(v)$. The simple visual picks of wavelet arrival time will sometimes be too early, sometimes too late. For an unbiased look at $B(v)$, therefore, one might examine the algebraic sum of $B_i(v)$ for i equal to an arbitrarily large number of traces, and hope that statistically the sum will provide some insight into the shape of $B(v)$ without introducing preconceived constraints. The results are shown in Figure 26a when the dynamic window is out, and Figure 26b when the dynamic window is in. Figure 27 is the enlarged illustration of the last column of Figure 26a which is the result of 12400 (i.e., 6200 traces from forward raypath and 6200 traces from reverse raypath) participating traces. The data are resampled at 8 ms so that the Nyquist of 62.5 Hz almost entirely covers the 14 to 56 effective frequency bandwidth. For absorption that is strictly linear with frequency, we expect the shape of $B(v)$ to be that of equation (12) as illustrated in Figure 3. Considering the limitations of this particular band-limited ADCOH data set, the results are in excellent agreement with this expectation. At this time we cannot say that any significant deviations from (12) as seen on Figure 27 are not real. This is therefore considered to be direct evidence that absorption in rocks is minimum delay.

Figure 27 provides some indication of the relative merits of conventional methods of determining Q using amplitude ratio techniques and this study that introduces the phase domain. If absorption were strictly linear with frequency, if the analysis window were perfectly centered over the absorbed wavelet, and if the data were completely noise-free, then $B(v)$ would be defined by equation (12). The solid line at the top of Figure 27 is the discrete Hilbert transform of the phase curve. The dashed line at the top is the absorption coefficient obtained from the data, again without using any of the analysis window constraints. This dashed line is the conventional method of determining $\alpha(v)$ versus v. Note the slightly more linear $\alpha(v)$

versus v for the phase method suggesting that the phase domain is the better method. The dashed line at the bottom of Figure 27 is the discrete Hilbert transform of the dashed absorption curve. These curves are the average of about 12,400 participant seismic traces. The results shown in Figure 27 are considered to be unbiased in the sense that no constraints were placed on the positioning of the analysis window. The window was simply visually positioned at the approximate arrival time of the reflected event. In spite of this, however, the expected shape of equation (12) has been confirmed. If constraints are placed on the analysis window as described above, the shape of B(v) where the signal-to-noise ratio is good is smooth and well defined (see Figure 26b).

Published values of Q at the ADCOH site are scarce. Chowdhury and Phinney (1987), as a by-product of a pre-processing "spectral shaping", obtained an average value of Q = 250 from an assumed 5 km depth and 5 km/s velocity.

Table 4 provides more detailed results from cumulative SVD computations. These are raw values from individual segments with their uncertainties and their "uncertainty weighted" averages. Results from amplitude only, phase only, and both amplitude and phase are represented.

Some results shown in this section have for their basis the SVD computations using both amplitude and phase methods. The solutions corresponding to amplitude method only or phase method only may be found in Appendix. The amplitude solutions of R4S2 are in Figure 51, and the phase solutions are in Figure 52. The amplitude solutions of R5S3 are if Figure 53, and the phase solutions are in Figure 54.

Table 4. SVD average solutions with pilot sweep used as input

	Raw Values				Weighted Average		
	Both	Amplitude	Phase		Both	Amplitude	Phase
R1S2	6101 ± 14	6063 ± 14	6119 ± 14	R1	6095	6057	6113
	28 ± 0.4	65 ± 1	15 ± 0		29	64	16
R1S3	6089 ± 16	6050 ± 16	6106 ± 17	R2	5708	5692	5701
	30 ± 1	63 ± 1	16 ± 0		53	171	28
R2S2	5704 ± 11	5685 ± 7	5704 ± 4	R3	5607	5570	5542
	54 ± 1	171 ± 4	28 ± 0		75	225	40
R2S3	5719 ± 26	5709 ± 17	5692 ± 10	R4	5440	5403	5445
	51 ± 2	172 ± 4	27 ± 0		101	299	52
R3S1	5634 ± 48	5579 ± 35	5558 ± 10	R5	5300	5285	5296
	72 ± 10	224 ± 14	41 ± 2		141	355	65
R3S2	5593 ± 24	5566 ± 16	5534 ± 5				
	76 ± 4	226 ± 6	40 ± 1				
R4S2	5451 ± 2	5411 ± 2	5457 ± 2				
	101 ± 1	312 ± 3	48 ± 1				
R4S3	5418 ± 4	5386 ± 4	5428 ± 3				
	100 ± 2	285 ± 3	55 ± 1				
R5S3	5345 ± 3	5335 ± 3	5347 ± 3				
	144 ± 2	370 ± 5	66 ± 1				
R5S4	5225 ± 5	5202 ± 5	5229 ± 4				
	135 ± 4	325 ± 10	64 ± 2				

Table 5. Number of observations and uncertainty in b

Reflector Segment	Number of Observations, m (NOBS)	δb_{min} (BMIN)	δb_{max} (BMAX)	δb_{ave} (BAVE)
R4S2B	1259	0.099	0.07	0.03
R5S3B	1499	0.006	0.05	0.02
R4S2A	1720	0.002	0.04	0.01
R5S3A	1566	0.002	0.04	0.01
R4S2P	2216	0.009	0.08	0.04
R5S3P	1610	0.01	0.09	0.04

SUMMARY AND CONCLUSIONS

This study has resulted in the discovery of an exact method for the theoretical formulation of the effects of intrinsic damping where the attenuation coefficient, $\alpha(\nu)$, is an arbitrary function of the frequency, ν. Absorption-dispersion pairs are computed using numerical Hilbert transformation; approximate analytical expressions that require the selection of arbitrary constants and cutoff frequencies are no longer necessary. The application of the numerical Hilbert transform avoids difficulties encountered by others who used aperiodic analytical approximations to determine absorption-dispersion pairs.

In this study, the dispersive body wave velocity, $p(\nu)$, is found to be

$$p(\nu) = \frac{p(\nu_N)}{1 + \frac{1}{2Q}\frac{H(-\nu)}{\nu}} \tag{21}$$

where H denotes numerical Hilbert transformation, $p(\nu)$ is the phase velocity at the frequency ν, and $p(\nu_N)$ is the phase velocity at Nyquist. From (21) it is possible to estimate Q in the time domain by measuring the amount of increase, ΔW, of the wavelet breadth after a traveltime, τ, by

$$Q = \frac{2\tau}{\pi \Delta W}. \tag{28}$$

The inverse problem, i.e., the determination of Q and velocity has also been investigated using singular value decomposition (SVD). The sparse matrices encountered in the acquisition

of conventional reflection seismology data result in a system of linear equations of the form $AX = B$, with A the design matrix, X the solution vector, and B the data vector. The system of normal equations is $A^TAX = A^TB$ where the least-squares estimate of $X = \hat{X} = V\frac{1}{S}U^TB$ and the SVD of A is $A = USV^T$.

Excellent reflections from crystalline rocks in South Carolina yield values of Q in the range $Q = 250 - 300$ from an application of (28). Tomographic solutions have the advantage of detecting local changes in Q. The analysis techniques discussed herein appear to be robust even when there is considerable overlap and interference between the target wavelets.

This study may be the first to detect directly body wave dispersion from conventional reflection seismology data. As shown on Figure 27, the expected approximate shape of the dispersive phase (equation 12) was recovered from the data.

The direct detection of body wave dispersion from conventional vibroseis data may be useful for distinguishing between those crustal volumes that are potentially seismogenic and those that are not. Such differences may be due to variations in fracture density and therefore water content (Costain and others, 1987) in the crust.

One other application of SVD techniques is potentially important. One of the most important geological problems in the southeastern U.S. at the present time is the identification and understanding of the role of major dextral strike-slip faulting in the architecture of the Appalachian orogen. Many major strike-slip fault zones are steep to vertical, and are not normally considered to be good targets for reflection seismology. The nature of the SVD techniques discussed herein, however, suggests a possible way to study those structural features that contain steep to vertical boundaries. As long as raypaths pass through the rock volume of interest, it is possible by SVD tomography to extract information about physical properties such as velocity or Q from those rock volumes. Furthermore, as long as raypaths cross the vertical boundary, reflectors are necessary only on one side, not both, of the reflecting boundary; i.e., as would be expected with a major strike-slip fault, reflectors do not have to be continuous across the structural discontinuity.

REFERENCES

Aki, K. and P.G. Richards, 1980, Quantitative Seismology - Theory and Methods, W.H. Freeman and Company, New York, Volume 1, 557 pp.

Anderson D.L., and J.B. Minster, 1979, The frequency dependence of Q in the earth and implications for mantle rheology and Chandler wobble, Geophys. J., 58, 431.

Anderson, D.L., and R.S. Hart, 1978, Q of the earth: J. Geophys. Res., 83, 5869-5882.

Angeleri, G. P., and E. Loinger, 1984, Phase distortion due to absorption in seismograms and VSP, Geophysical Prospecting, v. 32, 406-424.

Azimi, Sh. A., A.V. Kalinin, V.V. Kalinin, and Pivovasov, Impulse and transient characteristics of media with linear and quadratic absorption laws.

Badri, M., and H.M. Mooney, 1987, Q measurements from compressional seismic waves in unconsolidated sediments: Geophysics, 52, 772-784.

Berckhemer, H., F. Auer, and J. Drisler, 1979, High temperature anelasticity and elasticity of mantle peridotite: Phys. Earth Planet. Interiors, 20, 48.

Bishop, T.N., K.P. Bube, R.T. Cutler, R.T. Langan, P.L. Love, J.R. Resnick, R.T. Shuey, D.A. Spindler, and H.W. Wyld, 1985, Tomographic determination of velocity and depth in laterally varying media: Geophysics, 50, 903-923.

Bjorck, Ake, 1976, Methods for sparse linear least squares problems: Sparse Matrix Computations (Edited by James R. Bunch and Donald J. Rose), Academic Press Inc., 177-199.

Blair, D.P., and A.T. Spathis, 1984, Seismic source influence in pulse attenuation studies: J. Geophys. Res., 89, 9253-9258.

Brune, J.N., 1968, Seismic moment, seismicity, and rate of slip along major fault zones: Journal of Geophysical Research, 73, 777-784.

Brillouin, L., 1960, Wave Propagation and Group Velocity. Academic Press, 154 p.

Bolduc, P.M., R.M. Ellis, and R.D. Russell, 1972, Determination of the seismograph phase response from the amplitude response: Bull. of the Seism. Soc. of Amer, 62, 1665-1672.

Chowdhury, K.R., and R.A. Phinney, 1987, Improved resolution of reflections from the crystalline upper crust: Geophys. J. R. astr. Soc., 89, 35-40.

Claerbout, J.F., 1985, Fundamentals of geophysical data processing: Blackwell Scientific Publications.

Clark, H.B., J.K. Costain, and L. Glover, III, 1978, Structural and seismic reflection studies of the Brevard ductile deformation zone near Rosman, North Carolina, Amer. J. Sci., v. 278, 419-441.

Cook, F.A., D.S. Albaugh, L.D. Brown, S. Kaufman, J.E. Oliver, and R.D. Hatcher, 1979, Thin-skinned tectonics in the crystalline southern Appalachians; COCORP seismic reflection profiling of the Blue Ridge and Piedmont, Geology, v. 7, 563-567.

Çoruh, C, Costain, J.K., Hatcher, R.D., Jr., Pratt, T.L., Williams, R.T., and Phinney, R.A., 1987, Results from regional vibroseis profiling: Appalachian ultra-deep core hole site study, *in* Deep Seismic Reflection Profiling of the Continental Lithosphere, edited by D. Matthews and C. Smith, Special Issue of the Geophysical Journal of the Royal Astronomical Society, v. 89, 147-156.

Costain, J.K., C. Çoruh, T. Pratt, R.D. Hatcher, Jr., L. Glover, III, R. Phinney, J. Diebold, R. Williams, and M. Zoback, 1986, Seismic signatures of tectonic lithofacies from regional lines, Appalachian Ultradeep Core Hole Site Area, Society Exploration Geophysicists Extended Abstracts with Biographies, 1986 Technical Program, p. 136-139.

Costain, J. K. and E. R. Decker, 1987, Heat flow at the proposed Appalachian Ultradeep Core Hole (ADCOH) Site: Tectonic Implications, *Geophys. Res. Letters*, No. 14, v. 3, 252-255.

Costain, J.K., Bollinger, G.A., and Speer, J.A., 1987, Hydroseismicity: A hypothesis for the role of water in the generation of intraplate seismicity, *Seismological Research Letters*, v. 58, No. 3, in press.

Duff, I.S. and J.K. Reid, 1976, A comparison of some methods for the solution of sparse overdetermined system of linear equations: J. Inst. Maths Applics, 17, 267-280.

Ecevitoglu, Galip Berkan, 1984, Use of wavelet distortion from supercritical reflections to detect lateral velocity variations, M.S. Thesis in Geophysics, Virginia Polytech Institute and State University, Blacksburg, 24061.

Ecevitoglu, B.G., and Costain, J.K., 1985, Measurement of absorption from the phase spectrum of a reflected source wavelet, EOS (Transactions of the American Geophysical Union), v. 66, No. 46, p. 984.

Ecevitoglu, B.G., 1987, Velocity and Q from multifold seismic data using SVD, Ph.D. Dissertation in Geophysics, Virginia Polytechnic Institute and State University, Blacksburg, 24061.

Forsythe, G.E., M.A. Malcolm and C.B. Moler, 1977, Computer Methods for Mathematical Computations: Prentice-Hall Inc., 259 p.

Futterman, W.I, 1962, Dispersive body waves, Journal of Geophysical Research, v. 67, 5279-5291.

Gardner G. H. F., M. R. J. Wyllie, and D. M. Droschak, 1964, On the attenuation of elastic waves in sands: Jour. Pet. Tech., 16, 189-198.

Gentleman, W.M., 1973, Least squares computations by Givens transformations without square roots: J. Inst. Maths Applics, 12, 329-336.

George, A., and M.T. Heath, 1980, Solution of sparse linear least squares problems using Givens Rotations: Linear Algebra and its Applications, 34, 69-83.

Gill, P.E., and W. Murray, 1976, The orthogonal factorization of a large sparse matrix: Sparse Matrix Computations (Edited by James R. Bunch and Donald J. Rose), Academic Press Inc., 201-211.

Gladwin, M.T., and F.D. Stacey, 1974, Anelastic degradation of acoustic pulses in rock: Phys. Earth Planet. Int., 8, 332-336.

Golub, G., 1965, Numerical methods for solving linear least squares problems: Numerische Mathematik, 7, 206-216.

Golub, G.H., and C.F. Van Loan, 1983, Matrix Computations: Johns Hopkins Press, 476 p.

Gordon, R.B. and L.A. Davis, 1968, Velocity and attenuation of seismic waves in imperfectly elastic rock: J. Geophys. Res., 73, 3917.

Gutenberg, B., 1959, Physics of the Earth's Interior: Academic Press, New York.

Hatcher, R.D., Jr., 1971, Stratigraphic, structural, and petrologic evidence favoring a thrust solution to the Brevard problem: Amer. J. Sci., v. 270, 177-202.

Hatcher, R.D., Jr., 1972, Developmental model for the southern Appalachians: Geol. Soc. Amer. Bull., v. 83, 2735-2760.

Hatcher, R.D., Jr., 1973, Basement versus cover rocks in the Blue Ridge of northeast Georgia and adjacent North Carolina: Amer. J. Sci., v. 273, 671-685.

Hatcher, R.D., Jr., 1978, The Alto allochthon: A major tectonic feature of the Piedmont of northeast Georgia, Georgia Geol. Survey Bull., v. 93, 83-86.

Hatcher, Jr., R.D., Costain, J.K., Çoruh, C., Phinney, R.A., and Williams, R.T., 1987, Tectonic implications of new Appalachian ultradeep core hole (ADCOH) seismic reflection data from the crystalline southern Appalachians, *in* Deep Seismic Reflection Profiling of the Continental Lithosphere, edited by D. Matthews and C. Smith, Special Issue of the Geophysical Journal of the Royal Astronomical Society, v. 89, 157-162.

Iverson, W.P., 1987, Combining attenuation by Q and spherical divergence: Geophysics, 52, 740-744.

Jensen J.R., 1986, Introductory digital image processing, Prentice-Hall Inc., 379 p.

Kak, S.C., 1970, The discrete Hilbert Transform: Proceedings of the IEEE, 585-586.

Kanamori, H., and D.L. Anderson, 1977, Importance of physical dispersion in surface wave and free oscillation problems: Reviews of Geophysics and space physics, 15, 105-111.

Kaufman, S., 1979, COCORP southern Appalachian data, Geophysics, p. 44, 1598-1599.

Kjartansson, E., 1979, Constant Q wave propagation and attenuation. Journal of Geophysical Research, 84, 4737-4748.

Knopoff, L. and G.J.F. MacDonald, 1958, Attenuation of small amplitude stress wave in solids: Revs. Modern Phys., 30, 1178-1192.

Lawson, C.L., and R.J. Hanson, 1974, Solving Least Squares Problems: Prentice-Hall, Inc., 340 p.

Lines, L.R., and S. Treitel, 1985, Inversion with a grain of salt: Geophysics, 50, 99-109.

Liu, H.P., D.L. Anderson, and H. Kanamori, 1976, Velocity dispersion due to anelasticity; implications for seismology and mantle composition: Geophys. J. of the Royal Astr. Soc., 47, 41-58.

Luh, P.C., 1977, A scheme for expressing instrumental responses parametrically: Bull. of the Seism. Soc. of Amer., 67, 957-969.

McDonal, F.J., Angona, F.A., Mills, R.L., Sengbush, R.L., Van Nostrand, R.G., and White, J.E., 1958, Attenuation of shear and compressional waves in Pierre Shale, Geophysics, v. 23, 421-439.

Meissner, R., 1986, The continental Crust: A Geophysical approach: Academic Press Inc.

Menke, W., 1984, Geophysical Data Analysis: Discrete Inverse Theory: Academic Press, Inc., 260 p.

Muckelmann, R., 1982, Tech. Prog. Abstr. SEG, Dallas, Texas, 141-143.

Nolet, Guust, 1985, Solving or resolving inadequate and noisy tomographic systems: Journal of Computational Physics, 61, 463-482.

Pandit, B.I. and J.C. Savage, 1973, An experimental test of Lomnitz's theory of internal friction in rocks: J. Geophys. Res., 78, 6097.

O'Doherty R.F., and N.A. Anstey, 1971, Reflections on amplitudes: Geophysical Prospecting, 19, 430-458.

Peterson, J.E., Bjorn N. P. Paulsson, and Thomas V. McEvilly, 1985, Applications of algebraic reconstruction techniques to crosshole seismic data: Geophysics, 50, 1566-1580.

Ricker, N.H., 1977, Waves in viscoelastic media: Elsevier.

Schoenberger, M., and F. K. Lewin, 1974, Apparent attenuation due to intrabed multiples: Geophysics, 39, 278-291.

Sherwood, J.W.C., and A. W. Trorey, 1965, Minimum phase and related properties of the response of a stratified absorptive earth to plane acoustic wave: Geophysics, 30, 191-197.

Solomon, S.C., 1972, On Q and seismic discrimination: Geophys. J., 31, 163.

Strick, E., 1970, A predicted pedestal effect for pulse propagation in constant-Q solids. Geophysics, 35, 387-403.

Spencer, W., Jr., 1981, Stress Relaxations at low frequncies in fluid-saturated rocks: Journal of Geophysical Research, 86,1083.

Strick, E., The determination of Q, dynamic viscosity, and transient creep curves from wave propagation measurements. Geophys. J.R. Astr. Soc., 13, 197-218.

Strick, E., 1973, Discussion on "Proposed attenuation-dispersion pair for seismic waves," (J.E. White and D.J. Walsh). Geophysics, 423-429.

Takano, K., 1971, A note on the attenuation of short period P and S waves in the mantle, J. Phys. Earth, 19, 155.

Taner, M.T., F. Koehler, R.E. Sheriff, 1979, Complex seismic trace analysis: Geophysics, 44, 1041-1063.

Teng, Ta-Liang, 1968, Attenuation of body waves and the Q structure of the mantle: Journal of Geophysical Research, 73, 2195-2208.

Tittmann, B. R., L. Ahlberg, and J.Curnow, 1976, Internal friction and velocity measurements: Proc. Lunar Sci. Conf., 7th, 3123-3132

Tittmann, B.R., V.A. Clark, J.M. Richardson, and T.W. Spencer, 1980, Possible mechanism for seismic Attenuation in rocks containing small amounts of volatiles: Journal of Geophysical Research, 85, 5199-5208.

Toksoz, M.N., D.H. Johnston, and A. Timur, 1979, Attenuation of seismic waves in dry and saturated rocks, I, Laboratory measurements: Geophysics, 44, 681, 1979.

Trorey, A.W., 1962, Theoretical Seismograms with frequency and depth dependent absorption: Geophysics, 27, 766-785.

Cizek, V., 1970, Discrete Hilbert transform: IEEE transactions on audio and electroacoustics, V. AU-18, 340-343.

Ward, R.W., and Chi-Yuh Young, 1980, Mapping seismic attenuation within geothermal systems using teleseisms with application to the geysers-clear lake region: Journal of Geophysical Research, 85, 5227-5236.

Waters, K.H., 1987, Reflection Seismology: John Wiley and Sons, 3rd Edition, Third Edition, 538 p.

White, J.E., 1972, and D.J. Walsh, Proposed attenuation-dispersion pair for seismic waves, Geophysics, 37, 456-461.

Winterstein, D.F., 1987, Vector attenuation: Some implications for plane waves in anelastic layered media: Geophysics, 52, 810-814.

Wuenschel, P.G., 1965, Dispersive body waves - An experimental study. Geophysics, 30, 539-551.

Yoshida M., and M. Tsujira, 1975, Spectrum and attenuation of multiply reflected core phases: J. Phys. Earth, 23, 31.

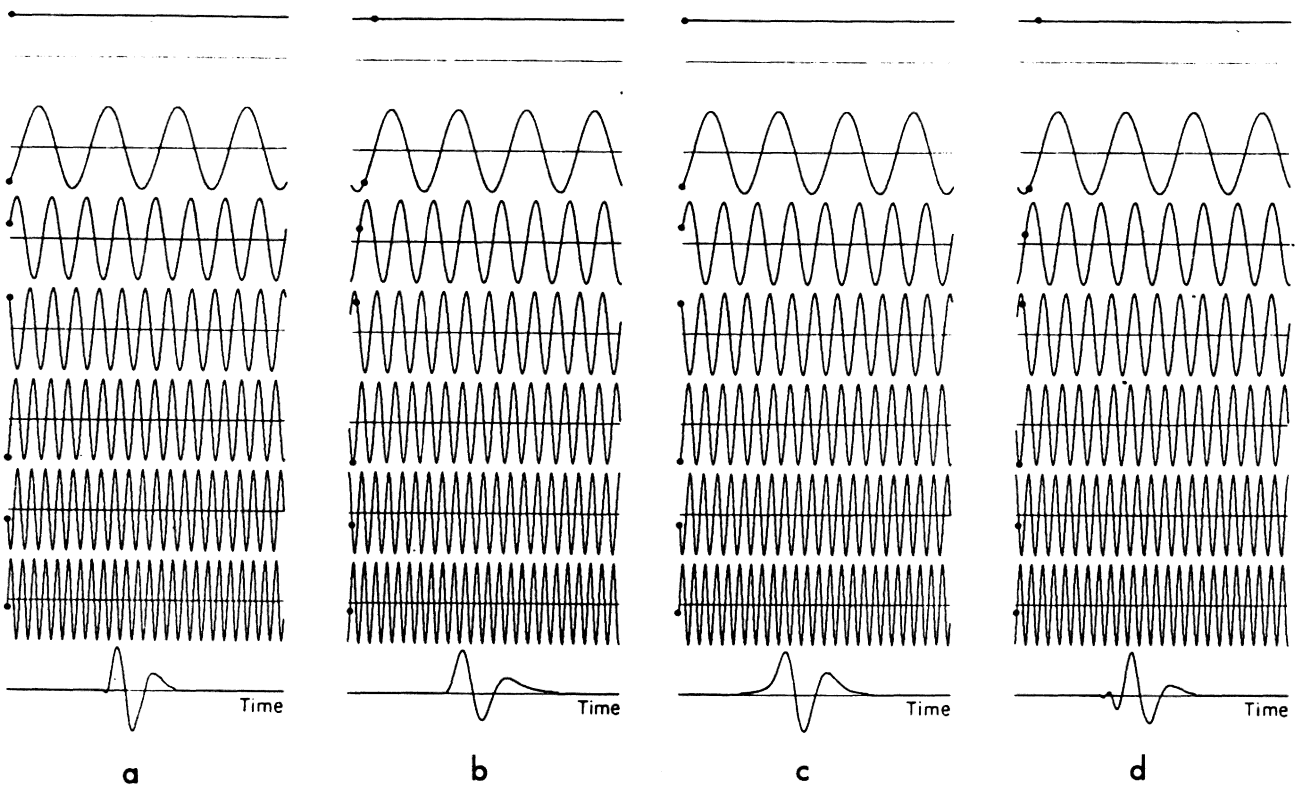

Figure 1. Illustration of causal absorption with sinusoids: (a) The input wavelet. Observe the bullets (time-markers) on each sinusoid is left justified. (b) The output wavelet is subject to both absorption and dispersion. Note that absorption increased the wavelet, and the accompanying dispersion kept the wavelet causal. The bullets indicate time-delays applied to each sinusoid as a result of the dispersion. (c) The output wavelet is subject to absorption only. Note the overshoot of the wavelet onset toward negative time violating the causality principle. Since no dispersion is considered, the bullet stays left justified indicating no time-delay. (d) The output wavelet is subject to dispersion only. Again, note the overshoot of the wavelet onset toward negative time and the increase in wavelet breath not caused by absorption. The displacement of the bullets indicates the time-delays. Therefore, absorption and dispersion must coexist. The sinusoids are kept at the same amplitudes for display purposes.

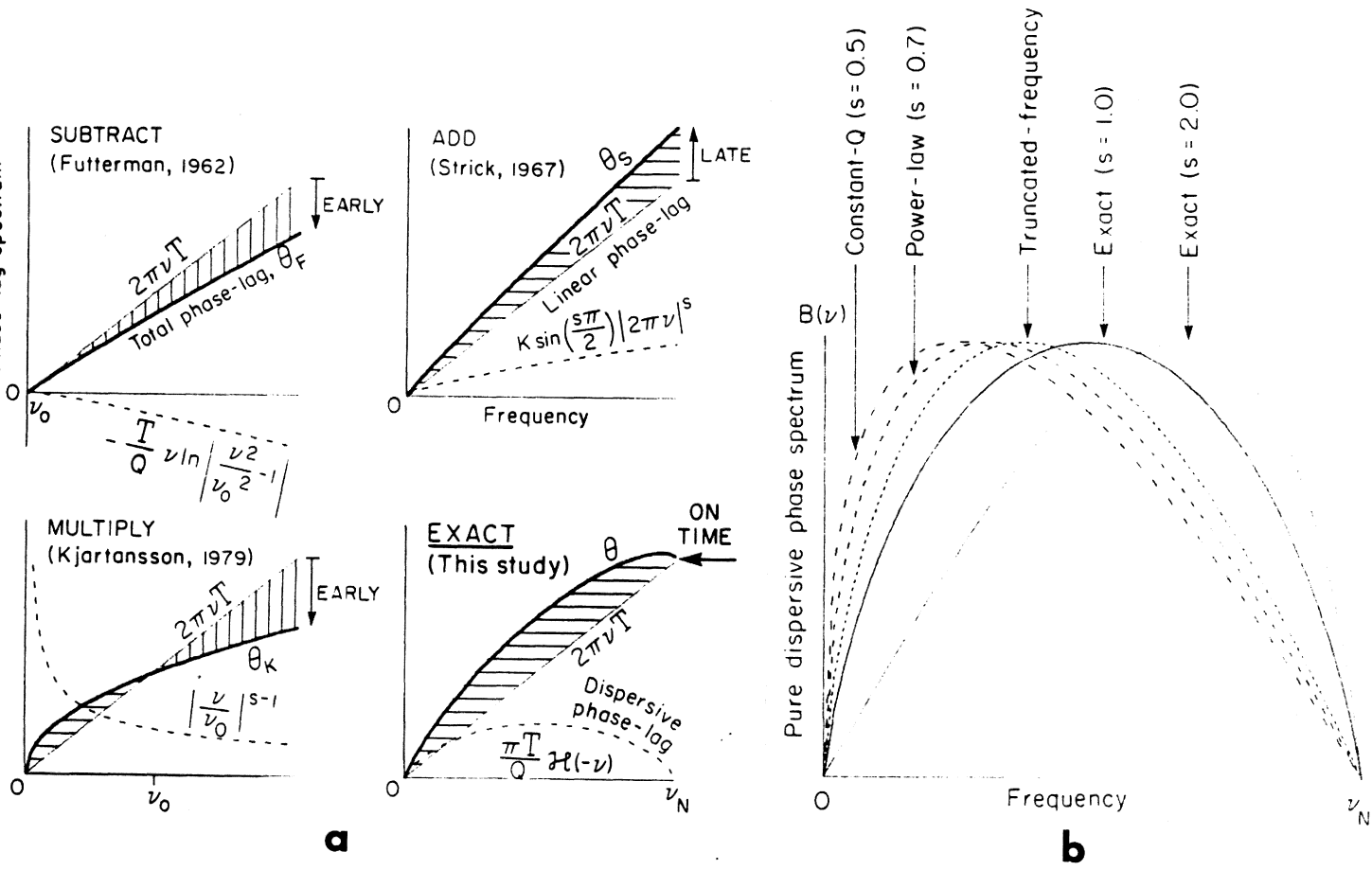

Figure 2. Graphic summary of phase definitions of Futterman (1962), Strick (1970), Kjartansson (1979), and this study. (a) The phase-lag curves; (b) Linear phase subtracted. A value of s = 1 means an absorption coefficient that is linear with frequency; thus, s = 1 divides absorption coefficients between $0 < s < 1$ and $s > 1$. Note that for $s > 1$ the dispersive phase is tilted toward the right and for $s < 1$ dispersive phase is tilted toward the left. For s = 1 the dispersive phase is symmetrical.

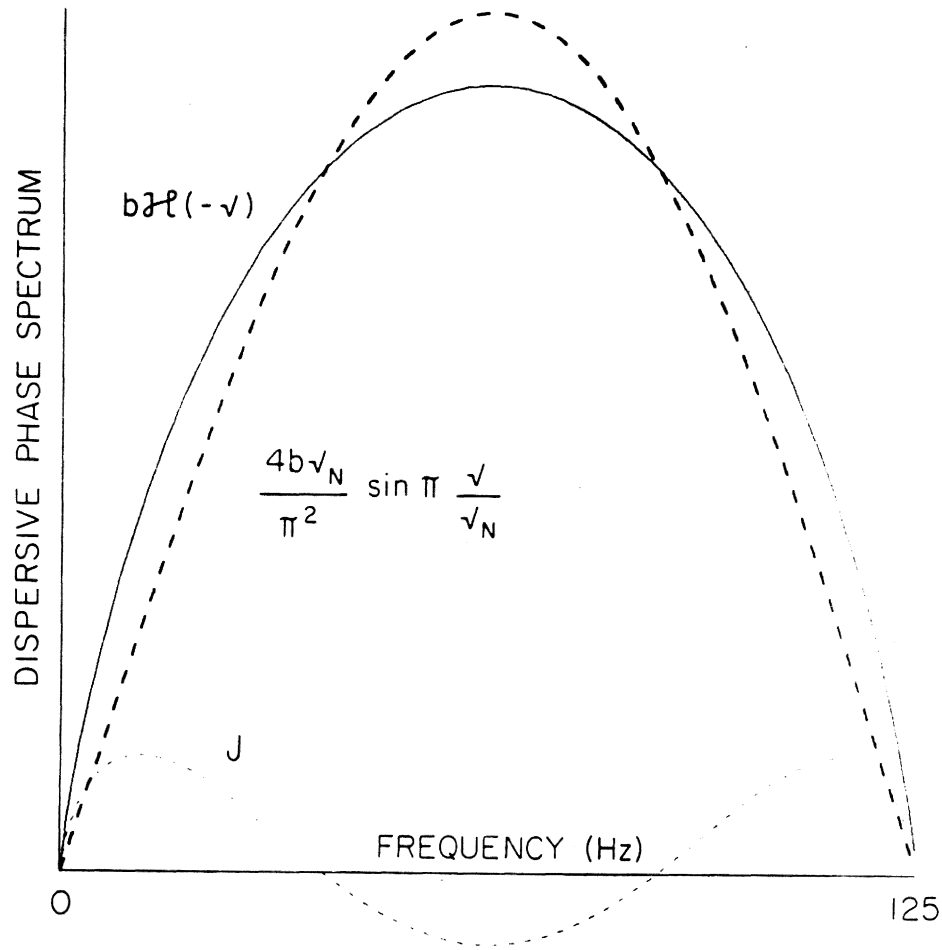

Figure 3. The dispersive phase spectrum: Heavy solid line is the dispersive phase curve (equation 12); dashed line is the dominant half-period sine wave (sine term in equation 12); thin dashed line is the deduced shape of the entire perturbing series terms (J in equation 12).

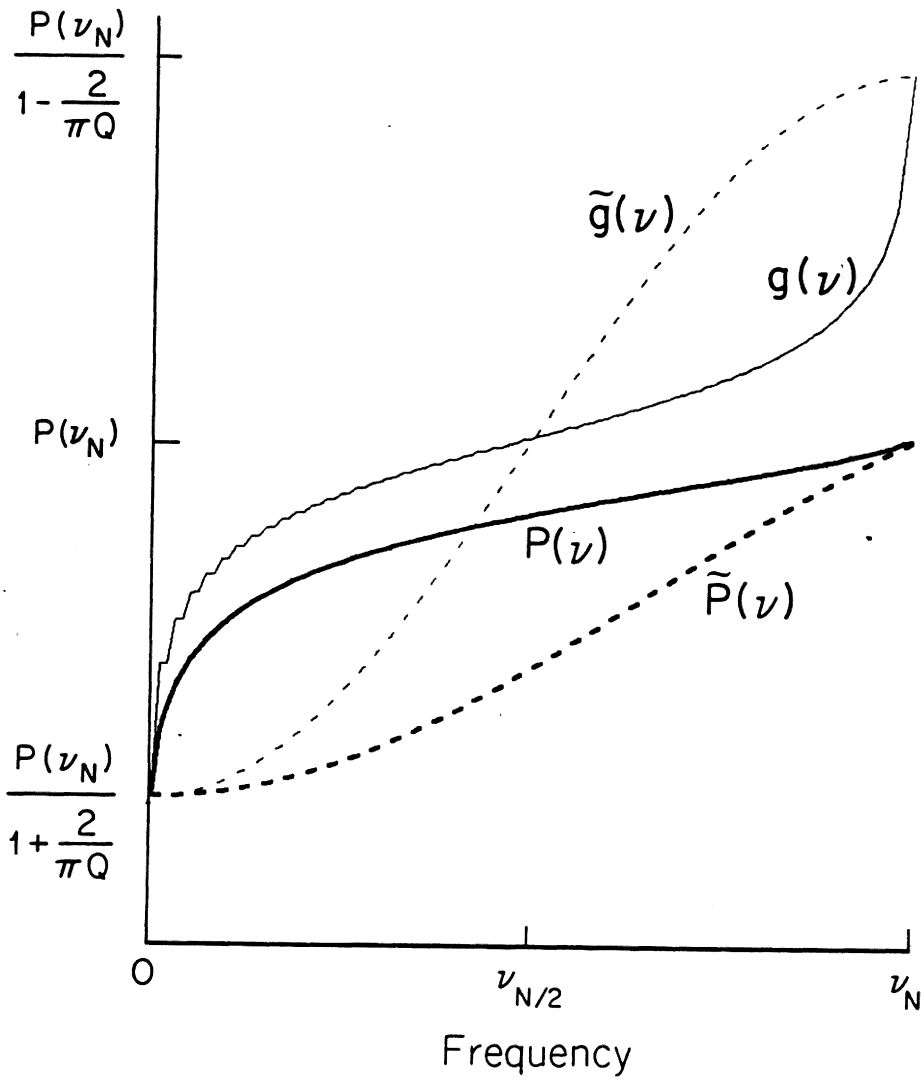

Figure 4. The phase and group velocities: Heavy solid line is the exact dispersive phase velocity; thin solid line is the exact group velocity; heavy dashed line is the approximate dispersive phase velocity; thin dashed line is the approximate group velocity.

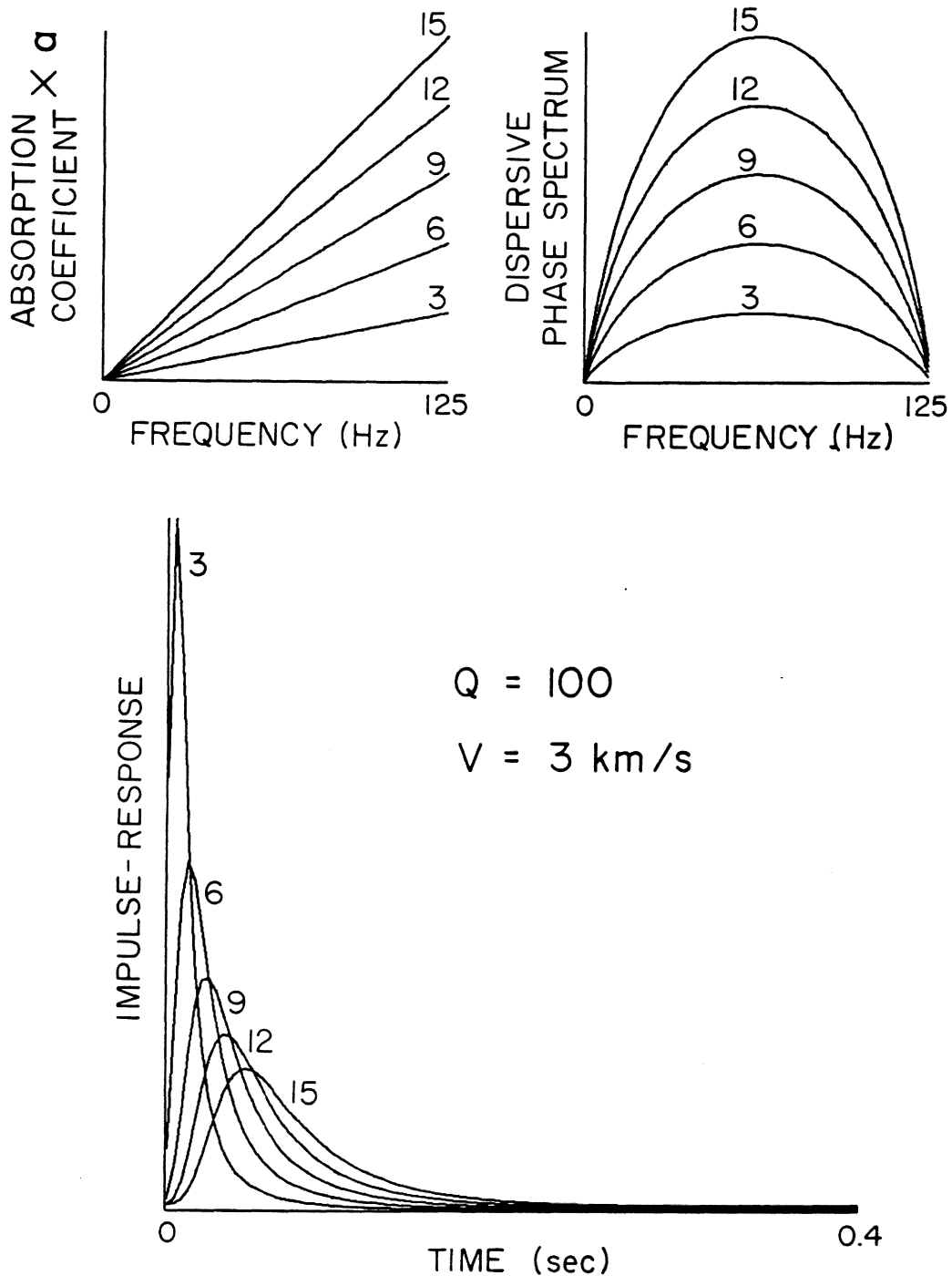

Figure 5. Different magnitudes of causal absorption: Different levels of causal absorption are illustrated in absorption coefficients, dispersive phases, and impulse-responses for distances a = 3, 6, 9, 12, and 15 km. Note that absorption coefficient is multiplied by the distance traveled a. Observe the scaling and broadening effects on the impulse-responses. Note that when $\alpha(\nu)a$ versus ν becomes steeper, then the dispersive phase $B(\nu)$ becomes larger so that the peak of the pulse in the time domain is gradually delayed.

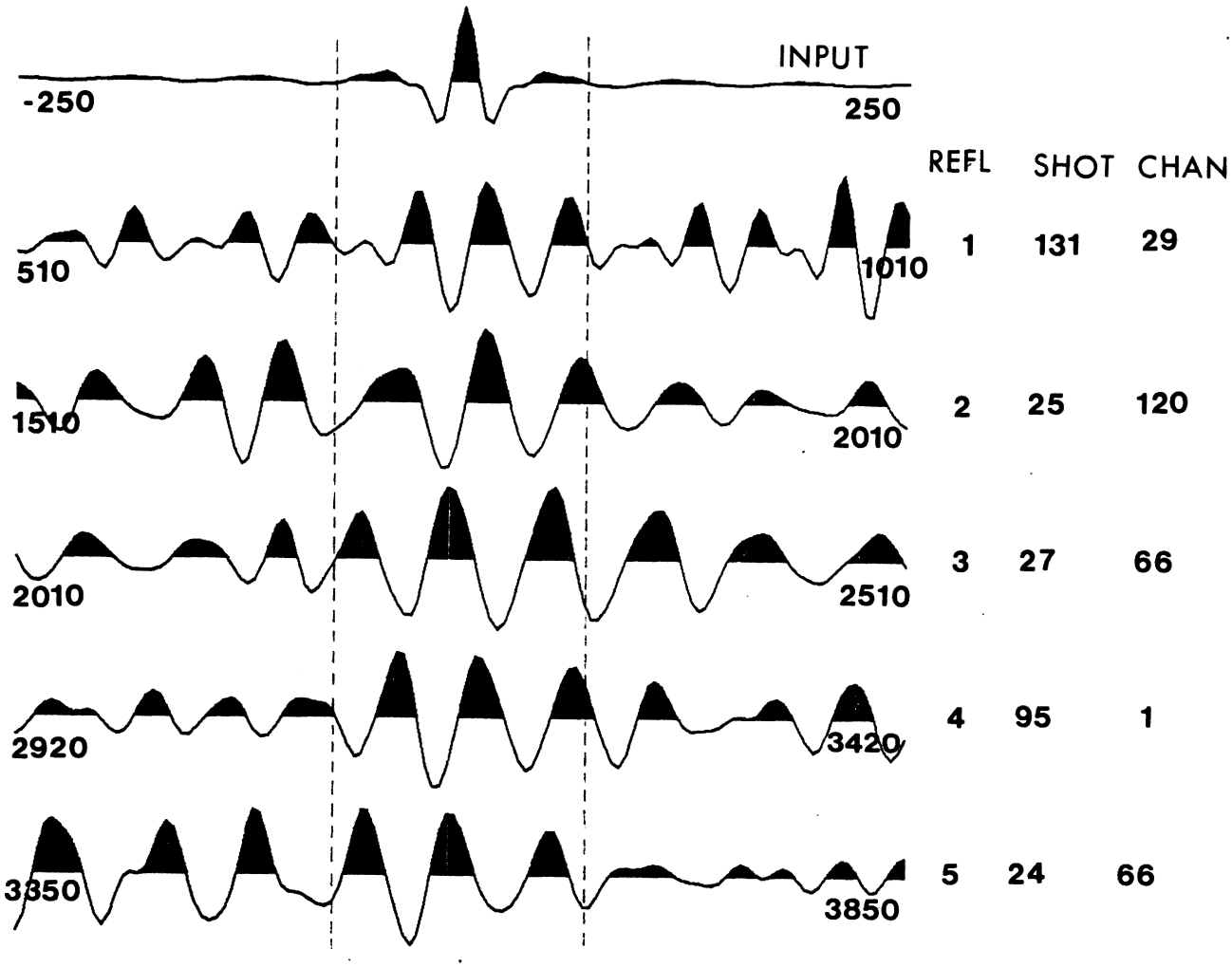

Figure 6. Real data from each reflector: 500 ms time gates from real data related to each reflector. Vertically drawn dashed lines indicates the approximate locations of the reflected events.

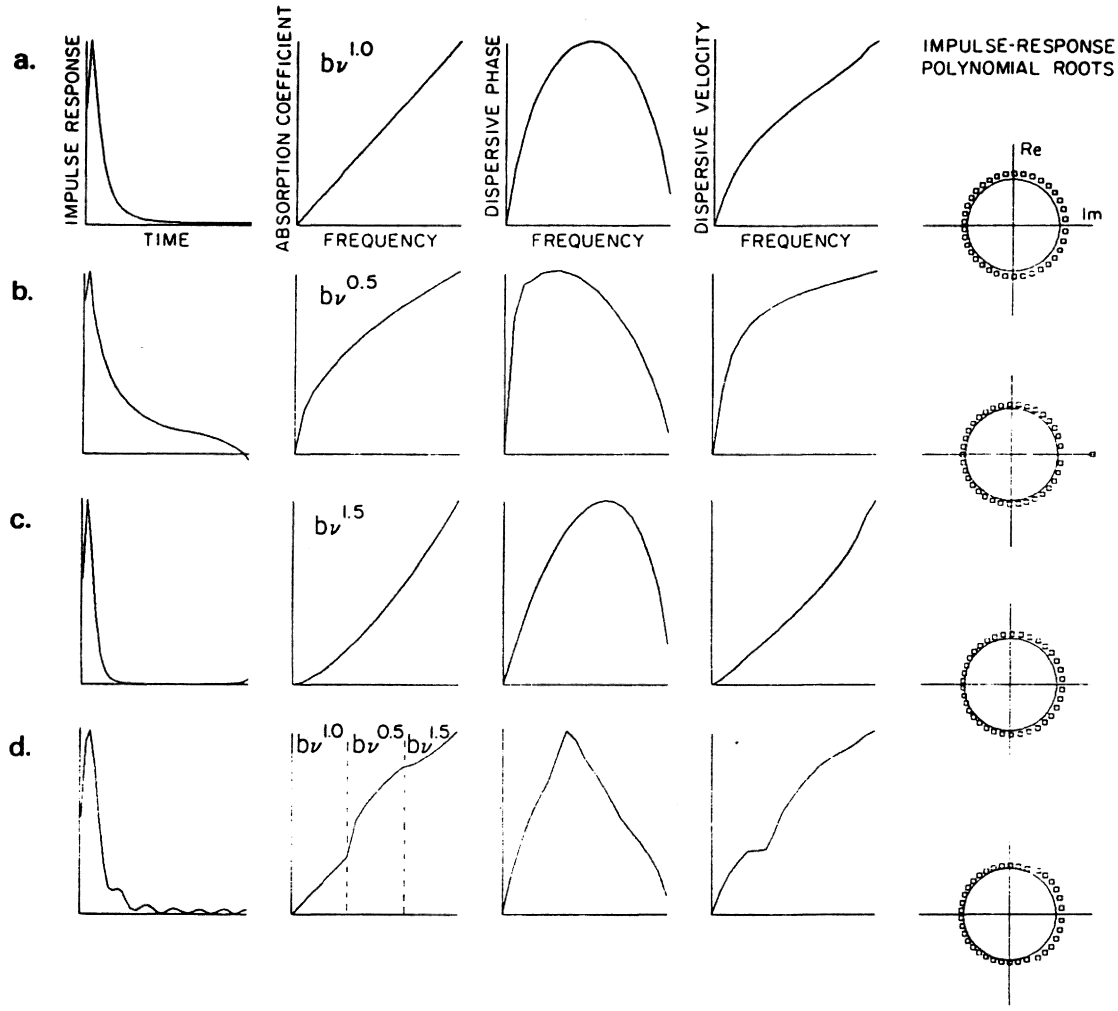

Figure 7. Power-law attenuation models: (a) Power = 1.0. Observe the symmetry of the dispersive phase. (b) Power = 0.5. Observe the tilt of the dispersive phase to the left. (c) Power = 1.5. Observe the tilt of the dispersive phase to the right. (d) Power is the combination of (a), (b), and (c). Note that all the roots are outside the unit circle; hence, all impulse-responses are causal and minimum-delay as predicted by Kolmogorov's condition.

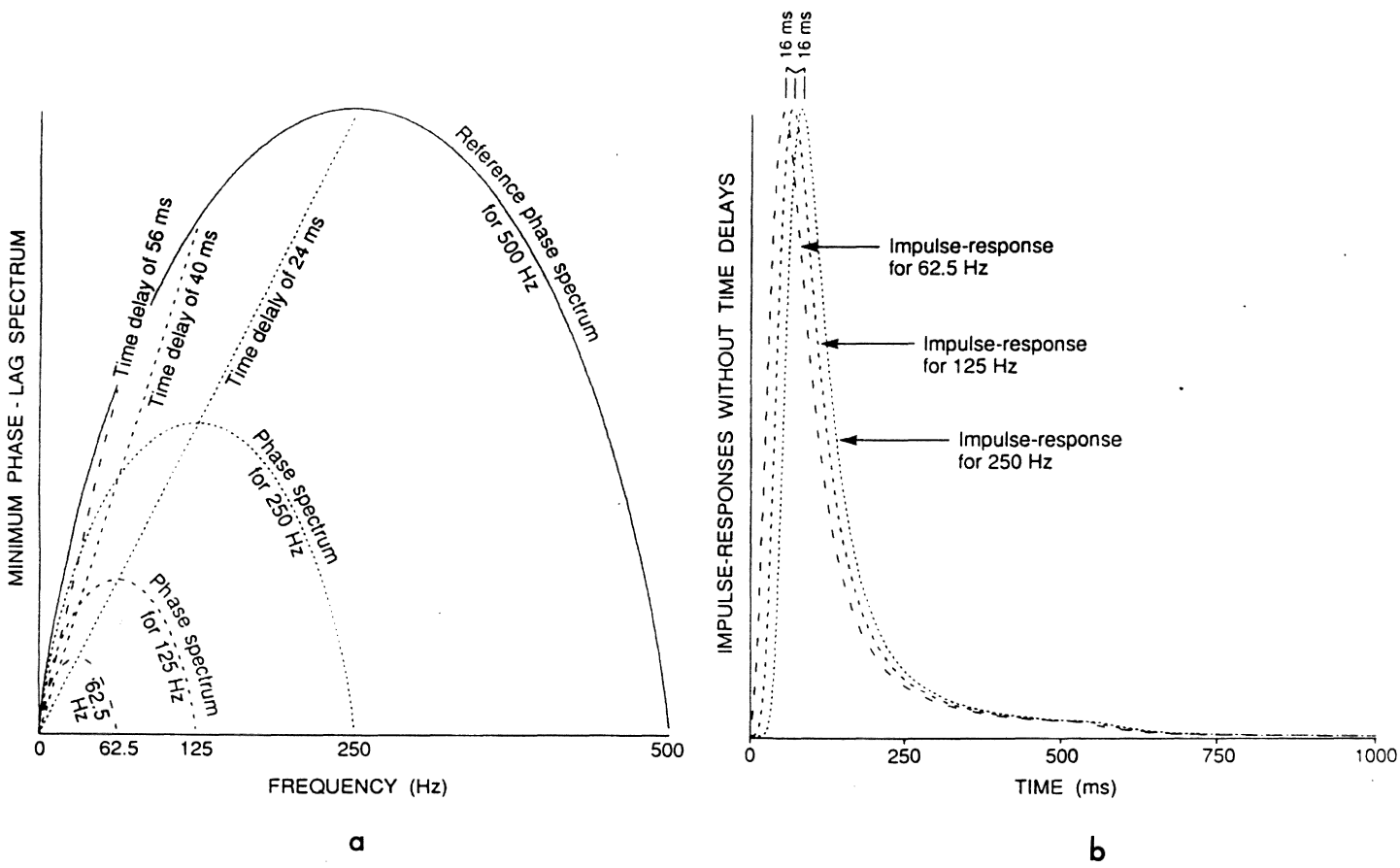

Figure 8. **Effect of different Nyquist frequencies (Power = 1.0, without time-delays):** Left sides are the dispersive phase spectra respective to each cut-off frequency. Straight lines show the corresponding time-delays to be applied. Right sides are the corresponding impulse-responses. Note that they are merely shifted with respect to each other by a constant amount of time.

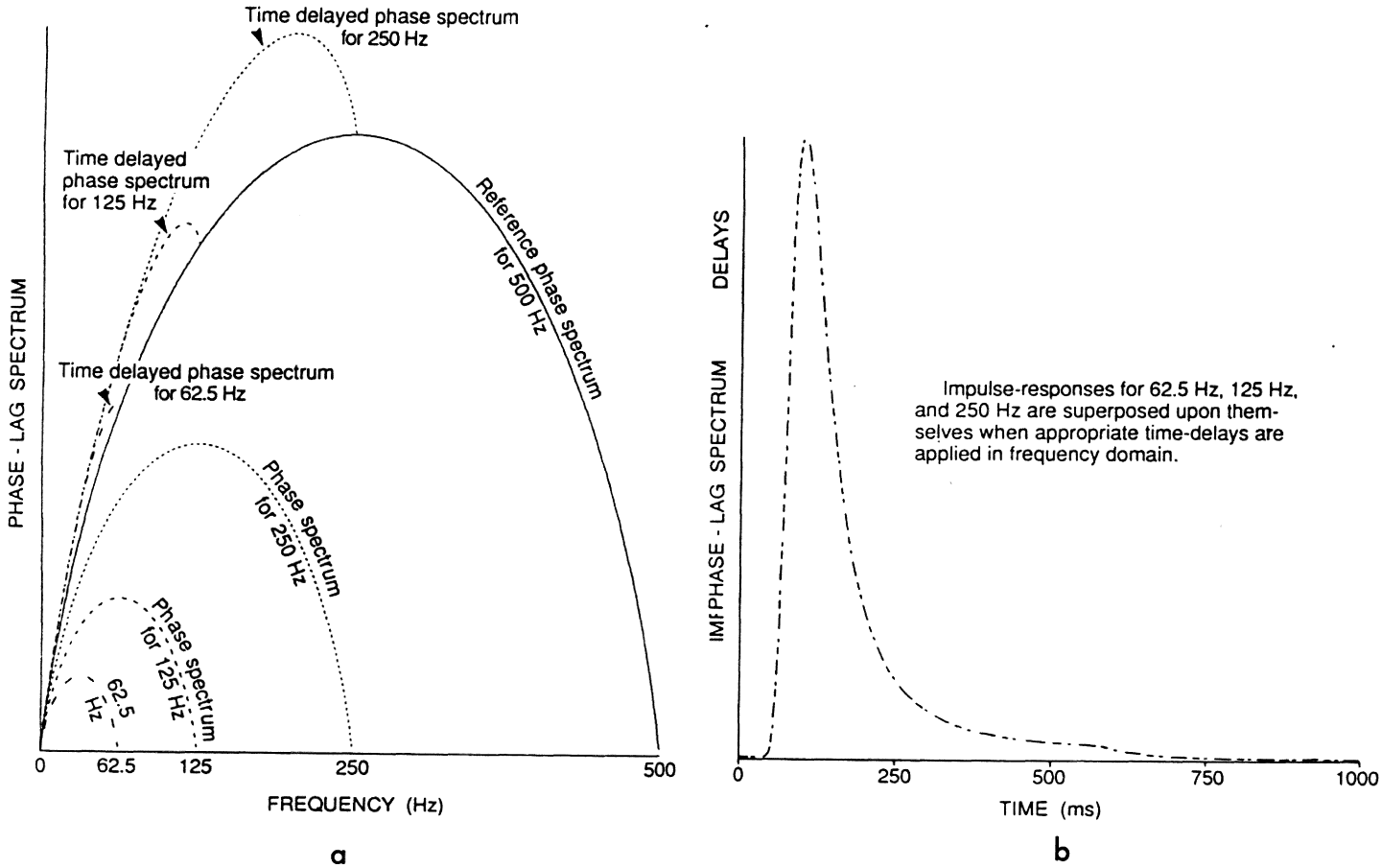

Figure 9. Effect of different Nyquist frequencies (Power = 1.0, with time-delays): Left side is the dispersive phase spectra and the time-delayed results related to each cut-off frequency. Right side is the corresponding impulse-responses. Note that with appropriate time-delays, all of them superimpose upon each other. Since a pure time-delay does not distort the pulse shape, as long as there is no serious aliasing in frequency domain, then identical absorption information may be retrieved from each of the impulse-responses corresponding to different Nyquist frequencies.

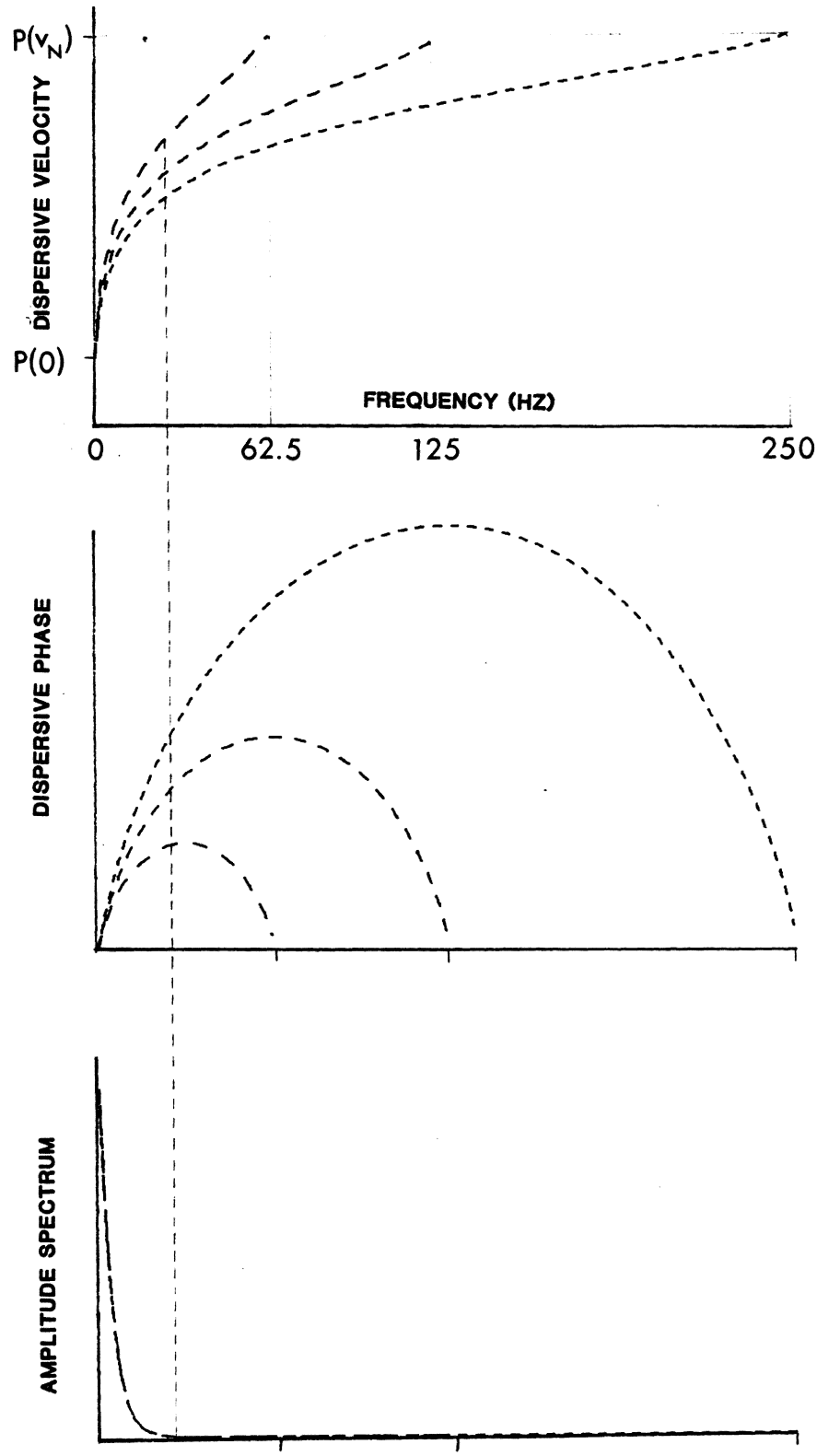

Figure 10. Time delay effect of Nyquist frequency: (a) The dispersive velocity, (b) The dispersive phase, (c) The amplitude spectrum of the impulse-response.

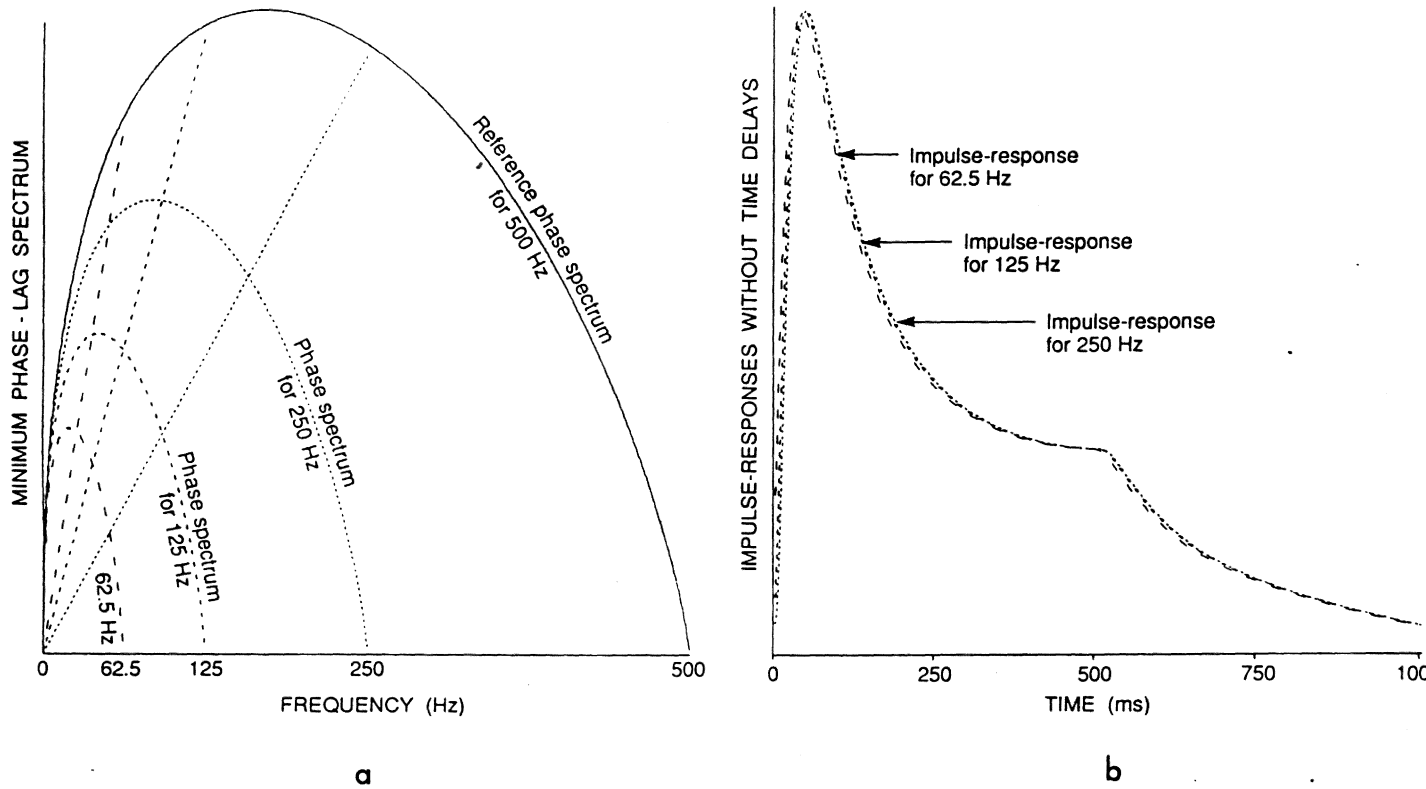

Figure 11. Effect of different Nyquist frequencies. (Power = 0.5, without time-delays): Same description as in Figure 8.

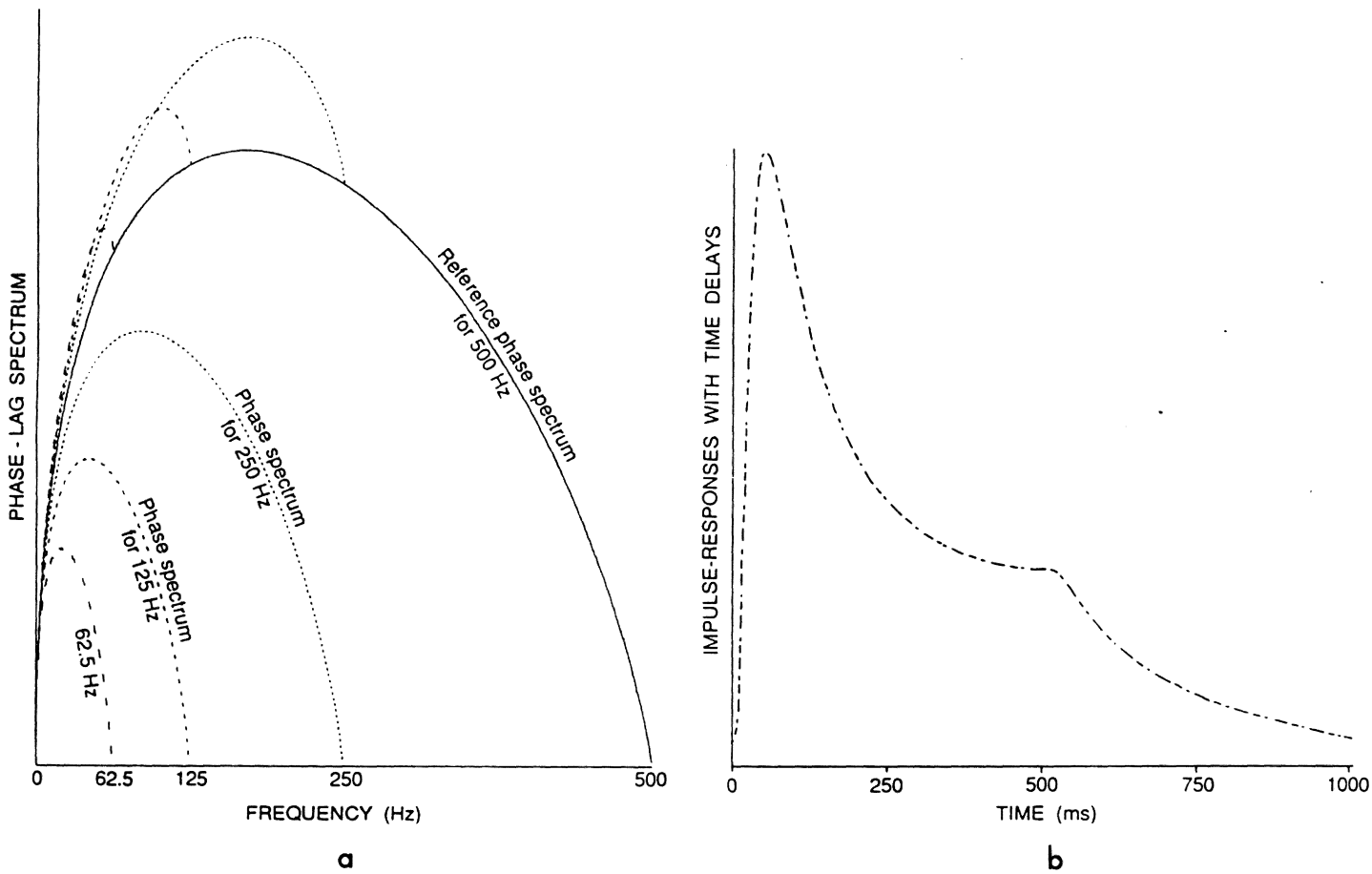

Figure 12. Effect of different Nyquist frequencies. (Power = 0.5, with time-delays): Same description as in Figure 9.

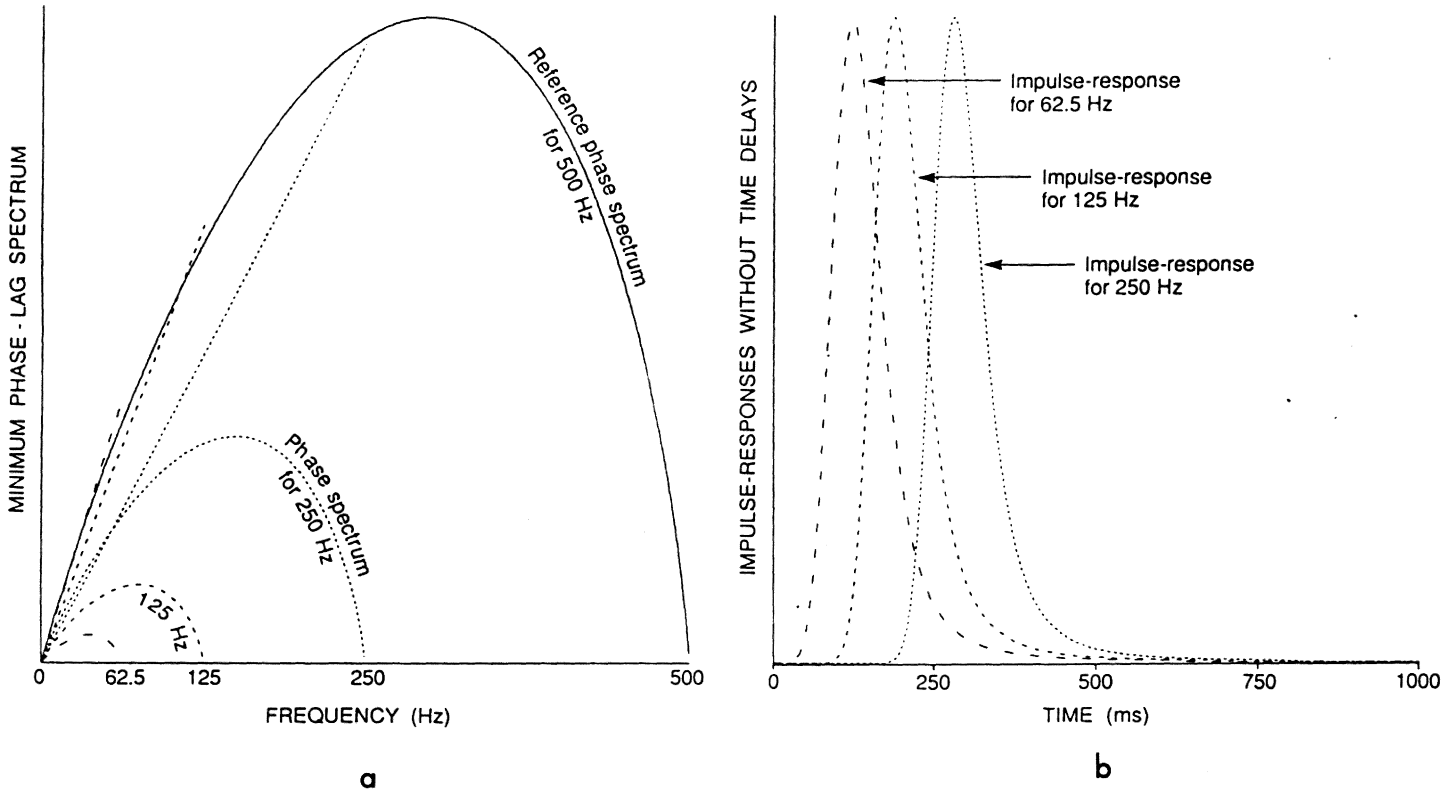

Figure 13. Effect of different Nyquist frequencies. (Power = 1.5, without time-delays): Same description as in Figure 8.

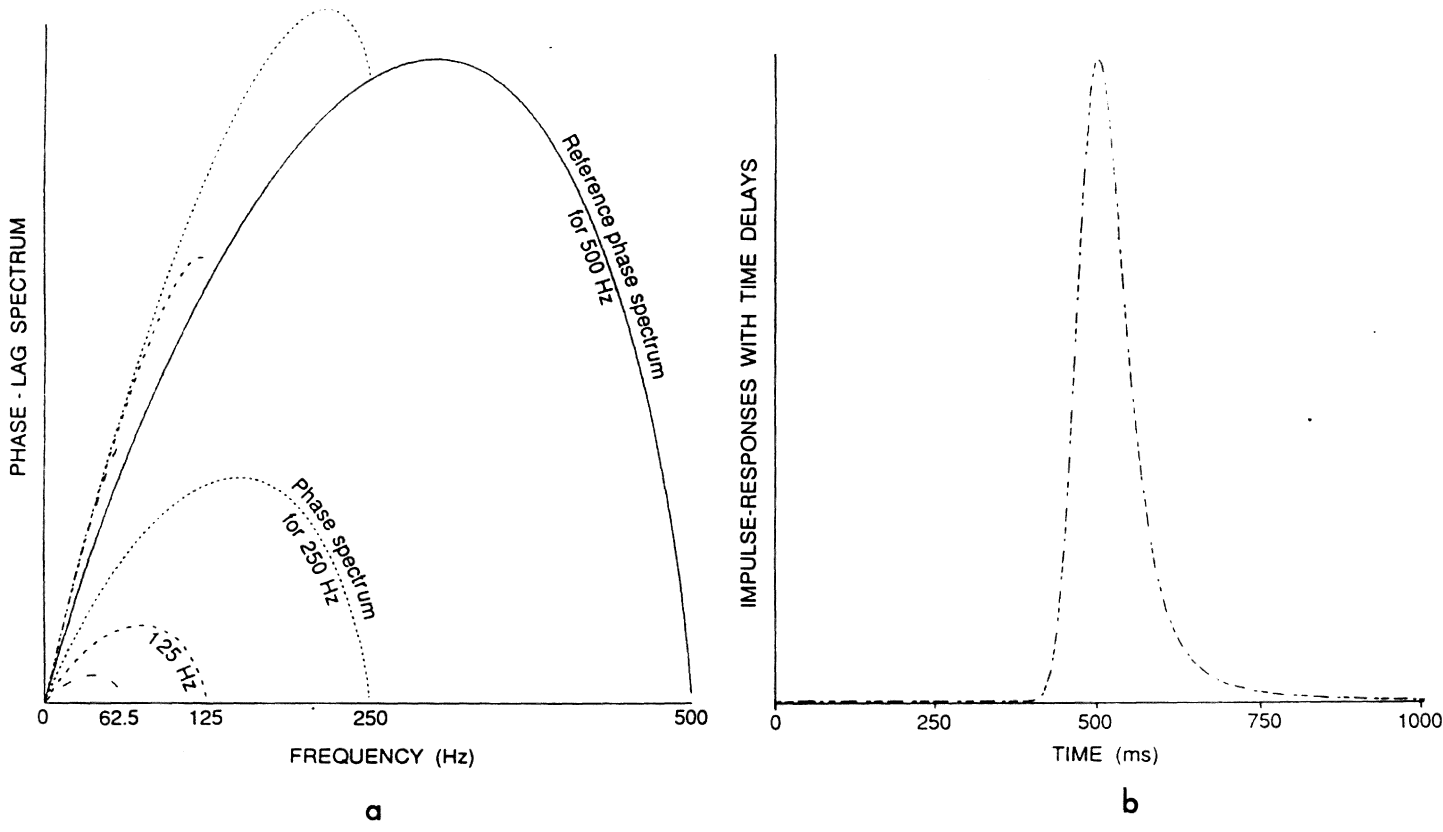

Figure 14. **Effect of different Nyquist frequencies. (Power = 1.5, with time-delays):** Same description as in Figure 9.

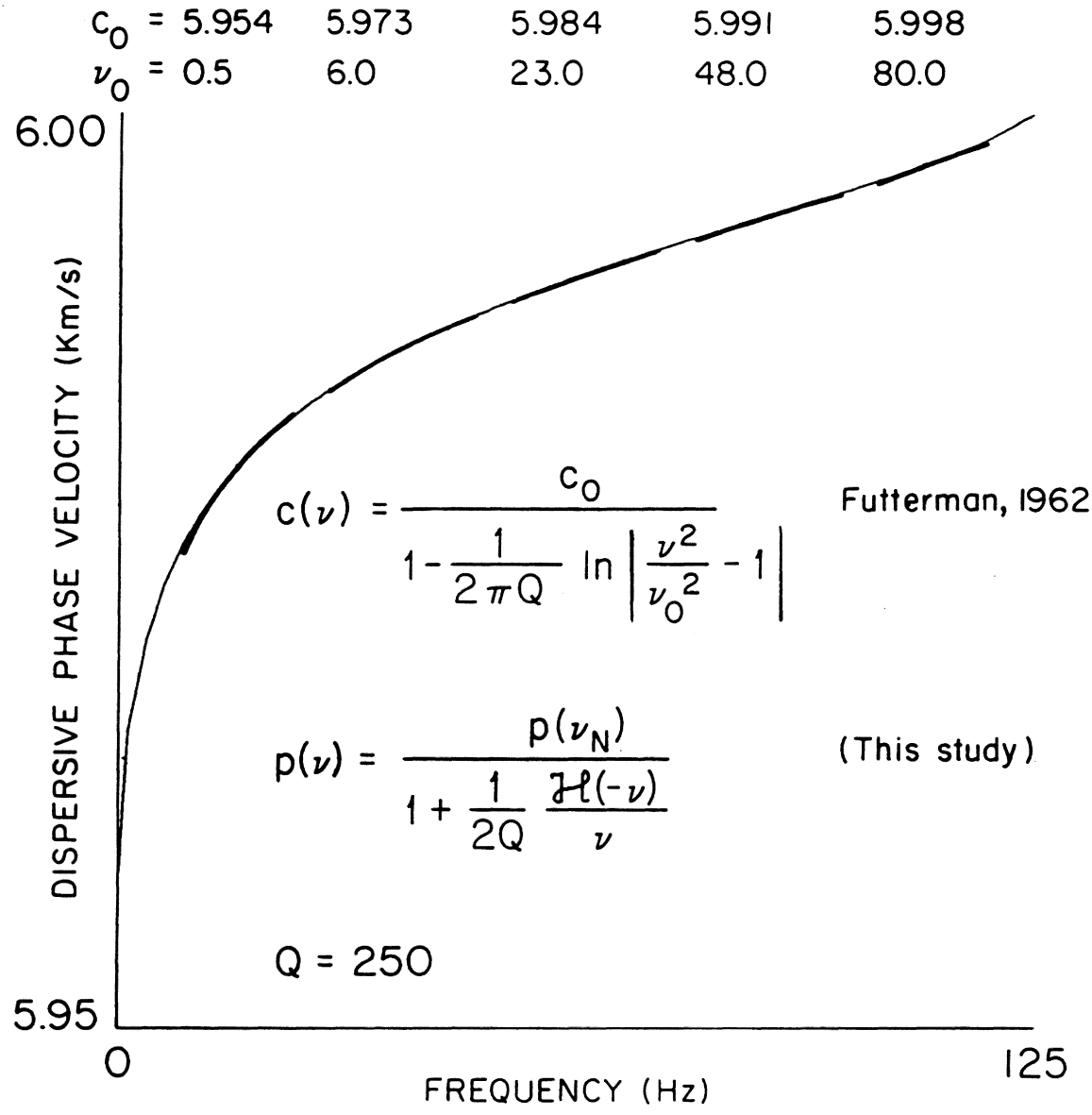

Figure 15. Comparison with Futterman's velocity dispersion relation: Segments of Futterman's velocity dispersion curves are superposed upon our curve. Each c_0 (km/s) and ν_0 (Hz) pair in Futterman's relation is shown at the top of the corresponding segment.

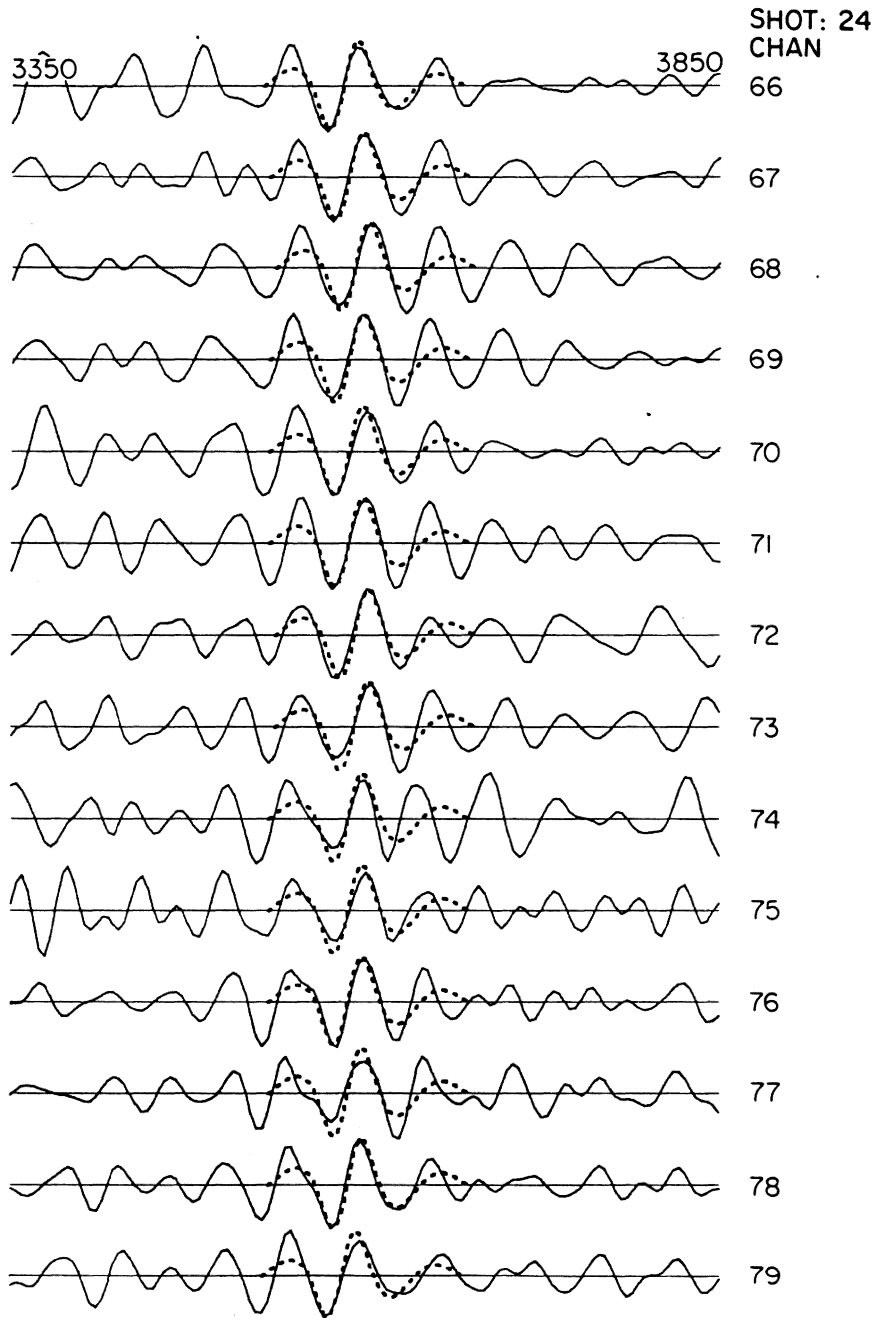

Figure 16. Matching the synthetics with the real data: Real ADCOH data traces from the fifth reflector (at about 9 km depth) are compared with synthetic data (heavy line) generated using the SVD cumulative average solution Q = 135, V = 5.225 km/s, a = 18.578 km for the fifth reflector. See Table 4. A later determination of Q using equation (28) together with a resampling interval of 1 ms instead of 4 ms yielded a value of Q = 95 instead of 135 (see Table 2). The lower value of 95 would be in the right direction for a better match for the wavelet at the bottom of this figure, for example (channel 79). At the top is the 500 ms input Klauder wavelet (dt = 4 ms). No processing except for crosscorrelation has been applied to the real data in order to preserve waveform shape and amplitude. Observe the asymmetry in the synthetic and reflected wavelets, as predicted by causal absorption. Note agreement between synthetic and real data over most of the synthetic wavelet; lack of agreement near ends of wavelet attributed to interference from neighboring wavelets.

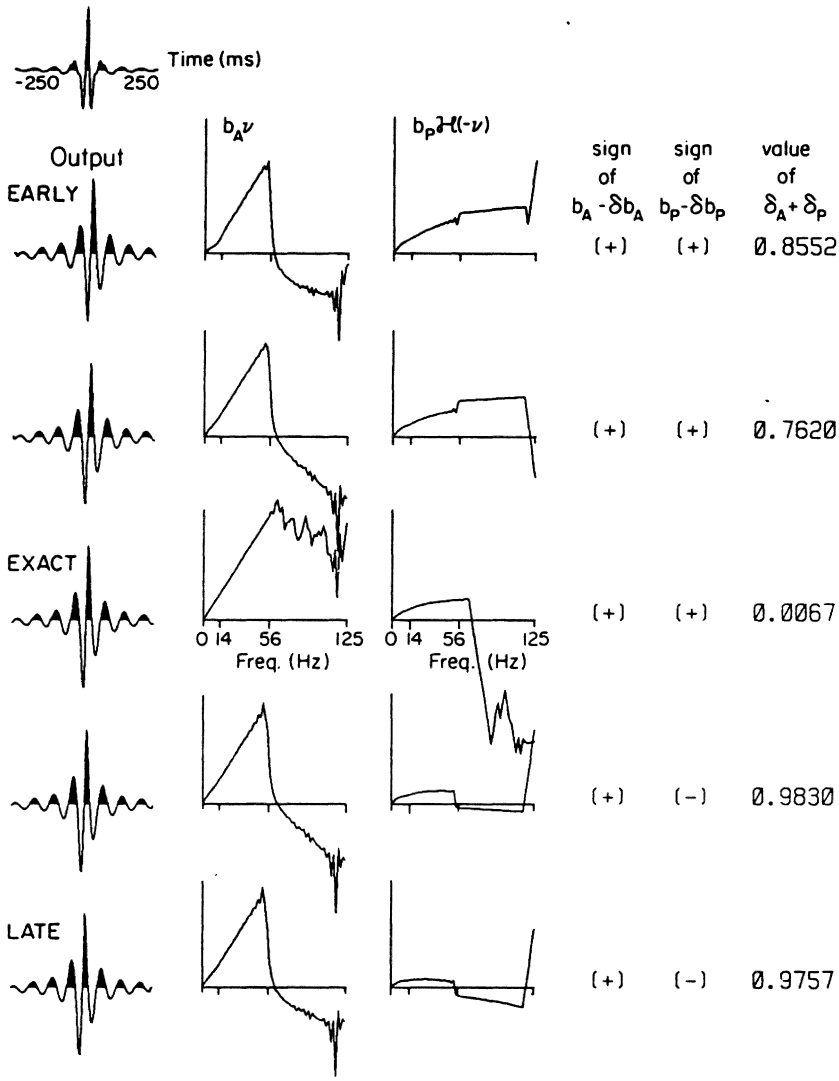

Figure 17. The dynamic analysis window: Five different positions of the analysis window for both phase and amplitude rejection criteria. Synthetic data. Input wavelet on top of left column is a 500 ms input Klauder wavelet (Δt = 4 ms) which is subjected to causal absorption of Q = 100, V = 3 km/s, a = 10 km. Absorbed wavelet below as it appears in the analysis window. Center column is plot of − ln [output/input] versus v (Equation (20, 21). Absorption coefficient as well as dispersive phase are valid only over the interval 14-56 Hz. Outside of this effective frequency band the information in absorption coefficient and dispersive phase is useless. First two rows are the early positions; third row is the correct (exact) position; last two rows are late positions. Third column (dispersive phase) is plot of the right-hand side of equation (39) versus v. Least error occurs when window is correctly centered. Second and third columns are not Hilbert transform pairs; they are from independent computations.

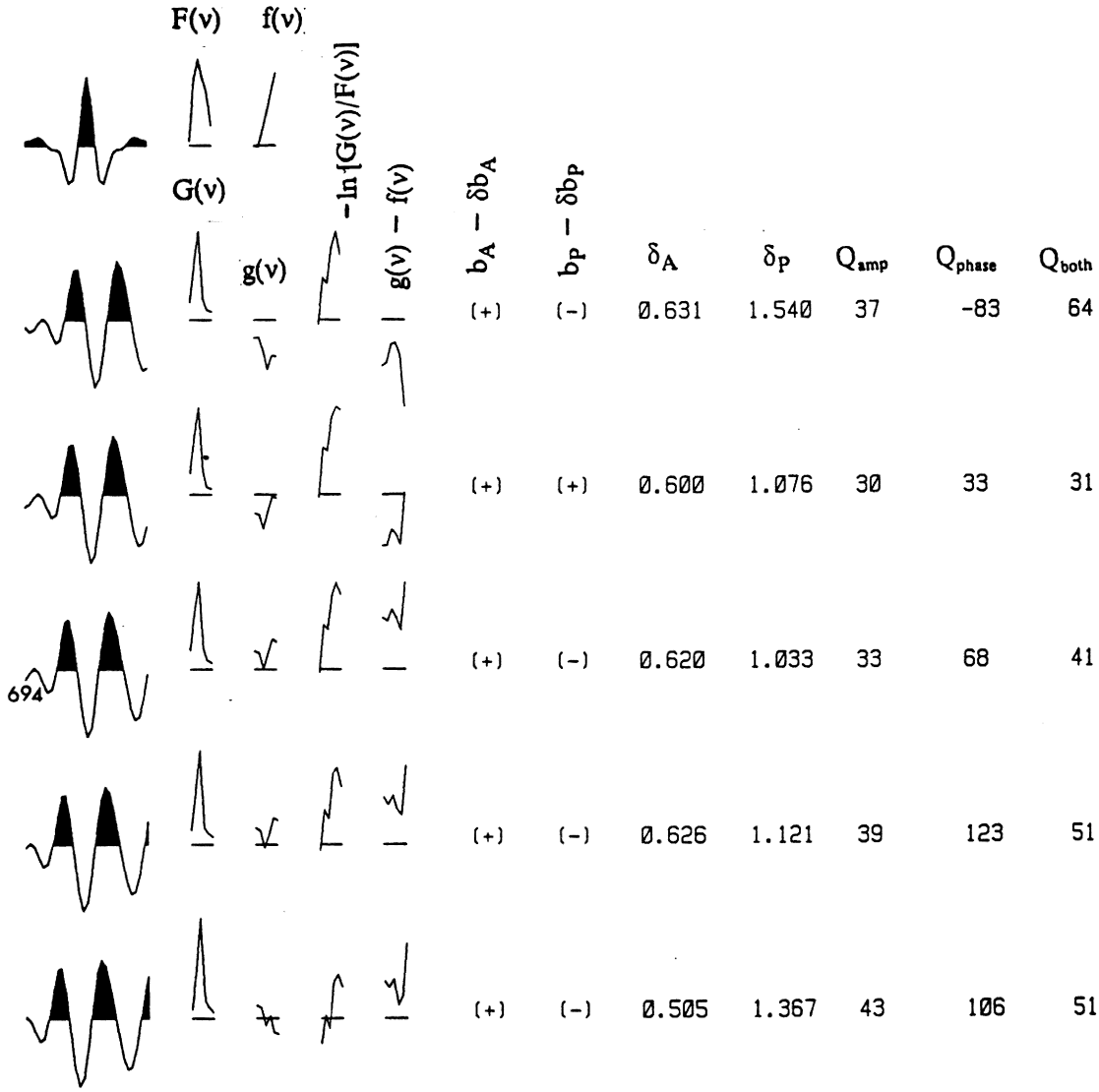

Figure 18. Performance of dynamic window: Reflector 1: Single-trace analysis. First row is the input Klauder wavelet. Columns from left to right represent: (1) The wavelet in the dynamic window, (2) The amplitude spectrum (14-56 Hz), (3) The phase spectrum (14-56 Hz), (4) negative of the natural logarithm of the amplitude spectrum ratio (14-56 Hz), (5) Phase spectrum difference, (6) Sign of $b_A - \delta b_A$, (7) Sign of $b_P - \delta b_P$, (8) Value of δ_A, (9) Value of δ_P, (10) Estimated Q value from amplitude ratio, (11) Estimated Q value from phase, and (12) Estimated Q value from both amplitude and phase calculated from equation 54. The window length is 112 ms. Data are sampled at 4 ms. The selection that would be made by the dynamic analysis window would be the third row (0.6 + 1.076) in the figure. Using both amplitude and phase information, Q = 31 compared with Q_{time} = 31 from Table 2. Differences between single-trace determinations of Q using amplitude versus phase are attributed to the much more sensitive nature of the phase technique compared with the relatively insensitive nature of the window position for the amplitude technique determination of Q.

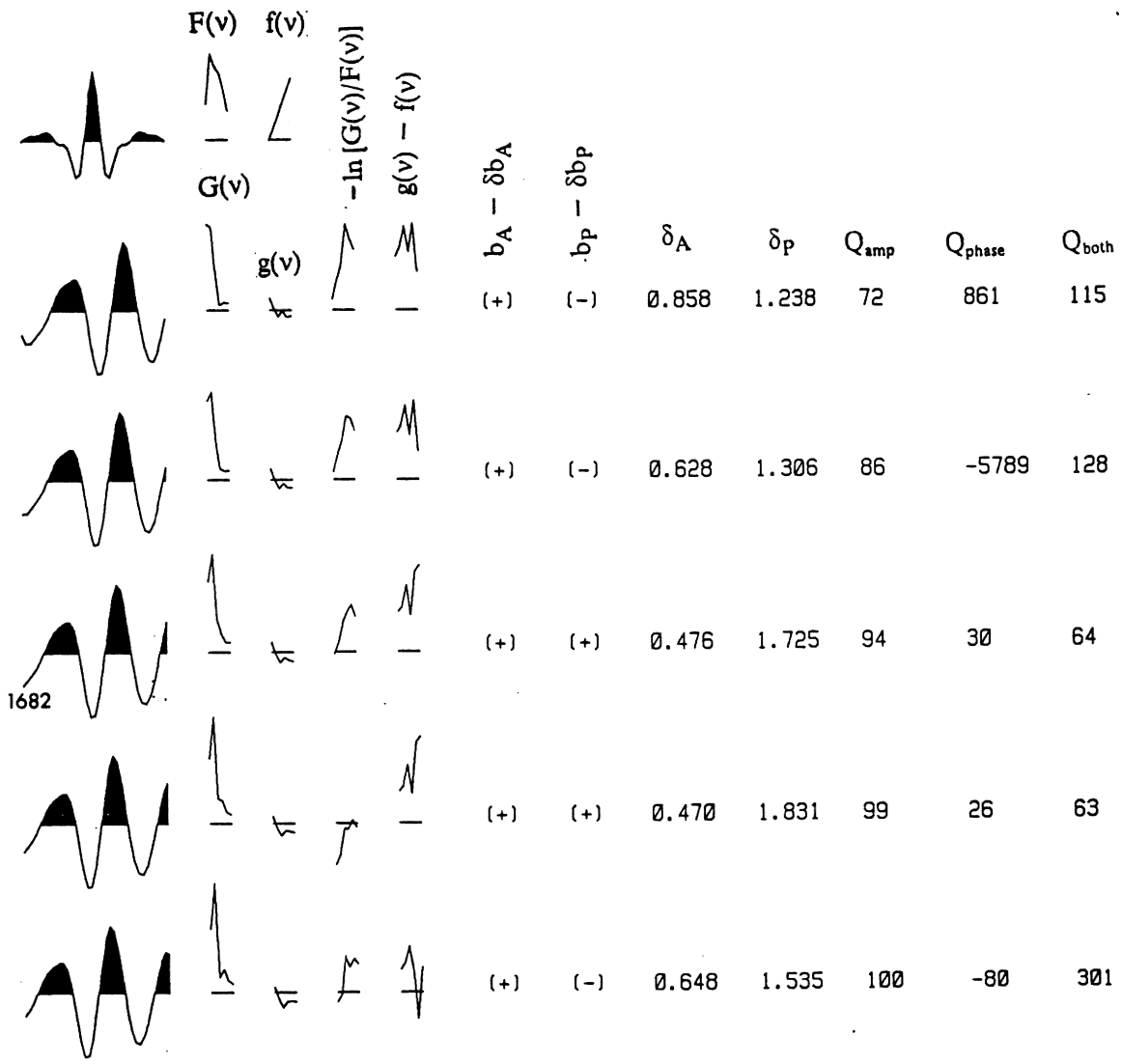

Figure 19. Performance of dynamic window: Reflector 2: Description is the same as in Figure 18. The window length is 136 ms. Data are sampled at 4 ms. The selection that would be made by the dynamic analysis window would be the fourth row (1.725 + 0.476) in the figure. Using both amplitude and phase information, Q = 64 compared with Q_{time} = 56 from Table 2.

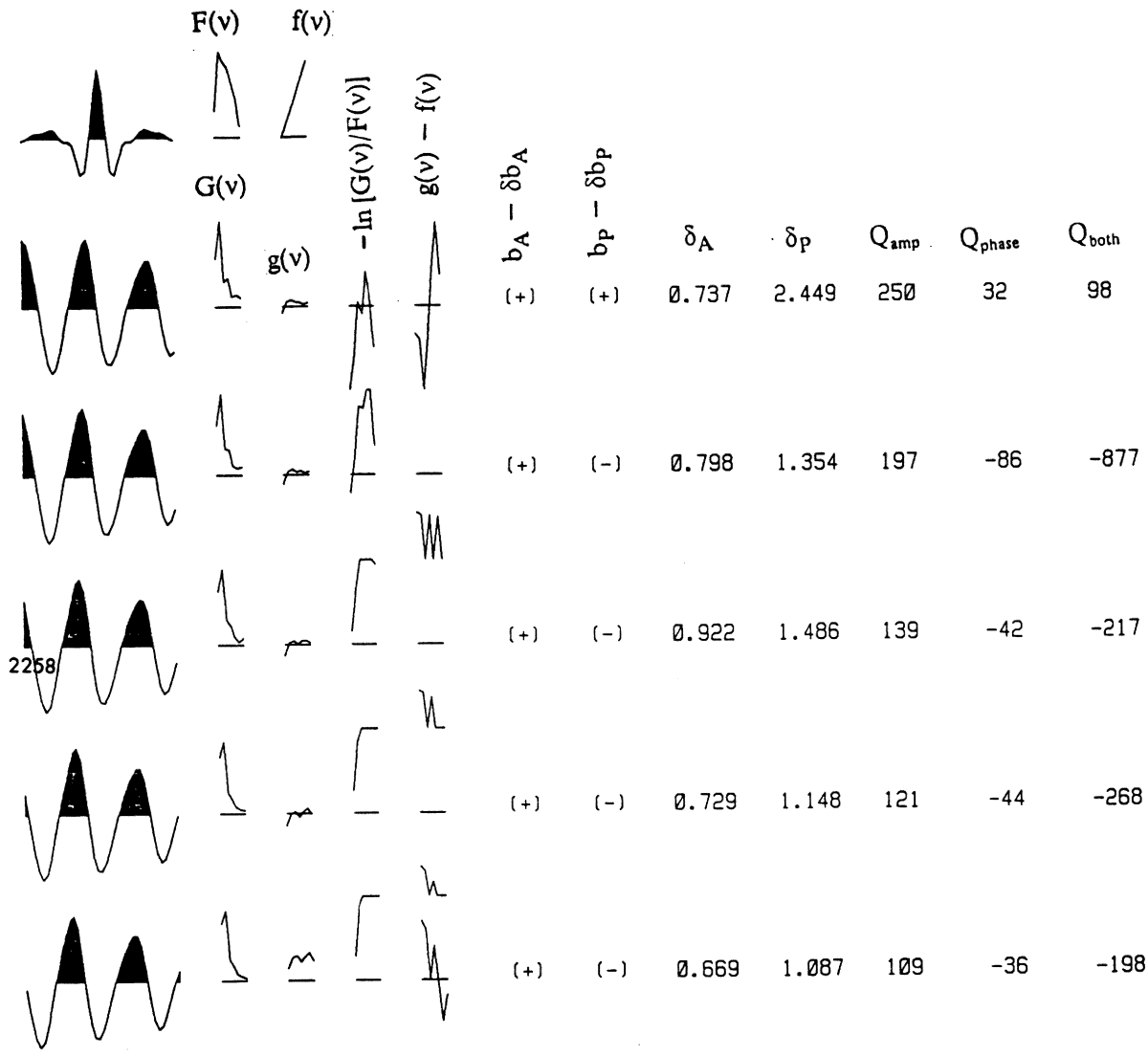

Figure 20. Performance of dynamic window: Reflector 3: Description is the same as in Figure 18. The window length is 144 ms. Data are sampled at 4 ms. The selection that would be made by the dynamic analysis window would be the second row (0.737 + 2.449) in the figure. Using both amplitude and phase information, Q = 98 compared with $Q_{time} = 68$ from Table 2.

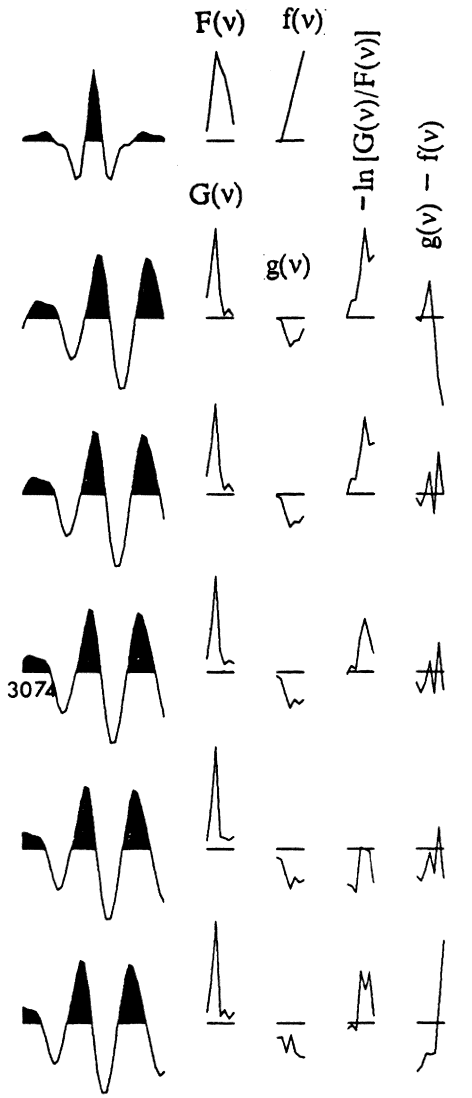

$b_A - \delta b_A$	$b_P - \delta b_P$	δ_A	δ_P	Q_{amp}	Q_{phase}	Q_{both}
(+)	(-)	0.812	2.030	148	-96	538
(+)	(-)	0.729	1.046	172	275	203
(+)	(-)	0.746	0.979	281	380	316
(+)	(+)	0.844	0.952	402	254	316
(+)	(+)	1.053	1.856	261	65	124

Figure 21. Performance of dynamic window: Reflector 4: Description is the same as in Figure 18. The window length is 124 ms. Data are sampled at 4 ms. The selection that would be made by the dynamic analysis window would be the fifth row (0.844 + 0.952) in the figure. Using both amplitude and phase information, Q = 316 compared with $Q_{time} = 88$ from Table 2.

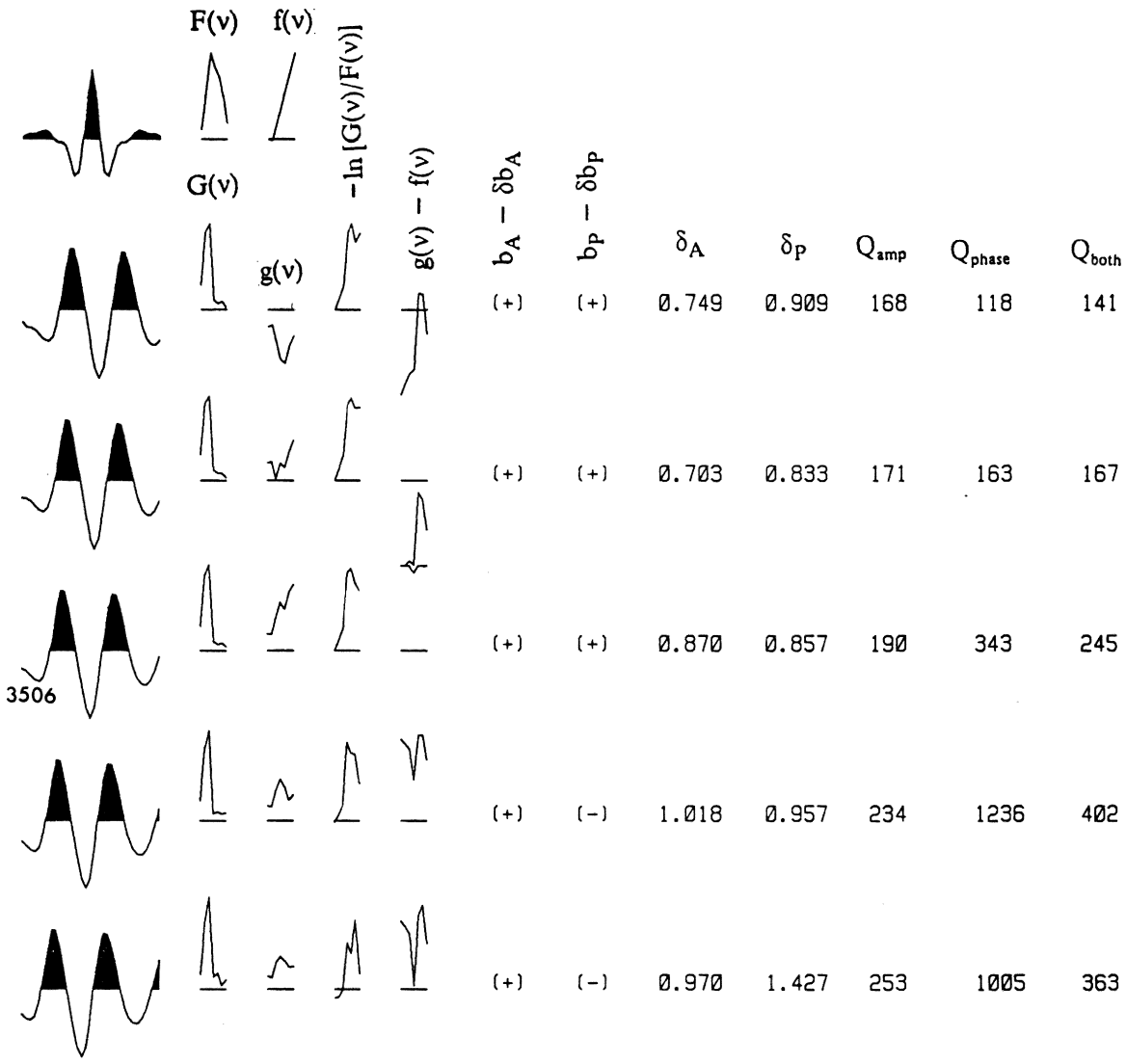

$b_A - \delta b_A$	$b_P - \delta b_P$	δ_A	δ_P	Q_{amp}	Q_{phase}	Q_{both}
(+)	(+)	0.749	0.909	168	118	141
(+)	(+)	0.703	0.833	171	163	167
(+)	(+)	0.870	0.857	190	343	245
(+)	(-)	1.018	0.957	234	1236	402
(+)	(-)	0.970	1.427	253	1005	363

Figure 22. Performance of dynamic window: Reflector 5: Description is the same as in Figure 18. The window length is 128 ms. Data are sampled at 4 ms. The selection that would be made by the dynamic analysis window would be the third row (0.703 + 0.833) in the figure. Using both amplitude and phase information, Q = 167 compared with Q_{time} = 95 from Table 2.

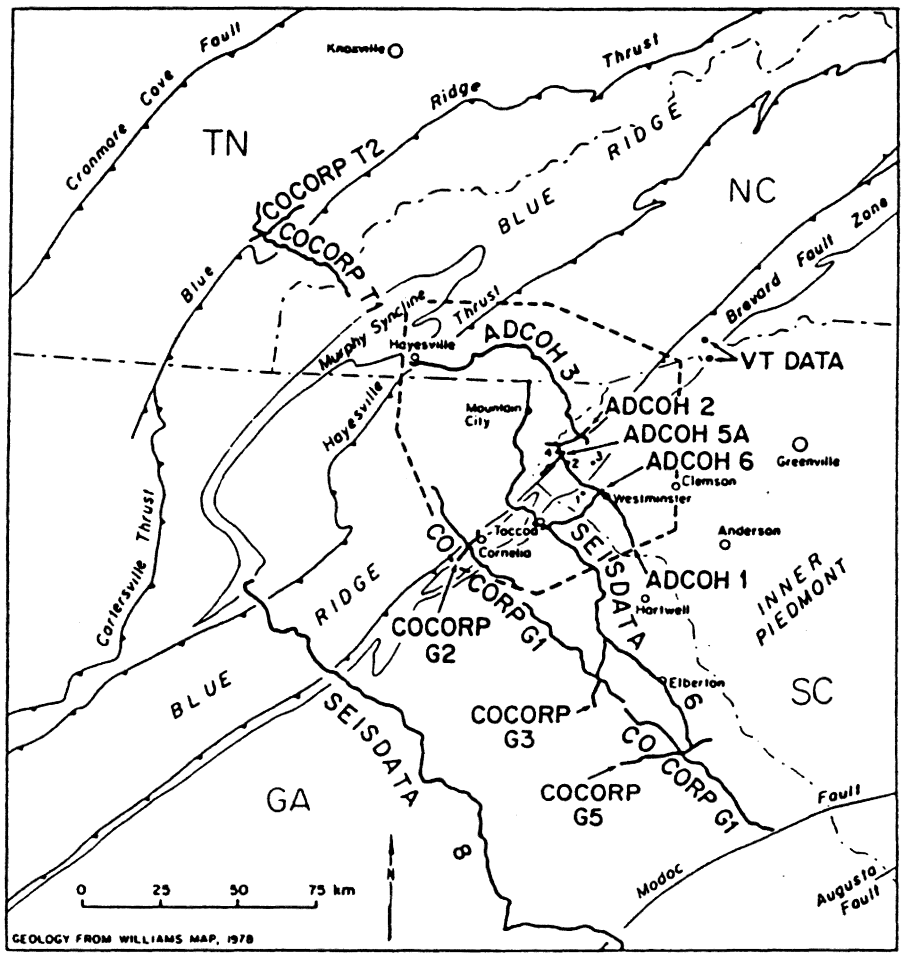

Figure 23. Location map of ADCOH regional vibroseis lines: Locations of SEISDATA data and COCORP lines in site study area, and the shallow core holes drilled as part of this program are also shown.

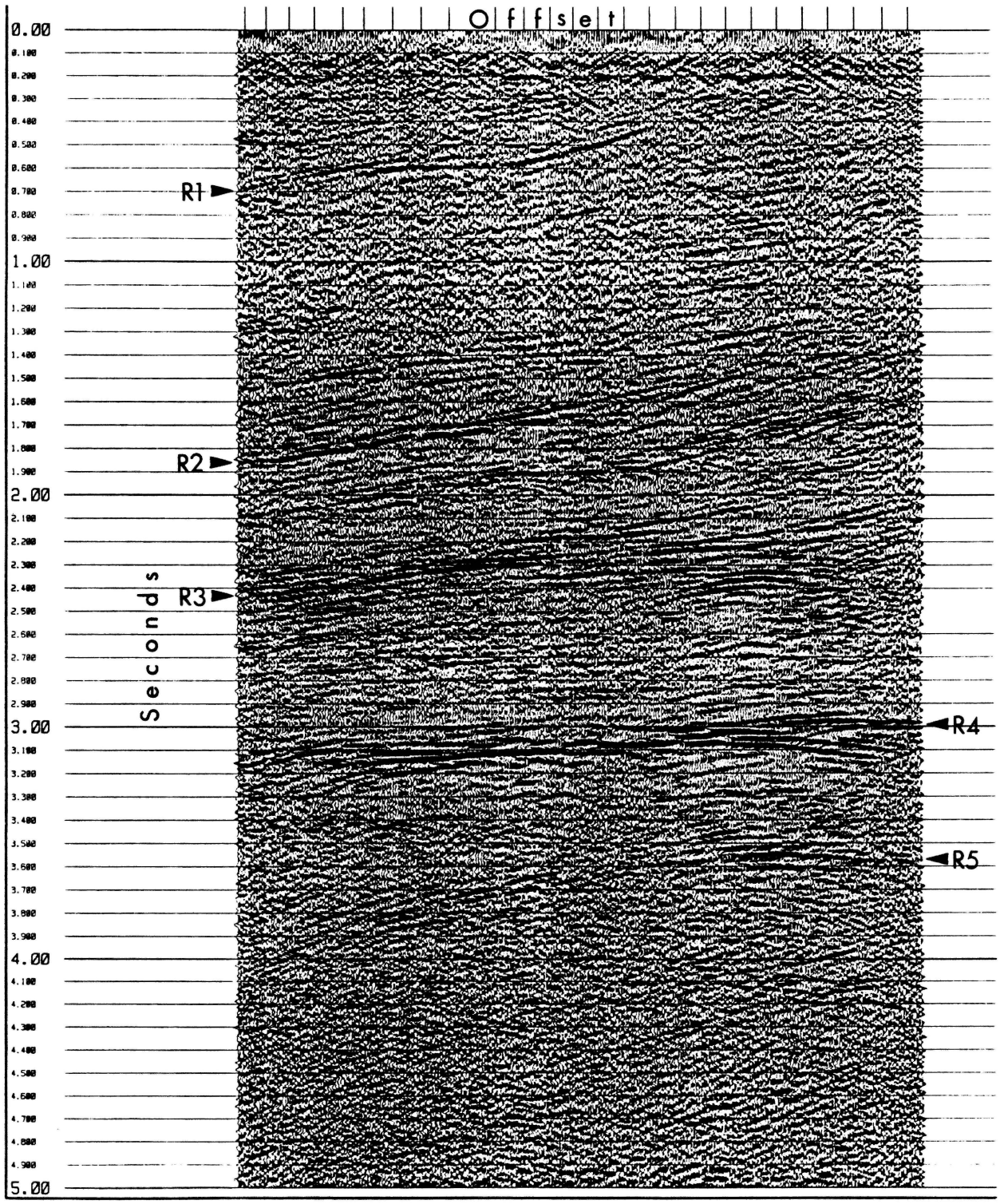

Figure 24. **ADCOH regional Line 1:** Unmigrated conventional stack. For processing parameters and interpretation of the data, see Çoruh and others (1987).

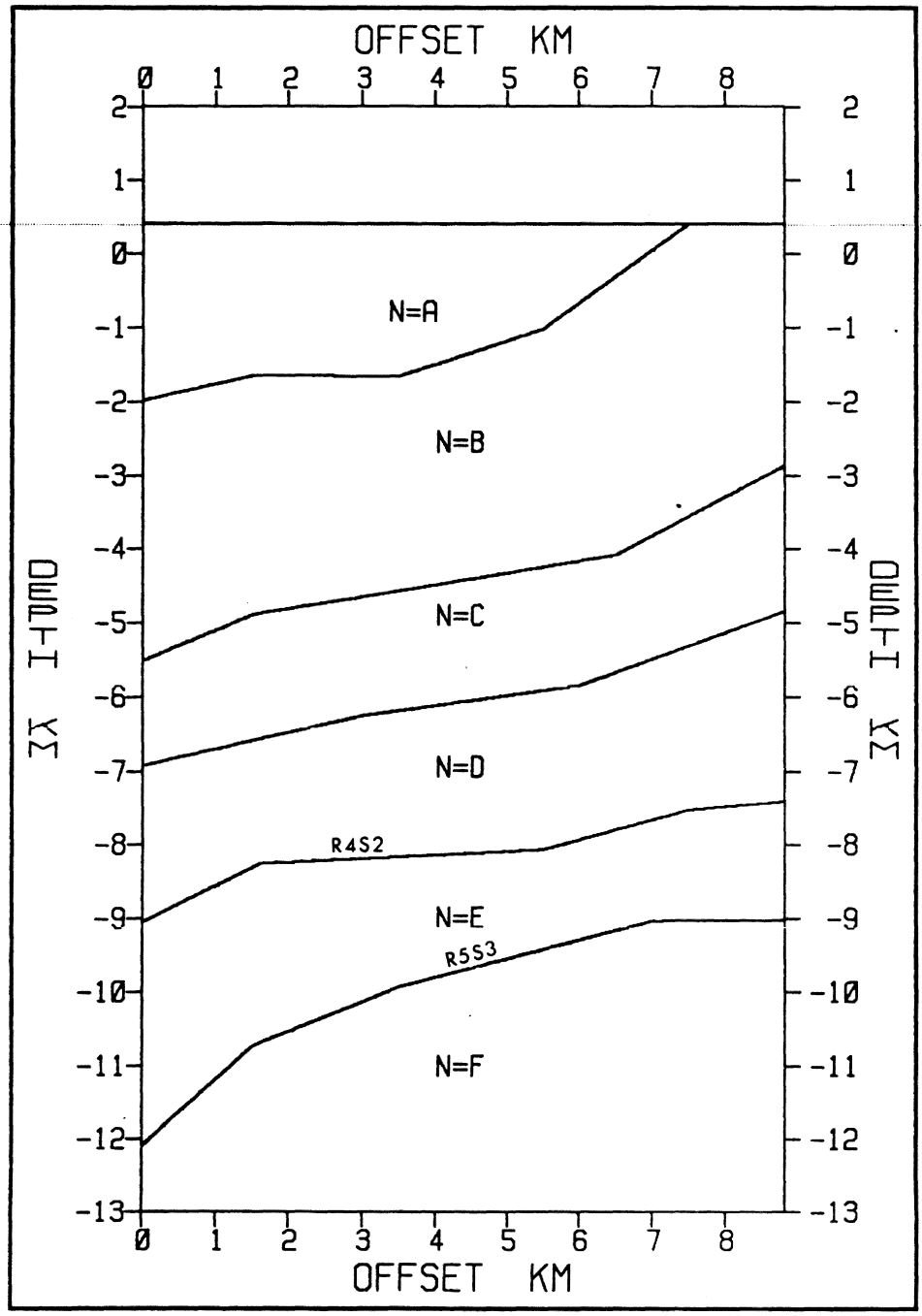

Figure 25. Model based on the stacked data: Compare with Figure 24.

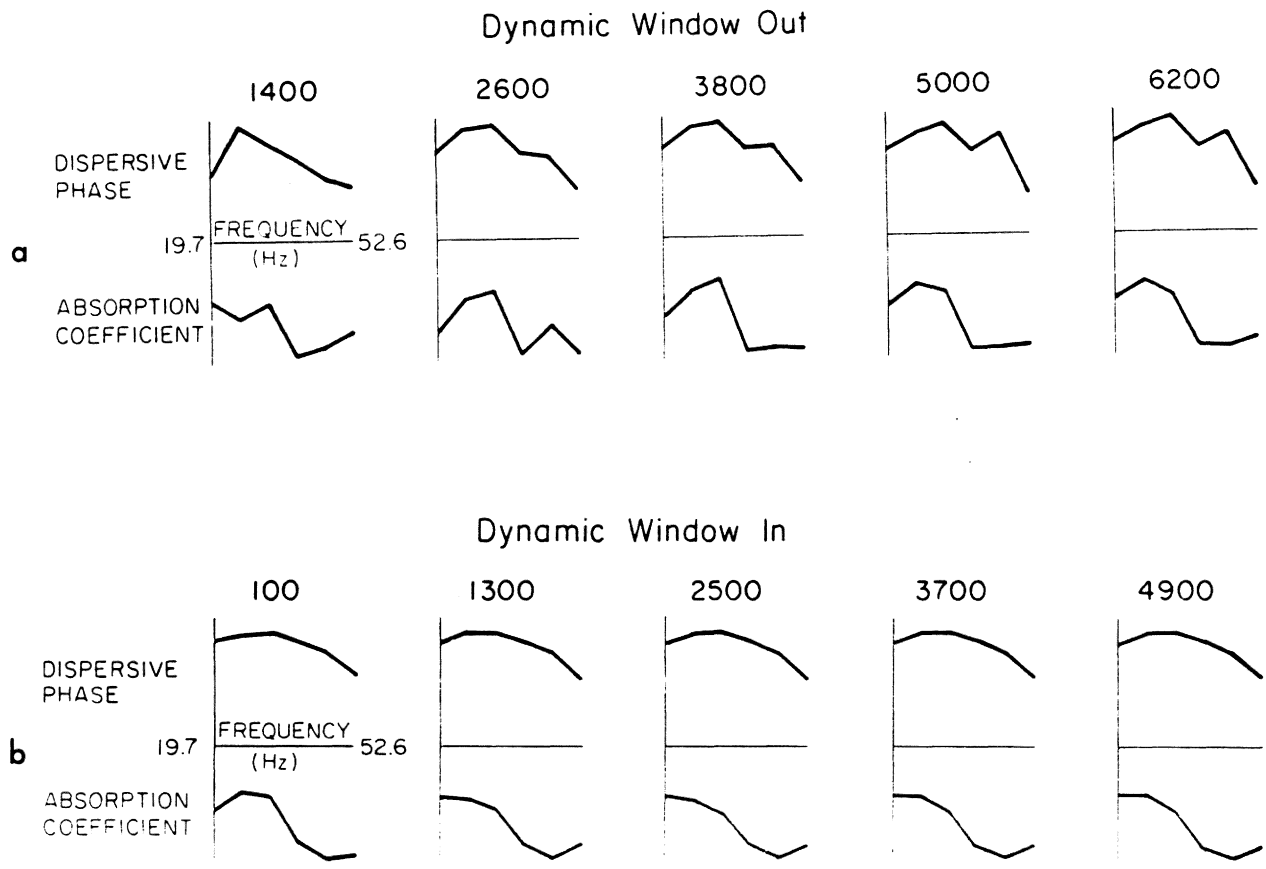

Figure 26. Performance of dynamic analysis window with real data: (a) Dynamic window out, (b) Dynamic window in. The number associated with each curve-pair indicates number of participant traces.

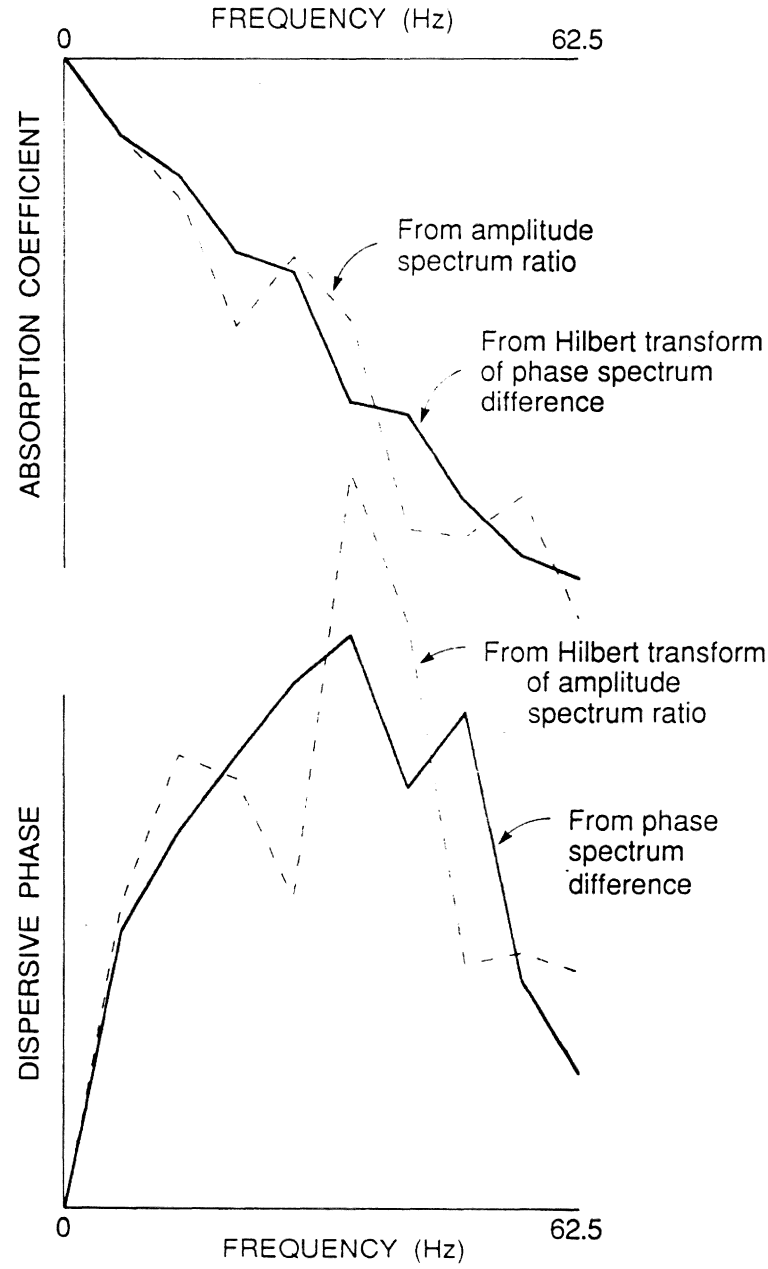

Figure 27. Causal absorption relations from real data: Solid line at the bottom is the dispersive phase, B(v), obtained from the data without using any of the analysis window constraints, i.e., the wavelets picked up with approximate travel-times are directly used in computations. If absorption were strictly linear with frequency, if the analysis window were perfectly centered over the attenuated wavelet, and if the data were completely noise-free, then B(v) would be defined by equation (12). This phase method of determining body wave dispersion is the new technique described herein. Solid line at the top is the discrete Hilbert transform of this phase curve. Dashed line at the top is the absorption coefficient obtained from the data again without using any of the analysis window constraints. This dashed line is the conventional method of determining $\alpha(v)$ versus v. Note the slightly more linear $\alpha(v)$ versus v for the phase method suggesting that the phase domain is the better method. Dashed line at the bottom is the discrete Hilbert transform of this dashed absorption curve. These curves are the result of averaging B(v) for about 12,400 seismic traces.

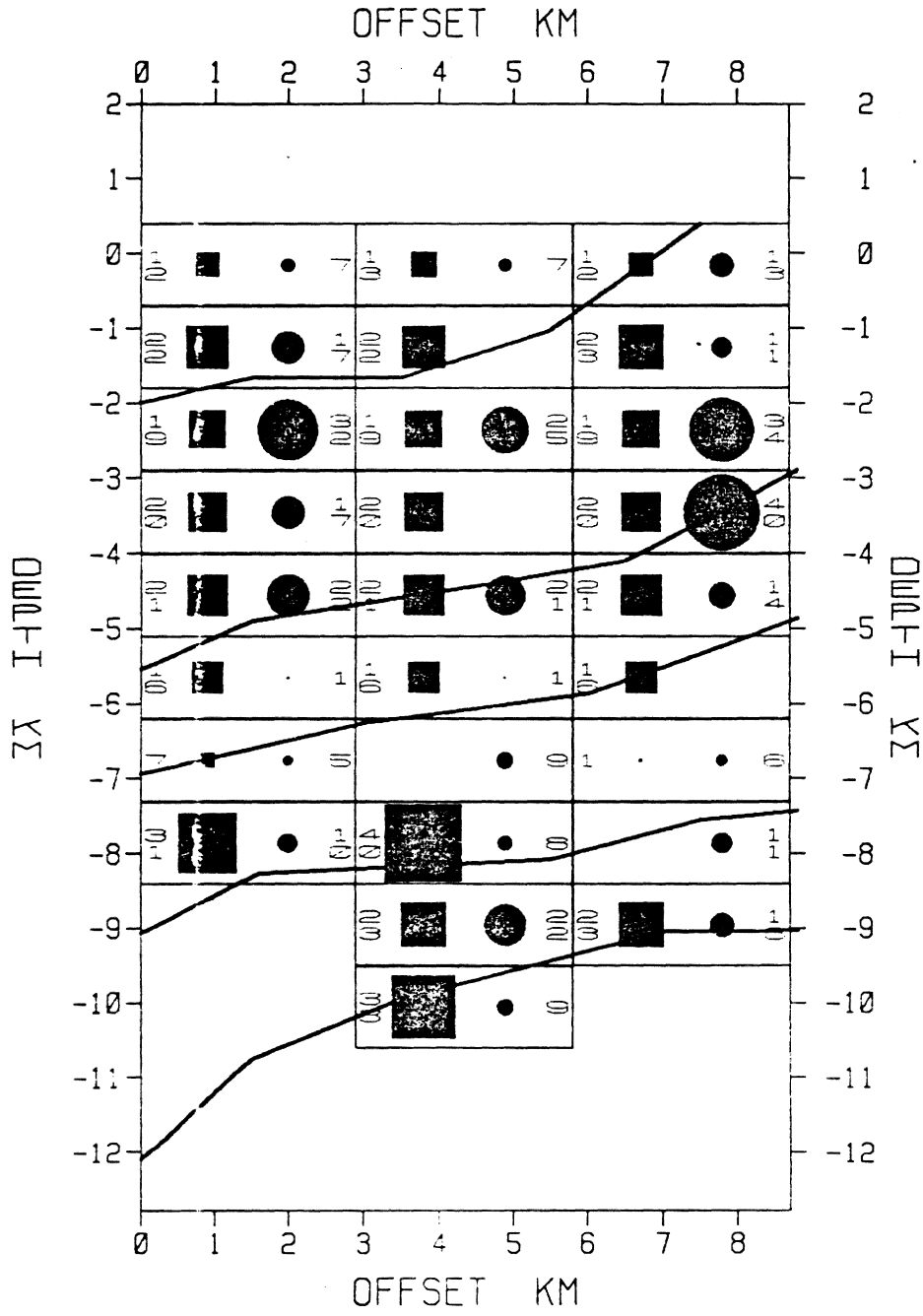

Figure 28. Tomographic SVD solutions for R5S3: "Tomographic" solutions, unlike "average" solutions show only relative values. Solutions obtained from SVD techniques using rectangular motifs. Both amplitude and phase information used. Relative sizes of squares denote relative magnitudes of velocity; relative sizes of circles denote relative magnitudes of Q. Note low-velocity zone at about 5-7 km believed to be caused by parautochthonous shelf strata beneath allochthonous crystalline plate.

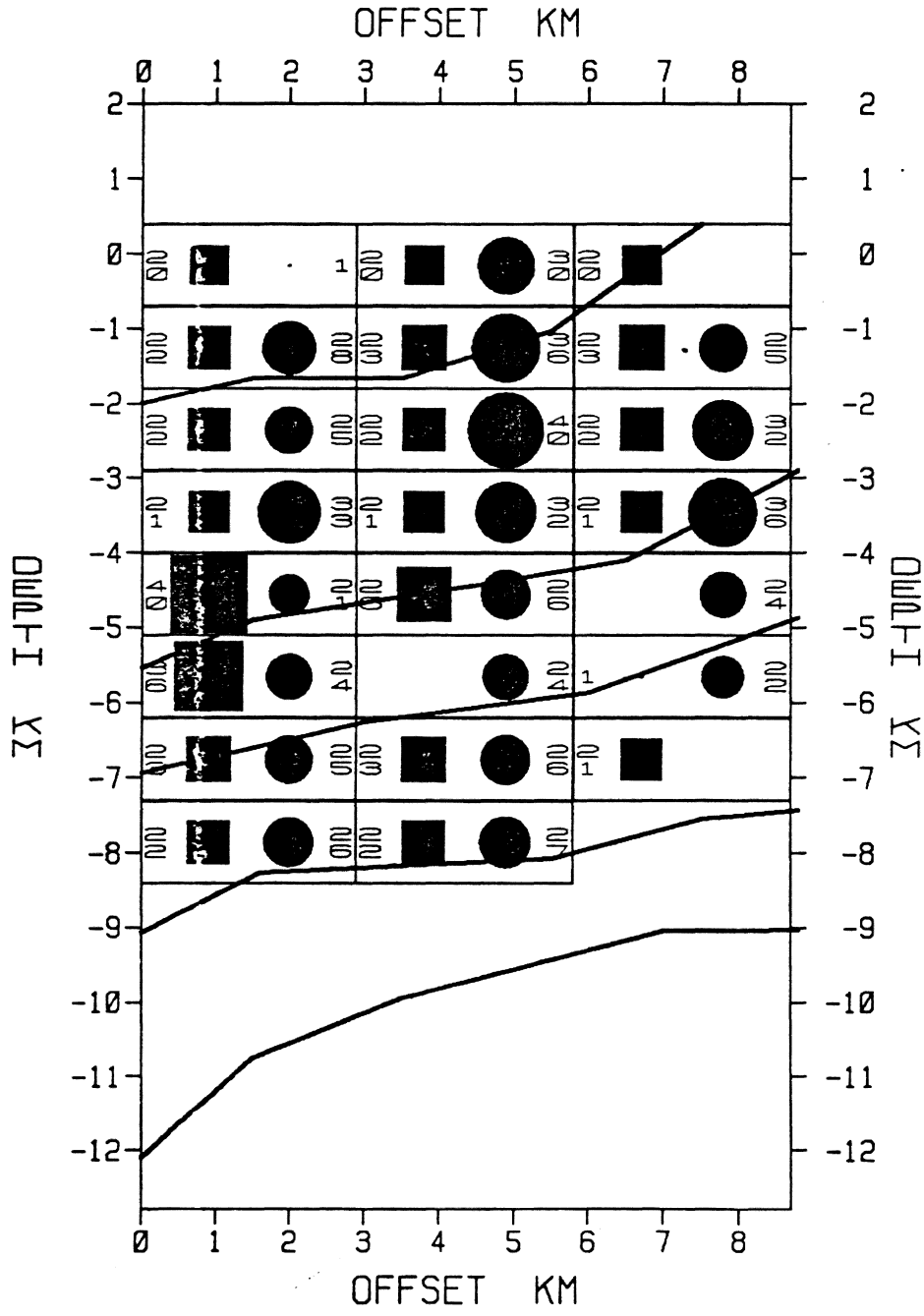

Figure 29. Reflector 4 segment 2 using both amplitude and phase: Tomographic solutions obtained from SVD techniques using rectangular motifs. Size of square is proportional to magnitude of velocity solution from SVD; size of circle is proportional to magnitude of Q.

APPENDIX 1 - BRUNE'S PULSE

Brune's pulse (Brune, 1968) is minimum-delay and defined by:

$$F_b(\omega) = \frac{1}{(1 + i\omega)^2} \tag{1}$$

The poles of (1), a double-pole of the form $\omega = -i$, are in the lower-half of the complex plane, therefore guaranteeing the minimum-phase property. The amplitude $A_b(\omega)$ and phase $B_b(\omega)$ spectra are given by:

$$A_b(\omega) = \frac{1}{1 + \omega^2} \quad , \quad B_b(\omega) = \tan^{-1}\frac{-2\omega}{1 - \omega^2} \tag{2}$$

Relations in (2) constitute Hilbert transform pairs; i.e., one can obtain $B_b(\omega)$, for example, by substituting the logarithm of $A_b(\omega)$ in equation (1). $A_b(\omega)$ and $B_b(\omega)$ are shown in Figure 30 on page 123.

First, we compute the time-domain Brune pulse, $f_b(t)$, from:

$$f_b(t) = \frac{1}{2\pi}\int_{-\omega_N}^{+\omega_N} A_b(\omega)e^{iB_b(\omega)}e^{+i\omega t}d\omega$$

where ω_N is some Nyquist cut-off frequency. $f_b(t)$ is shown in Figure 30c. An analysis of the roots of the polynomial reveals that one of the roots, which is real and negative in this case, lies inside the unit circle. Therefore, once the equations in (2) are truncated at some Nyquist frequency ω_N, the corresponding time-domain pulse loses its minimum-delay property. The

relations in (2) which guarantee the minimum-delay property of Brune's pulse as far as a continuous process is concerned, fail to do so when they are discretized. Hence, when we truncate and approximate the continuous Brune's pulse (which is defined for all of positive time) by discretizing it into some finite number of samples, it is no longer minimum-delay.

Second, we will compute the time domain Brune's pulse $f'_b(t)$ from

$$f'_b(t) = \frac{1}{2\pi} \int_{-\omega_N}^{+\omega_N} A_b(\omega) e^{iB'_b(\omega)} e^{+i\omega t} d\omega$$

where

$$B'_b(\omega) = H[\ln A_b(\omega)]$$

H stands for discrete Hilbert transformation. $f'_b(t)$ is shown in Figure 30a.

For this case, computation of the roots shows that they all lie outside of the unit circle; the function is therefore minimum-delay.

Third, we compute the time domain Brune pulse $f''_b(t)$

$$f''_b(t) = \frac{1}{2\pi} \int_{-\omega_N}^{+\omega_N} A_b(\omega) e^{iB''_b\omega} e^{+i\omega t} d\omega$$

where

$$B''_b(\omega) = B_b(\omega) - \omega\tau$$

We have subtracted from the phase spectrum (equation 2) a linear trend of slope τ. The idea is to shift the pulse toward negative time so that the root inside the unit circle is removed. Actually, the advance of the pulse some τ time did move the root out of the unit circle causing a minimum-delay pulse; however, a piece from the front of the pulse appeared at the tail of the pulse; i.e., in negative time. Therefore, although the pulse is now minimum-delay, it is no longer causal.

A similar investigation of the Futterman's pulse is shown in Figure 31. The fundamental difference between Brune's pulse and Futterman's pulse is that the former has a bounded phase spectrum (i.e., the phase curve is bounded by a horizontal asymptote) and the latter has an unbounded phase spectrum (i.e., the phase curve goes to infinity as the frequency increases).

APPENDIX 2 - THE SINGULAR VALUE DECOMPOSITION OF A MATRIX

The most reliable method for computing the coefficients for a general least-squares problem is based on an orthogonal matrix factorization known as Singular Value Decomposition (SVD). This method is efficient in dealing with errors in the data, round-off errors, and linear dependence. It is important to identify rank deficient situations when solving least-squares problems. The only fully reliable way to treat rank deficiency is to compute the SVD.

A SVD of an m-by-n real matrix A is any factorization of the form $A = USV^T$ where U is an m-by-m orthogonal matrix (i.e. $U^TU = I$), V is an n-by-n orthogonal matrix (i.e. $V^TV = I$) and S is an m-by-n diagonal matrix with $s_{ij} = 0$ if $i \neq j$ and $s_{ii} = s_i \geq 0$. The quantities s_i are called the singular values of A, and the columns of U and V are called the left and right singular vectors.

The SVD Algorithm

The objective of the algorithm is to find orthogonal matrices U and V so that $U^TAV = S$ is a diagonal matrix (Golub and Reinsch, 1970). Both U and V are obtained as the product of orthogonal matrices known as Housholder reflections. The matrix A is reduced to upper bidiagonal form. Once the bidiagonalisation of A has been achieved, the next step is an iterative process (Golub and Kahan, 1965) in which the superdiagonal elements are reduced to a negligible size by implicitly applying the symmetric QR algorithm, leaving the desired diagonal matrix.

Rank Deficiency and Pseudorank

The usual definition of the rank of a matrix is the maximum number of independent columns in the matrix. A practical definition of the rank of a matrix is the number of non-zero singular values. An m-by-n matrix with $m \geq n$ is said to be of full rank if $r = n$ or rank deficient if $r < n$. The value of r, called pseudorank, can be easily determined if the magnitude of singular values fall into two clearly distinguishable groups: the larger ones representing the underlying signal of information that is being modeled, the smaller ones representing noise and round-off accumulation. Small singular values generally contribute little to the validity or accuracy of the model. The pseudorank threshold (r) determines the cut-off between these two groups of singular values and is chosen generally on the basis of statistical heuristics originating in the model. In realistic inverse problems, the singular values smoothly decline in size making it difficult to distinguish between these two groups. One solution to this problem is to ***assume*** some cut-off size for singular values and then consider any values smaller than this as equal to zero. This involves a tolerance, τ, which reflects the accuracy of the original data and the accuracy of the floating point arithmetic being used. This arbitrary value is associated with the non-uniqueness of the least-squares solution. Changes in the data and round-off errors less than τ can result in an entirely different set of solutions which also satisfies the least-squares criterion; however, if columns of the matrix A are linearly independent, i.e. if A has a full column rank, then there is one unique solution to the least-squares problem. Neglecting singular values less than τ has the effect of decreasing the condition number[2] to the ratio of the maximum singular value to τ. Since the condition number is an error magnification factor (increase in variance), this results in a more reliable determination of the estimated solution. The resulting estimate of the solution is no longer exactly the natural one; however, the solution is generally close to the natural solution and possesses better variance. The cost of this increase in reliability is a possible increase in the size of the residues; i.e. while the variance is improved

[2] The condition number in terms of singular values is defined as the ratio of the maximum singular value to the minimum singular value.

the model and data resolution are degraded. The precise value of the absolute error tolerance, τ, used as the cutoff parameter must be chosen so that the relative merits of having a solution with small variance against those of having one that fits the data is well balanced.

For example, if the data are accurate up to four significant digits, then relative error of $\delta b = 0.0001$ is appropriate. The absolute error tolerance τ is then obtained from

$$\tau = \delta b \times s_{max} \tag{1}$$

Further discussion of the tolerance factor, rank deficiency and pseudorank can be found in Golub and Van Loan (1983, p. 169), Forsythe and others (1977, p. 196), and Menke (1984, p. 123).

Sparsity Considerations

The kind of matrices encountered when using conventional multifold reflection seismic data are sparse. Sparsity patterns are sensitive to row and column interchanges. It would be desirable to improve the sparsity patterns by judicious choice of row and column interchanges to minimize the fill-in. When a matrix is arbitrarily sparse (as with reflection seismology data), the rows and columns can be reordered so that it is in approximate "dual-angular" structure in which the fill-in will be restricted to the diagonal and vertical blocks (Gill and Murray, 1976). In addition, this kind of preprocessing allows a simpler data structure to be used and has, especially for problems requiring backing store, substantial implementation advantages (Bjorck, 1976).

We will give an algorithm suitable for multichannel seismic prospecting, generating the matrix A (the design matrix) which possesses the approximate dual-angular structure.

Construction of the Design Matrix and Sparsity

The first step into the forward or inverse modelling is the preparation of the design matrix A. The entries in A are the travel distances a_{ij} where i represents the rows of A, i.e., the observations, and j represents the columns of A, i.e., the unknowns to be solved.

The earth section under investigation is represented by a model that is subdivided into square pixels (building blocks) of side 12.7 m (for a map scale of 1:100,000, 12.7 m correspond to one dot of plotter resolution). It is possible to represent the model by 2-D Fortran character array where each cell has a particular name, row and column number corresponding to a pixel in the model having a particular offset and depth. Therefore, ray tracing in the model is equivalent to the ray tracing in the 2-D Fortran array with a precision of 12.7 m.

Any arbitrary gathering of several pixels constitutes a "motif." Motifs represent the geometrical shapes of the unknown units. They may either be the exact shapes of the unknown units, in which case one may solve for the absolute values of the physical parameters (Q, velocity) corresponding to those units, or they may be the repetitions of a particular polygonal shape, in which case one may solve for both the relative values of the physical parameters and their spatial distribution in the model.

The following geometrical relations may be used for straight-line ray-tracing purposes (see Figure 32):

$$k = \frac{y_r - y_\ell}{x_r - x_\ell};\quad b = y_1 - k(x_1 - x_\ell) - y_\ell;\quad d = y_2 - k(x_2 - x_\ell) - y\ell$$

$$x_3 = x_1 + \frac{x_2 - x_1}{\frac{d}{b} + 1};\quad y_3 = y_1 + \frac{y_2 - y_1}{d_b} + 1$$

$$x_4 = \frac{k^2 x_\ell + k(y_3 - y_\ell) + x_3}{k^2 + 1};\quad y_4 = k(x_4 - x_\ell) + y_\ell$$

$$e = \left[(x_4 - x_1)^2 + (y_4 - y_1)^2\right]^{1/2};\quad f = \left[(x_4 - x_2)^2 + (y_4 - y_2)^2\right]^{1/2};\quad a^2 = (x_2 - x_1)^2 + (y_2 - y_1)^2$$

$$i = \frac{1}{2}\cos^{-1}\left(\frac{e^2 + f^2 - a^2}{2ef}\right) .$$

The stability of a sparse matrix is improved when the coefficients a_{ij} are gathered along the main diagonal and zeros are pushed to the corners (i.e., dual-angular form). To achieve this, the ordering of the motif names (i.e., unknowns) should be done during the ray tracing.

The procedure:

1. Sort the traces with respect to their leftmost station x_1, y_1 as seen in Figure 32.
2. Sort the traces having the same left station in increasing offset order.
3. Start the ray tracing with the first trace in the above double-sort.
4. Advance 12.7 m at a time in a known direction prescibed by the model geometry. along the ray path.
5. If the name of a motif on the ray path has not been registered in the unknowns table, then insert in this new entry; otherwise, proceed to the next step.
6. Add 12.7 m to the previous travel distance corresponding to the ith unknown (i.e., motif) of the jth observation (i.e., trace).

The steps described above may be illustrated by a system of equations with $m = 4$ and $n = 4$ as depicted in Figure 33.

System of equations for velocity:

$$\begin{bmatrix} a_{11}a_{12}0 & 0 \\ a_{21}a_{22}0 & 0 \\ a_{31}a_{32}a_{33}a_{34} \\ a_{41}a_{42}a_{43}a_{44} \end{bmatrix} X \begin{bmatrix} y_1 \\ y_2 \\ y_3 \\ y_4 \end{bmatrix} = \begin{bmatrix} t_1 \\ t_2 \\ t_3 \\ t_4 \end{bmatrix}$$

System of equations for Q:

$$\begin{bmatrix} a_{11}a_{12}0 & 0 \\ a_{21}a_{22}0 & 0 \\ a_{31}a_{32}a_{33}a_{34} \\ a_{41}a_{42}a_{43}a_{44} \end{bmatrix} X \begin{bmatrix} x_1 \\ x_2 \\ x_3 \\ x_4 \end{bmatrix} = \begin{bmatrix} b_1 \\ b_2 \\ b_3 \\ b_4 \end{bmatrix}$$

The maximum number of observations participating in the SVD may be obtained from:

$$m = n_R(n_S - \frac{n_R - 1}{2} - n_G)$$

where m is the number of observations, n_R is the number of data traces per shot, n_S is the number of shots in the record section "window", and n_G is the gap between the shot and the nearest data trace.

If $n_S \leq n_R$, use:

$$m = n_S(\frac{n_S + 1}{2} - n_G)$$

Least-squares Problem

The system of linear equations arising from seismic applications has the form

$$AX = B \tag{2}$$

where A is the design matrix, X is the solution vector, and B is the data vector. The least-squares method is defined as the second median of the Euclidian norm

$$\min_X \|AX - B\|_2 \tag{3}$$

which is equivalent to

$$A^TAX = A^TB \tag{4}$$

Equation (4) is known as the system of "normal equations". The least-squares estimates of X which we denote by $\hat{X}$ would be

$$\hat{X} = A^TB \tag{5}$$

However, the SVD of A is

$$A = USV^T \tag{6}$$

From equation (6), recalling $U^TU = V^TV = I$ and $S^T = 1/S$ we obtain

$$A^T = V\frac{1}{S}U^T \tag{7}$$

Now, substituting equation (7) in equation (5) we obtain the least-squares solution

$$\hat{X} = V\frac{1}{S}U^TB \tag{8}$$

For computer implementation, express matrix equations (2) and (8) ***element wise*** (each element of upper case lettered matrix represented by its lowercase equivalent)

$$\sum_{j=1}^{n} a_{ij}x_j = b_i \tag{9}$$

with $1 \leq i \leq m$ and $1 \leq j \leq n$. Here m and n ($m > n$, i.e. overdetermined case) stand for the number of observations and number of unknowns, respectively. The least-squares estimates of the solution vector

$$\hat{x}_j = \sum_{k=1}^{r} v_{jk}\frac{p_k}{s_k} \tag{10}$$

where

$$p_k = \sum_{i=1}^{m} u_{ik} b_i \tag{11}$$

with $1 \leq k \leq r$. Here r ($r \leq n$) stands for pseudorank

$$\sigma = \sqrt{\frac{1}{m-n} \sum_{i=1}^{m} (b_i - \sum_{j=1}^{n} a_{ij} x_j)^2} \tag{12}$$

The number σ can be interpreted as an unbiased estimate of the standard deviation of errors in the data vector B.

Lawson and Hanson (1974, p. 198) report that inspection of the columns of the matrix V associated with small singular values is an effective technique for identifying the sets of columns of A that are nearly linearly dependent.

Following this idea we derived

$$\hat{\delta x_j} = \sigma \sqrt{\frac{1}{r} \sum_{k=1}^{r} (\frac{v_{jk}}{s_k})^2} \tag{13}$$

We interpret $\hat{\delta x_j}$ as the estimated error of the j^{th} least-squares solution. Note that $\hat{\delta x_j}$ includes both the error coming from the data (i.e. σ) and the error introduced by the decomposition process of the design matrix.

Testing the resolving power of SVD

We have tested the resolving power of SVD on different models and using various motifs.

Synthetic models were generated on a 660m × 660m square-shaped geological section. The section area itself is discretized with 10m × 10m square building blocks herein called "pixels"; the size of a pixel was arbitrarily taken to be equal to 1/3 of the receiver group spacing. Along the 660m top side (surface), 23 stations are distributed with a receiver group spacing of 30m.

Assuming, for a convenient example, 23 (stations) X 22 (receivers) = 506 observations, with split-spread recording, half of the traces are just the same as the other half, because they travel along the same ray path, but in opposite directions. As far as the design matrix **A** is concerned, this is just redundant information, i.e. the second half of the traces bring nothing new but identical rows in the design matrix. Therefore, the actual number of observations will be m = 253. However, in real data all 506 traces are useful in the sense that they provide a choice of selecting the good traces or averaging the data. A reflector parallel to the surface constitutes the bottom side of the geological section at a depth of 660m. The seismic raypaths are assumed to follow straight lines, down and up. There is no bending of seismic waves (See Figure 34a).

The geological section was simulated with a 66 × 66 FORTRAN character array (or alphanumeric matrix). Therefore, any arbitrary model can be generated in this frame by just assigning rock names (character variables such as A3, B8, etc.) to the appropriate pixels of this two dimensional character array.

The ultimate goal of inverse modeling is to solve for both geometrical boundaries (shapes) of geological structures and their physical properties (in our present application velocity or Q); however, with conventional multifold seismic reflection data acquired from the surface, our capacity to collect data about the subject to be investigated is not as good as that of the physician's CAT scanner. We can move only along a straight line above the subject; the physician is able to move *around* his subject. Indeed we can improve our ability to observe if we expand our observations to drill-holes surrounding the subject under investigation. A solution based on a few observations but evenly distributed in space is far more accurate than one based on many observations but all accumulated at one location in space.

Partition Motifs and Pixels

We arbitrarily partition (subdivide) the geologic cross-section into one of four different types of shapes, herein called "motifs". Each motif is composed of an arbitrary number of

pixels. The partition motifs examined were square, diamond, cross, and variable (Figure 35a, b, c, and d, respectively) motifs although they can be any shape. Their related design matrices, **A**, are shown in Figure 36a, b, c, and d. The blank parts indicate the structural zeros (sparsity) in the design matrices.

The design matrices corresponding to each type of partition motif are decomposed with the SVD subroutine given by Forsythe and others (1977, p. 229). With the number of observations m = 253 and the error estimate $\delta b = 0.0001$ the following table is obtained:

Motif type	**Square**	**Diamond**	**Cross**	**Variable**
Area (pixels)	36	24	20	9-144
Perimeter (pixels)	24	24	24	12-48
MSF	0.785	0.523	0.436	0.785
Number of unknowns	126	195	245	203
Pseudorank	126	193	230	203
VAX 11/780 CPU time (sec)	220	515	850	645

A "Motif Stability Factor (MSF)" is defined herein as

$$\text{MSF} = 4\pi \frac{\text{Area}}{(\text{Perimeter})^2}$$

where "Area" is the area of a motif in pixels, and "Perimeter" is the perimeter of a motif in pixels. Thus, the MSF quantitatively compares the shape of any motif relative to the circle. Note that the MSF of a circle is one, and is independent of the size of the motif.

The spectrum of the data kernel (Menke, 1984, p. 123) corresponding to these four motifs is shown in Figure 36e. The spectrum of the data kernel is the plot of the magnitudes of the singular values against their index numbers.

The resolving power of each motif was tested by assigning random numbers to the unknowns. The models based on random numbers for the motifs are shown in Figure 37. Their least-squares SVD solution are shown in Figure 38. Their error estimates are shown in Figure 39.

Although SVD may be used to attempt to solve simultaneously for the Q or velocity values and their spatial variations throughout arbitrary geological structures, least-squares solutions obtained from SVD do not return the *correct* absolute values that were supplied when generating the synthetic models if the Q or velocity and structure are both required at the same time. The solution vector is seen to have been multiplied by a scale factor and negative values are common. Nevertheless, the correct relative positions of Q or velocities in the model and their correct relative magnitudes are preserved, but a simple shifting and scaling operation on the solution vector is required. This is simply the consequence of the motif boundaries not coinciding exactly with the boundaries of the contrasts in the Q or velocity. This is not serious because there are numerous problems that are satisfactorily solved by knowing the approximate location only of a contrast in a physical property (the best example of this is conventional reflection seismology data for which only *relative* amplitudes and shapes are generally considered anyway). Note that if the model geometry is known, then correct values of the Q velocity can be recovered. As an example, if the lower and upper limits of Q in the geologic model under investigation are expected to be 100 and 600, respectively, then the solution vector will be shifted toward the positive values and scaled so that computed Q values are stretched to lie between 100 and 600. The Q values so obtained are not the absolute values we seek; however, relative values of Q are as important as absolute values for many applications, especially when searching for locations and shapes of geological structures where the visual contrast is of interest. We will see in "Use of a priori Information" that additional information supplied during the solution process will improve the results and eliminate this shifting-scaling operation. Essentially, the "additional information" reduces the number of unknowns, but "fitness of the motif geometry" to the actual contrasts in the Q or velocity is equally important.

Inspection of the error estimate plots (i.e. Figure 39) indicates that motifs located at the leftmost and rightmost sides of the section have large errors. This is to be expected because these motifs are visited by fewer raypaths than the others. The intersection frequency of the seismic raypaths to each pixel is shown in Figure 34b. In fact, the variable motif size was created in order to balance the ray distribution among the motifs.

Image Enhancement

Prior to display of the results, two procedures for image enhancement were applied to the solution vector:

1. Eliminate outlying values with a technique similar to "Chevaunet's criterion". The arithmetic mean and standard deviation of the solution values were computed. Any value whose absolute difference from the mean is larger than 1.96 (probability of 5%) standard deviations is rejected. The remaining values are scanned for maximum and minimum values. The previously rejected values are accepted again by substituting their values with the maximum value if the rejected value was larger than the mean, or the minimum value if the rejected value was smaller than the mean.
2. "Histogram equalization" (Jensen, 1986, p. 129) enhances the contrast between different values of the solution vector. The method has for its basis stretching a piecewise linear contrast; i.e. selective pieces of the histogram are linearly contrast stretched where the slope of the linear contrast enhancement changes.

Image enhancement is viewed here as an interpretive aid because it highlights differences in the solution vector or error estimates so that the resolving power of SVD techniques is more readily evaluated. *Contrasts* in the solution vector are increased after image enhancement.

In this example, 5 adjacent intervals were selected; i.e., Q value *gates* are 100-200, 200-300, 300-400, 400-500, 500-600. n solution values are distributed among these intervals according

to their magnitudes. The number of occurrence of solution values in each interval proportionally weights the slope of the linear contrast stretch in that interval. Using the number of occurrence criterion as a weight factor, in a given interval, it is possible to enhance the contrast among the solution values which are large in numbers but small in their magnitude differences.

On the figures, when examining a model and its corresponding solution, the relative variations in the model should be compared with the relative variations in the solution. Image enhancement degrades the absolute accuracy of values of Q or velocity, but emphasizes contrasts in these physical properties.

Synthetic Models

Four different synthetic models were generated as shown in Figure 40. The four motif shapes were tested on each model. The results are shown in Figure 41 for square motifs, Figure 42 for diamond motifs, Figure 43 for cross motifs, and Figure 44 for variable motifs.

Error Analysis

Random noise of 10%, 20%, 30%, and 40% was added to the data vector of Model 1. in Figure 40a. When adding random noise to data vector B, a more stringent method of measuring the noise was used instead of the conventional RMS criteria. The scale factor of the random numbers (which are algebraically added to the data vector after they are scaled) is the percent value of the maximum data value in vector B.

Solutions for 10%, 20%, 30%, and 40% random noise are shown in Figure 45.

Use of a priori Information

"A priori" information results in great improvements in the SVD solutions. Two possible kinds of a priori information may be furnished for the solution process. They are defined as follows:

- The geometrical shape(s) of geologic structures, i. e., the internal model geometry may be known from a conventional stack, and
- A known or assumed equality in physical properties (Q or velocity) of various parts of the geologic section.

Either of the above reduces the number of unknowns. Note that the model geometry is, in fact, generally known for any reflection seismic data that has a good S/N ratio.

A synthetic model that is analyzed by each time assuming new information for the solution process is shown in Figure 46a. This model has a "transitional zone" in the middle layer which we wish to resolve.

Apply three a priori information situations as follows:

- *First.* Begin with the information that the upper and lower boundaries of the layers are known (in this case they are parallel and all of the same thickness). The solution for this situation is shown in Figure 46b.
- *Second. **Add*** (by altering the alphanumeric matrix) the information that the layers above and below the target layer contain no transitional zone. Therefore, these layers can be considered to be simply wide rectangles. The solution for the second case is shown in Figure 46c.
- *Third. **Add*** the information (by altering the alphanumeric matrix) that the layers above and below the target layer are alternating layers composed of only two different rock types. The solution for the third situation is shown in Figure 46d.

Note that as the amount of a priori (known) information increases, the SVD solutions improve drastically. The decrease in the number of unkowns reduces the condition number. Therefore, not only the error magnification is reduced, but full rank (i.e. r = n) situation leading to a unique solution is achieved.

Comparison of SVD solution methods with conventional methods

The computational benefits of using the SVD solution rather than a conventional solution can best be appreciated with a small numerical example. Consider a simple well posed problem with two equations and two unknowns.[3] The exact solution for this problem is the vector

$$\begin{bmatrix} \delta_1 \\ \delta_2 \end{bmatrix} = \begin{bmatrix} 1.2 \\ 0.6 \end{bmatrix}$$

We consider the effect of scaling on these solutions by multiplying the first equation by an arbitrary integral power of 10 and then computing the solution for

$$Z\,\delta = g \ ,$$

where

$$Z = \begin{bmatrix} 4.0s & 2.0s \\ 2.0 & -1.0 \end{bmatrix}$$

and

$$g = \begin{bmatrix} 6.0s \\ 1.8 \end{bmatrix} \ ,$$

---

[3] This example is taken directly from L.R. Lines and S. Treitel, Tutorial, a review of least-squares inversion and its applications to geophysical prospecting, 32, 159-186, 1984.

and where

$$s = 10^m$$

Table A-4.1. Numerical comparison between SVD and normal equation solutions

Scaling factors	Method (i) (Cholesky)	Method (ii) (Crout)	Method (III) SVD
10	1.19999981	1.19999695	1.19999886
	0.60000262	0.59999845	0.59999487
10^1	1.20002937	1.19992065	1.19999790
	0.59994036	0.60016286	0.59998116
10^2	1.19810200	1.20763683	1.19999790
	0.60379499	0.58468812	0.59999865
10^3	3.51085280	0.77235425	1.19999981
	-4.02170181	1.45528984	0.60000014
10^{13}			1.19999981
			0.59999428

Three techniques were used to solve the normal equations for δ, namely (i) Cholesky factorization, (ii) Gaussian elimination with Crout's method, and (iii) singular value decomposition (SVD). The results of our single precision computations are summarized in Table 1.

Evidently, the SVD method is by far the most robust. In double precision, all methods produced accurate answers up to $s = 10^8$; then SVD proved superior. Lines and Treitel concluded that SVD provided by far the greatest numerical robustness (see also Lawson and Hanson, 1974; Stewart, 1973).

APPENDIX 3 - SVD SOLUTIONS USING SYNTHETIC DATA

The software was tested with synthetic data for

- Velocity inversion of the traveled layers
- Q inversion of the traveled layers
- Velocity inversion of the reflecting layer.

The input model and the input parameters are shown in Figure 47.

207 synthetic traces were created using a 50 ms Klauder wavelet (Δ = 2 ms) of 10-80 Hz frequency content. The synthetic seismogram is shown in Figure 48. The corresponding seismic rays in the model are shown in Figure 49. The solutions to this synthetic model are shown in Figure 50.

Noise tests were also performed on the synthetic data. The velocity and Q values of a single layer model (the corresponding figures are not shown) are solved using 171 synthetic traces obtained from a model of 12 km depth and 18 km width. The exact input values are velocity = 5000 m/s and Q = 270.

The magnitude of the white noise added to a trace is an arbitrary percent of the maximum absolute value found in the time series. The results of the noise tests are shown in the Table 6.

Table 6. Results of noise tests

White Noise (Percent)	Velocity (m/s) Observed Value	Velocity (m/s) Absolute Error	Velocity (m/s) Relative Error	Seismic Q Observed Value	Seismic Q Absolute Error	Seismic Q Relative Error
10	5008	8	0.16	223	-47	17
20	5012	12	0.24	210	-60	22
30	5013	13	0.26	211	-59	22
40	5015	15	0.30	204	-66	24

APPENDIX 4 - COMMENTS ON THE ANALYSIS OF REAL DATA

The depth-velocity tables used for stacking purposes and the average velocities computed from SVD techniques are shown in Table 7.

Table 7. Depth-velocity tables for ADCOH Line 1

CDP 470		*CDP 400*		*CDP 350*		*CDP 270*		*CDP 220*		*Average*	
V-rms	**Depth**	**V-rms**	**Depth**	**V-rms**	**Depth**	**V-rms**	**Depth**	**V-rms**	**Depth**	**V-SVD**	**Depth**
4750	0	5000	0	4750	0	4750	0	4750	0	6095	1700
5500	825	5250	788	5100	765	5000	1000	5300	1060	6095	1700
5500	1375	5500	1648	5600	1674	5500	2192	3900	1365	5708	4700
5750	2297	5000	2603	5750	4018	5500	3292	4000	2004	5607	6300
5750	4597	5250	3906	5750	6605	5600	3908	5250	3544	5440	8200
6000	5675	5250	6269	5500	7047	5750	5158	5250	5119	5300	10200
5750	6245	5250	9156	5500	10072	5350	5369	5250	9057		
5750	10845	5500	10333	6000	14776	5250	9199	6000	14374		
6000	11803	6000	14751	8000	66968	6000	14516	8000	66566		
8000	67193	8000	66943			8000	66708				

APPENDIX 5 - FUTURE WORK

In the present state of the work, we devised the dynamic analysis window so that it detects some specific shapes (straight line for the absorption coefficient and corresponding approximately half-period sine wave for the dispersive phase spectrum). We will relax these assumptions so that we can study any other possible shapes corresponding to much more complex physical absorption mechanisms. One of them may be local absorption bands in the frequency spectra.

Figure 55 illustrates how a local anomaly (hump) superimposed on the background rectilinear absorption coefficient may effect the dispersive phase and dispersive velocity. Note that the hump has approximately the shape of a half-period sine wave; thus one can observe the corresponding half-period cosine wave (Hilbert transform of sine is cosine) on the dispersive phase curve.

The upward hump on the absorption coefficient curve indicates that there is an excess of attenuation in that particular frequency band. The downward hump indicates that there is less attenuation in that frequency band than the surrounding frequencies. Ecevitoglu (1985) found just this effect on vibroseis data acquired on the Atlantic Coastal Plain, and attributed the cause to 60-Hz electrical interference.

The magnitude effect, location effect, and width effect of the hump are also investigated. They are depicted in Figure 56, Figure 57, Figure 58, respectively.

"Q-spreads"

Special field source-receiver designs will be investigated. They are intended to improve the seismic-ray coverage of the subsurface of the SVD applications.

Vibroseis programmed sweeps

We intend to increase signal to noise ratio at the corners of our interest frequency range. We will investigate the effect of changing amplitude and changing frequency rates of the sweep signal to accomplish this.

Non-linear spreads for better SVD coverage

Non-linear programmable sweeps for better S/N ratio over frequency band of interest

Wider bandwidth (more octaves)

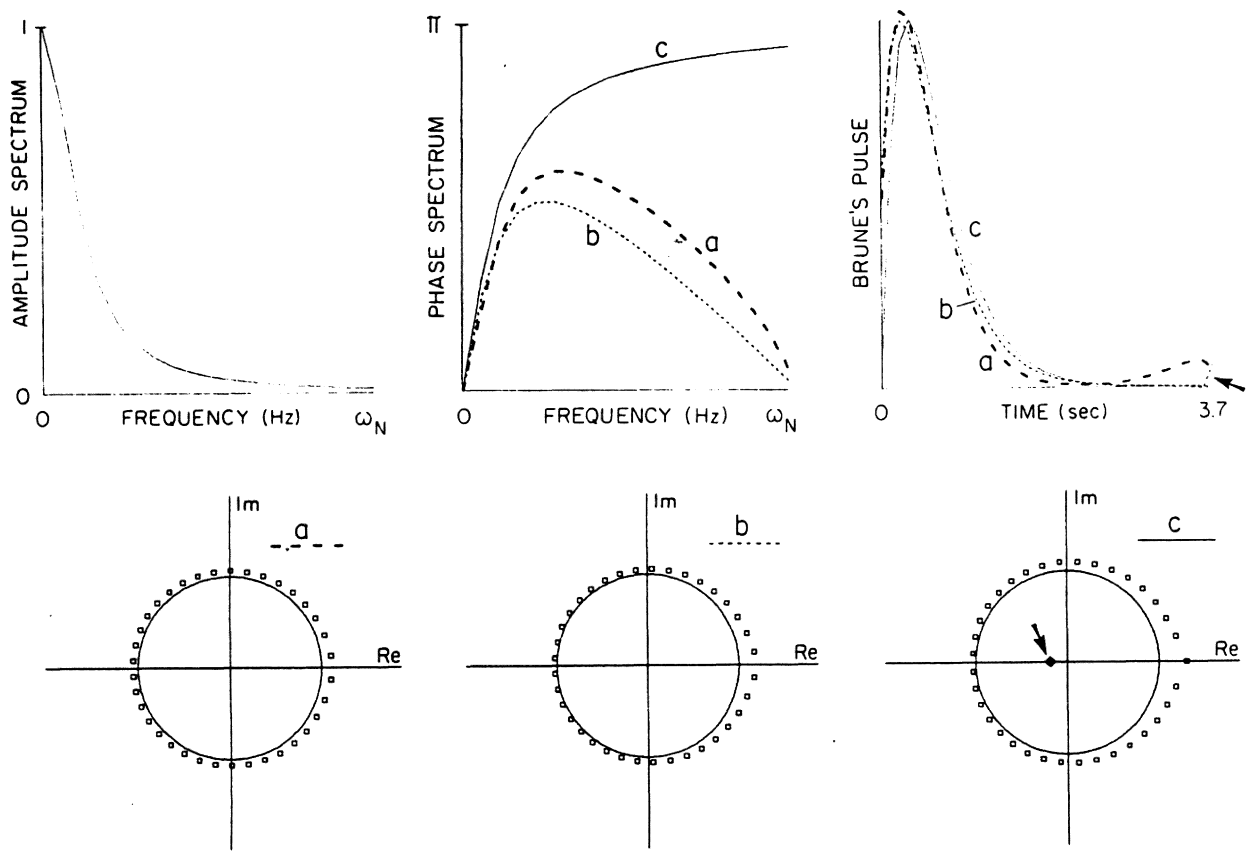

Figure 30. Brune's pulse: Curves (a) are generated using the phase spectrum obtained from discrete Hilbert transform of the natural logarithm of the theoretical amplitude spectrum. Observe that the pulse is minimum-delay and causal. Curves (b) are generated using the 93 ms time-advanced (remember that these are phase-lag curves) theoretical phase spectrum (dt = 100 ms). Observe that the pulse is minimum-delay but the waveform has been shifted into negative time (note the arrow pointing to the tail of the pulse). Curves (c) are generated using the theoretical phase spectrum. Observe that the pulse is causal but not minimum-delay (note the arrow pointing to a root inside the unit circle). The negative of the phase spectrum (i.e., phase-lag spectrum) is shown.

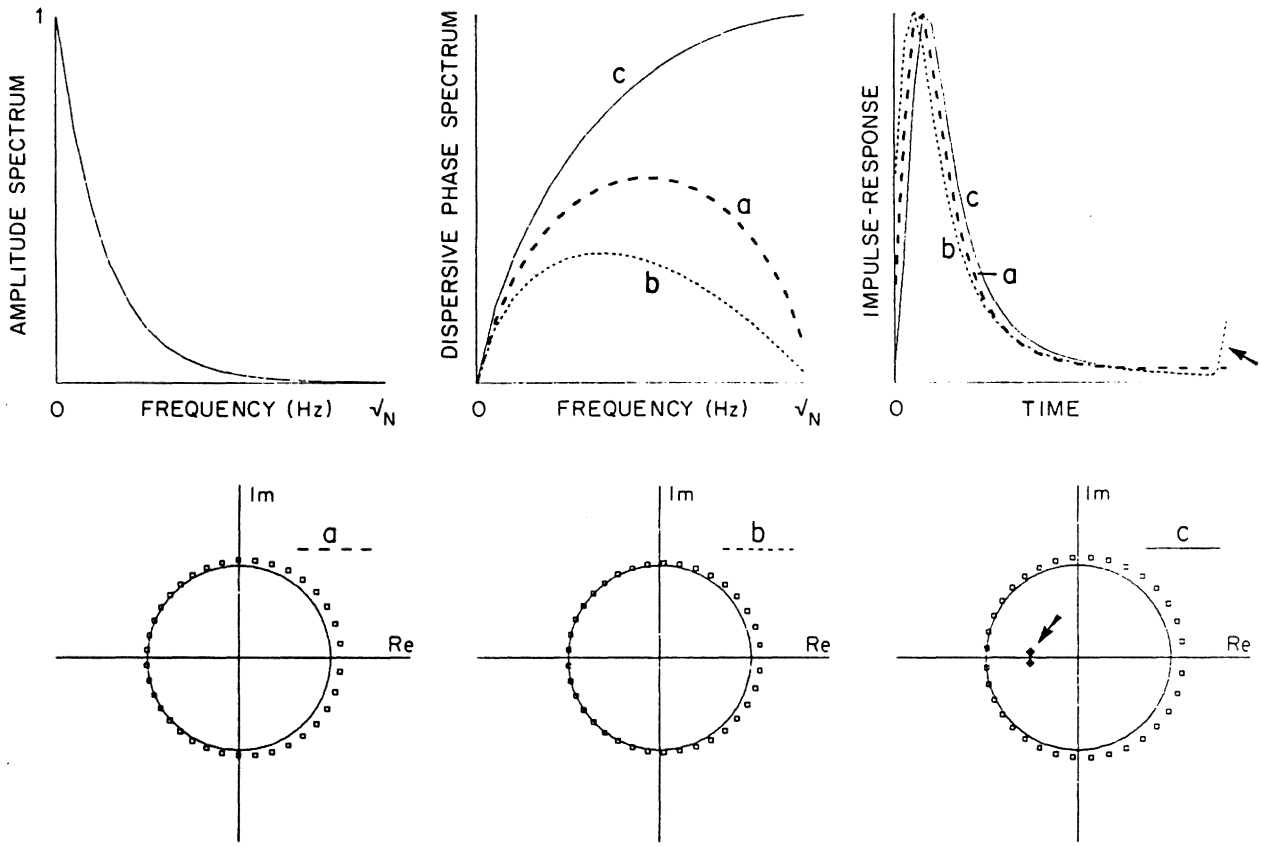

Figure 31. Futterman's pulse: Curves (a), (b), and (c) are equivalent to those in Figure 30. The only difference is Futterman's unbounded phase spectrum (remember that Brune's phase spectrum was bounded by a horizontal asymptote at π): It includes both a pure-delay and pure-dispersive part. Only 0.3% to 1.3% of it is responsible from dispersion which is of interest. Therefore, curve (b) in dispersive phase spectrum is obtained by 1772 ms time-advancing (total travel-time is 1800 ms) Futterman's pulse which becomes minimum-delay but acausal as in Brune's case. To make the pulse causal (but losing its minimum-delay property), a time-delay of 6 ms is applied. The result is the curve (c). Observe the tilt of the curve (b) to the left.

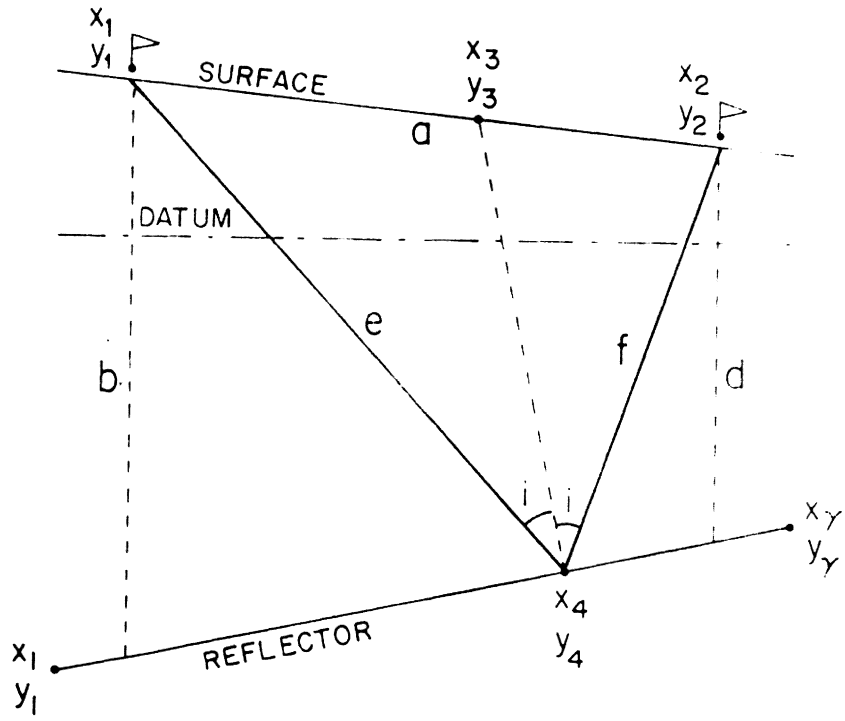

Figure 32. Definitions of the geometrical equations: Descriptions of the source, receiver, and reflection point coordinates.

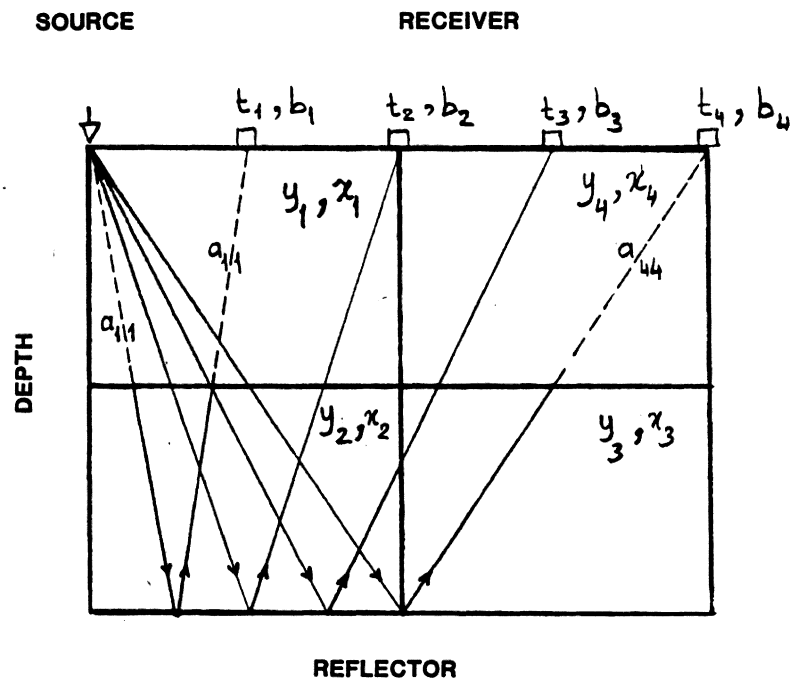

Figure 33. Illustration of matrix designs: Example showing four simultaneous equations with four unknowns.

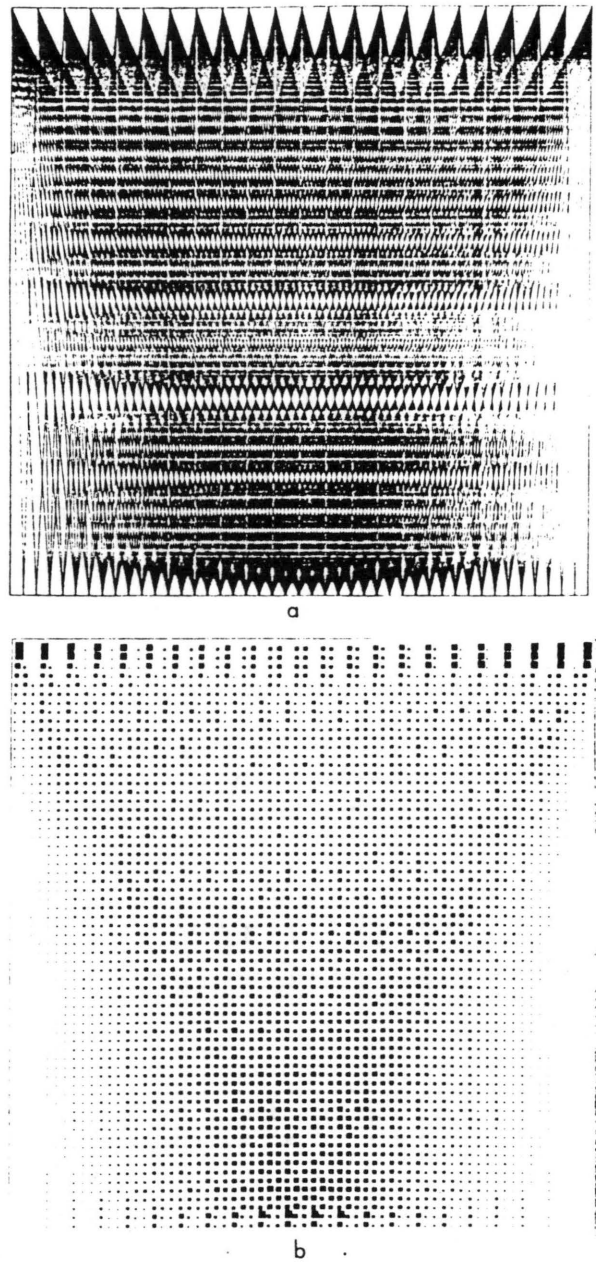

Figure 34. Model section depicting the seismic ray paths and visitation density: (a) Seismic raypaths, (b) Frequency of intersection of seismic rays with each pixel. The larger the dark area, the greater the frequency of intersection of seismic raypaths with each pixel.

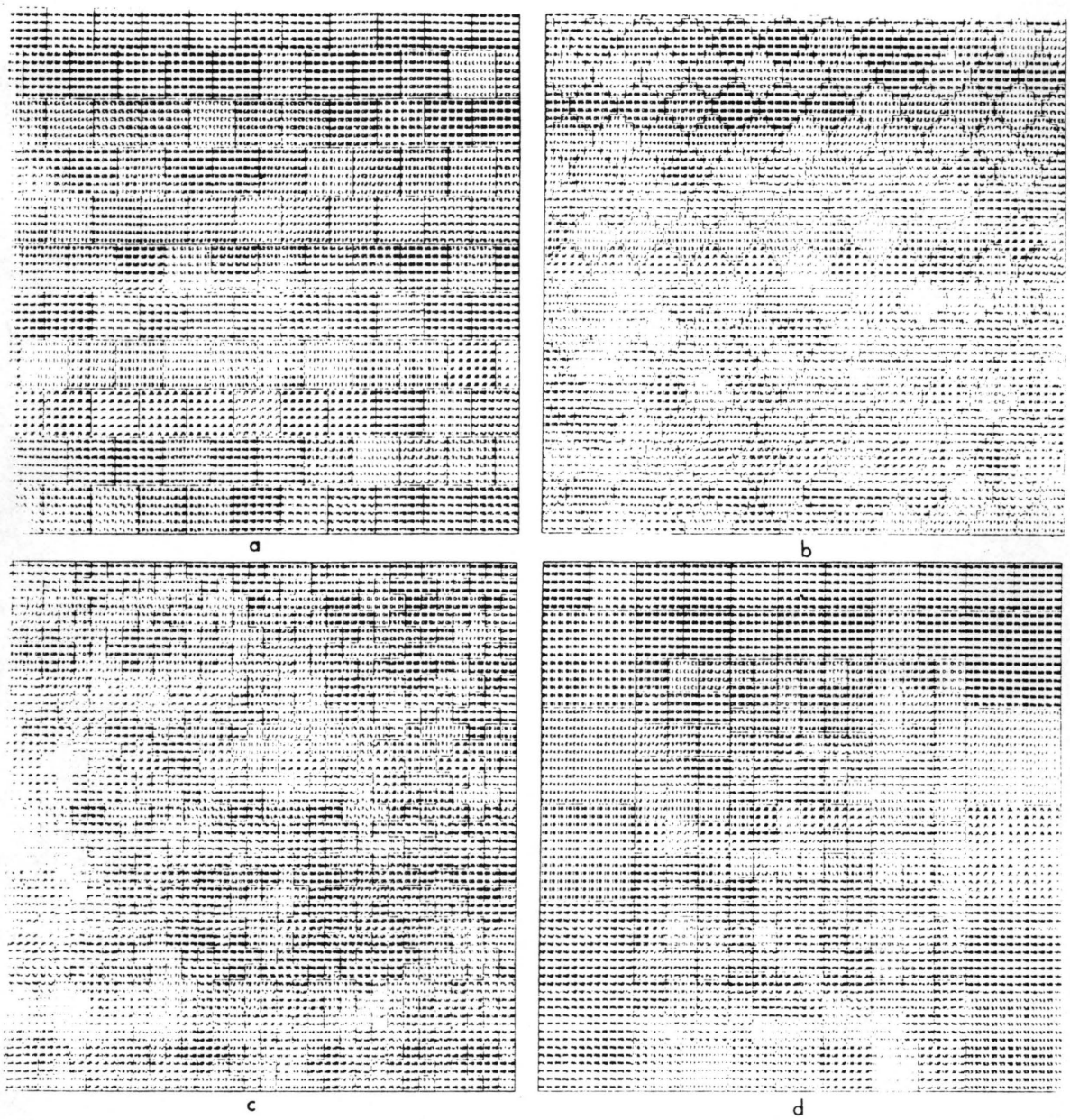

Figure 35. Motifs used to partition xz-space (the geologic model): (a) square, (b) diamond, (c) cross, and (d) variable.

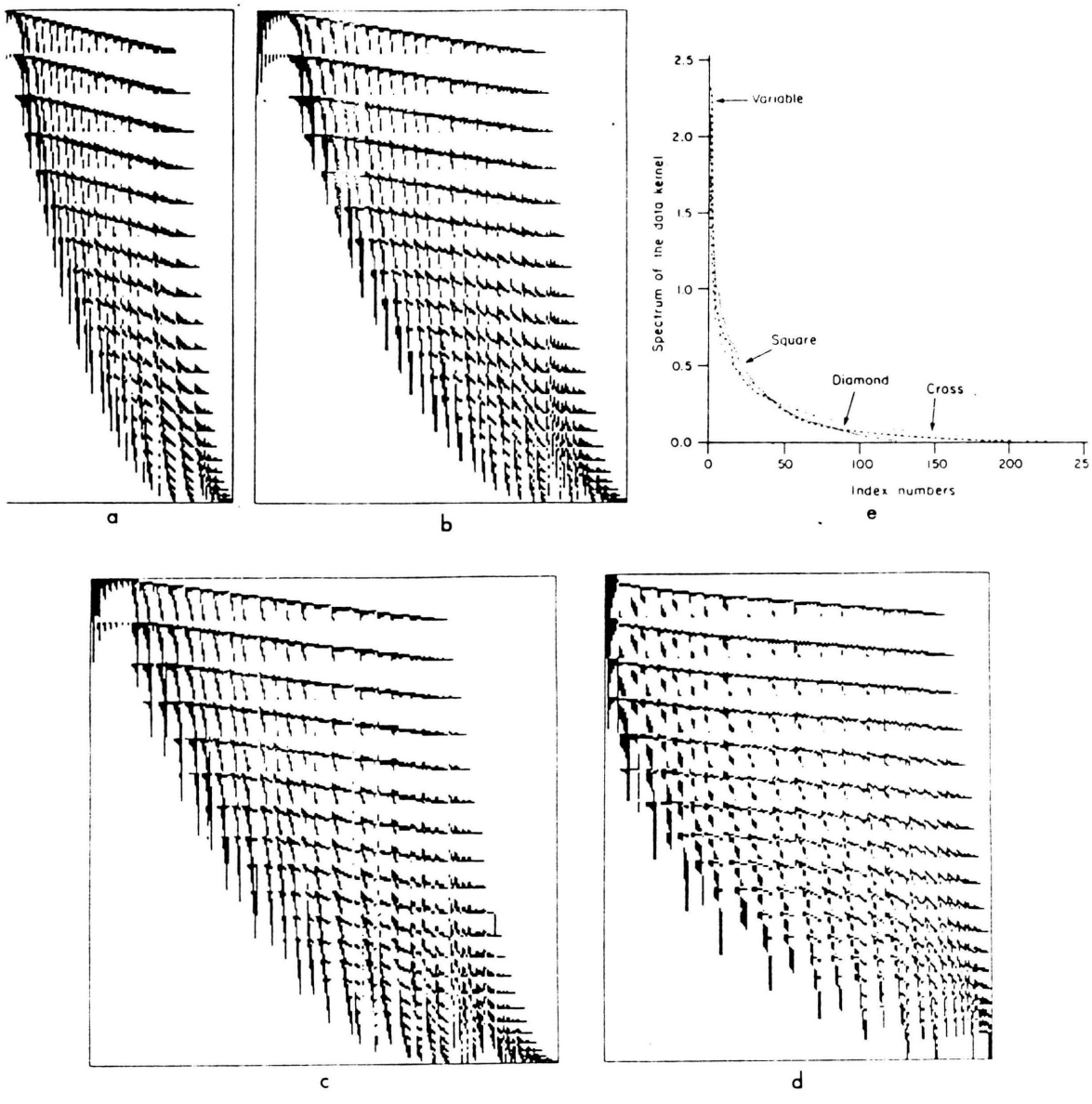

Figure 36. Design matrix sparsity patterns and spectrum of the data kernel: (a) square, (b) diamond, (c) cross, (d) variable, (e) The spectrum of the data kernel corresponding to the motifs.

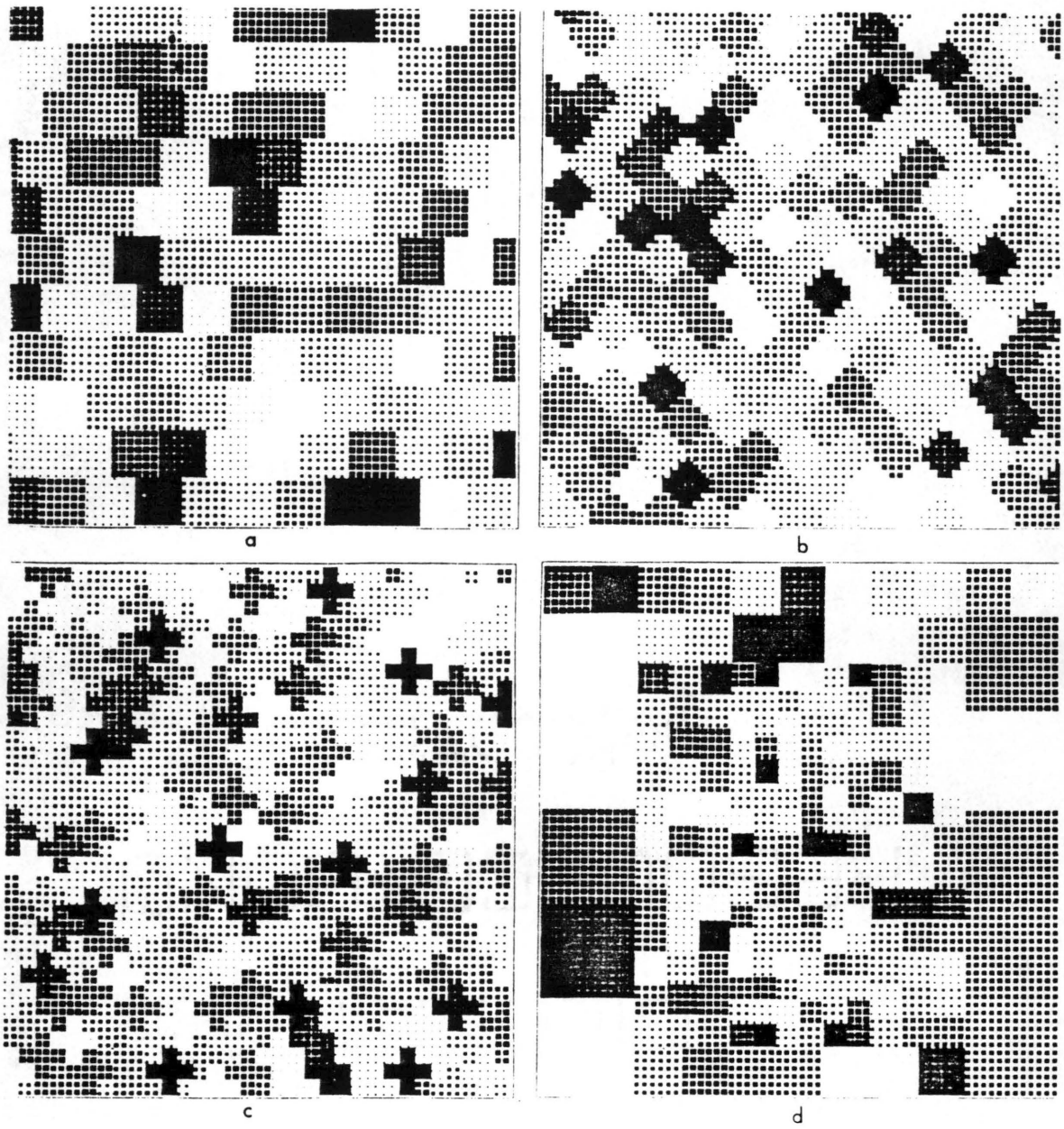

Figure 37. Random number models: (a) Square motifs, (b) Diamond motifs, (c) Cross motifs, (d) Variable motifs.

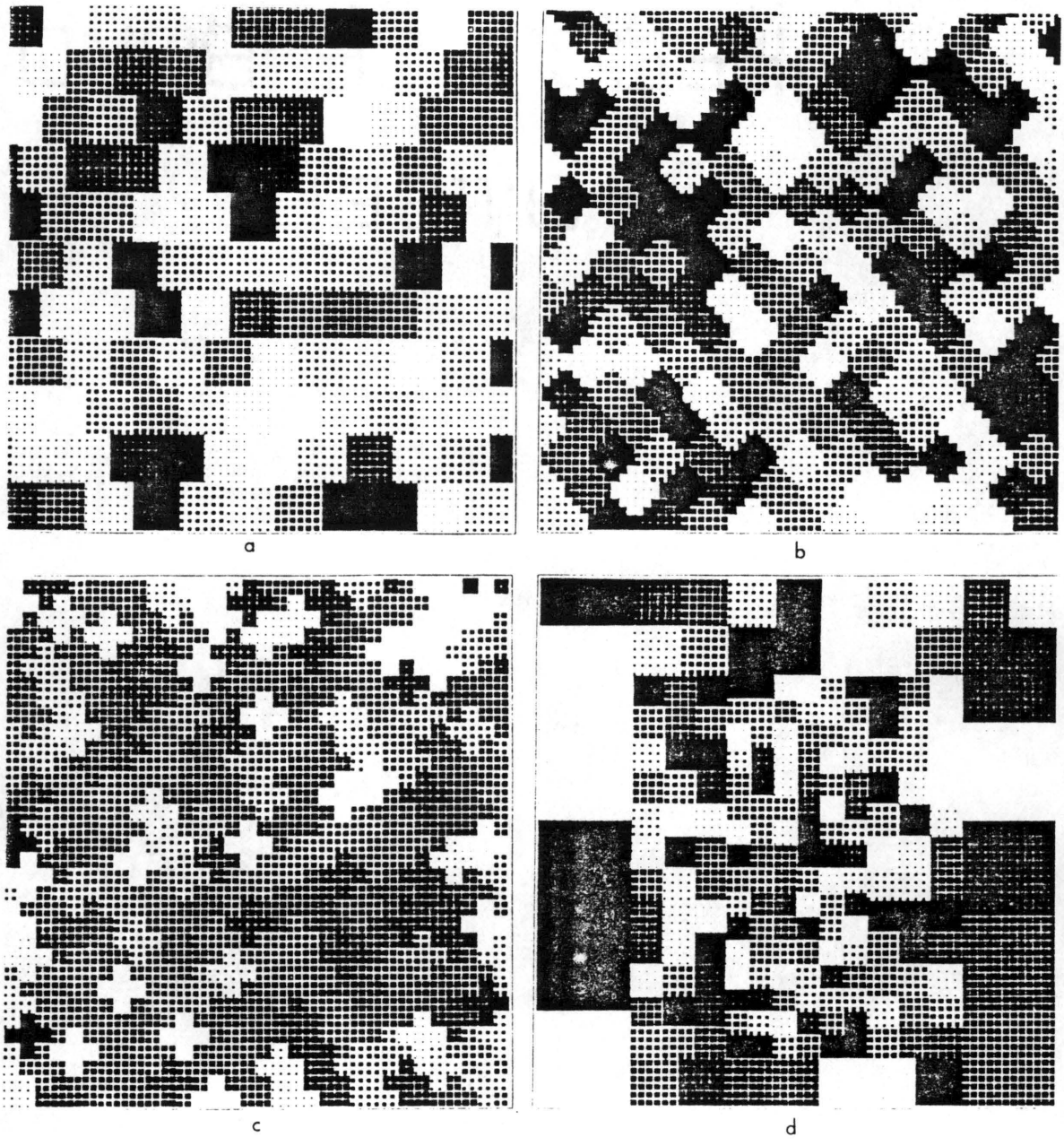

Figure 38. Solutions to the random number models: (a) Square motifs, (b) Diamond motifs, (c) Cross motifs, (d) Variable motifs. The solution vector has been constrained to lie between 100-600, not 1 and 999, the actual dynamic range of the random numbers used to generate the model. In a real application (such as this) the range of values of the random numbers would be unknown (but constrained by physical considerations of possible values of the Q-factor).

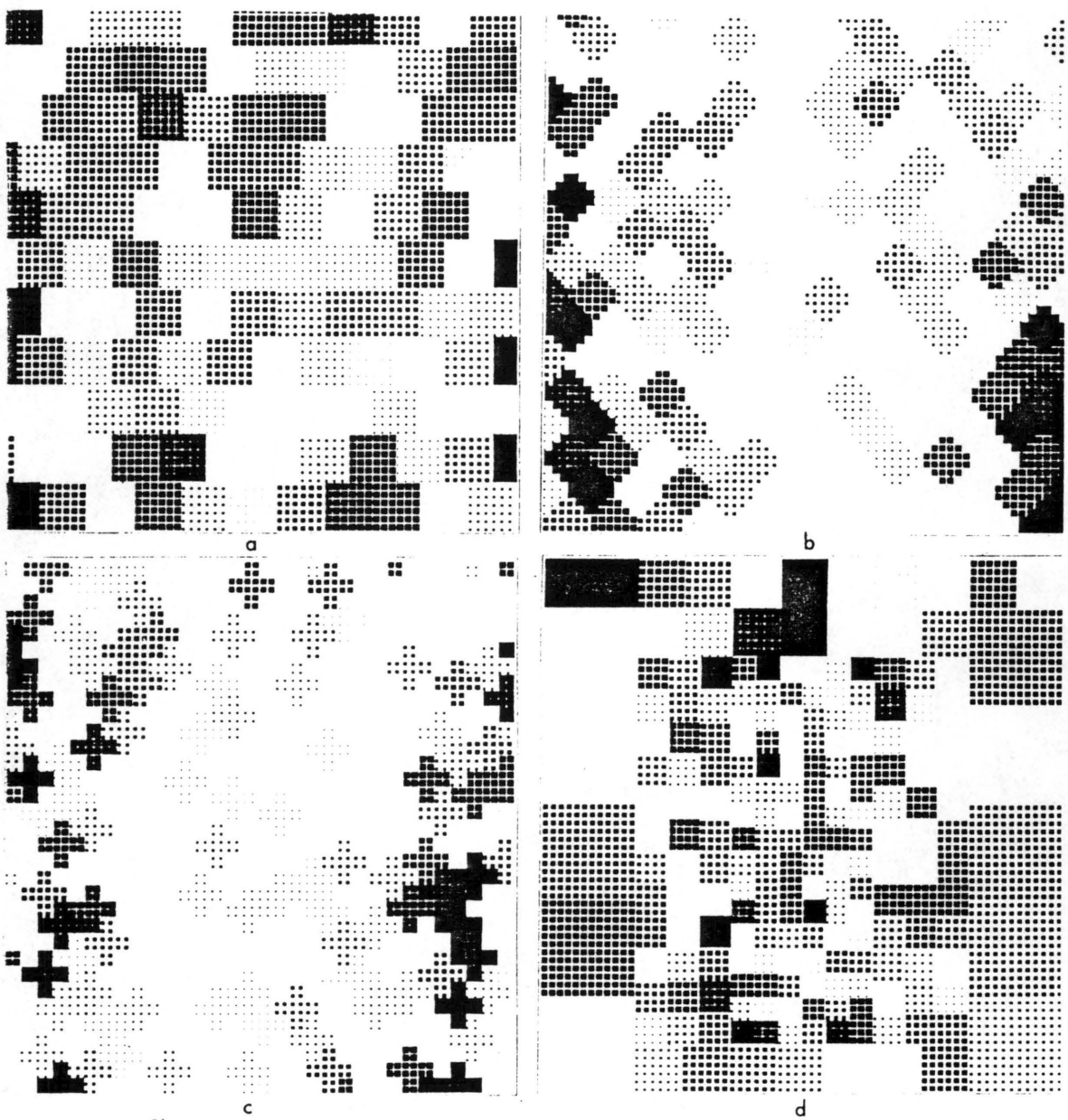

Figure 39. Error estimates of the random number models: (a) Square motifs, (b) Diamond motifs, (c) Cross motifs, (d) Variable motifs. It is important to note that these four diagrams display a much-enhanced error. Image enhancement (which has nothing to do with SVD) has been applied here to enhance the contrast between the unknowns (motifs). The error is much smaller than implied by the actual image-enhanced display. In fact, without image enhancement there would not be enough error in the solution vector to make an interesting display. Compare (c) in this figure with Figure 34b; note that the least error coincides with the highest raypath visitation rate.

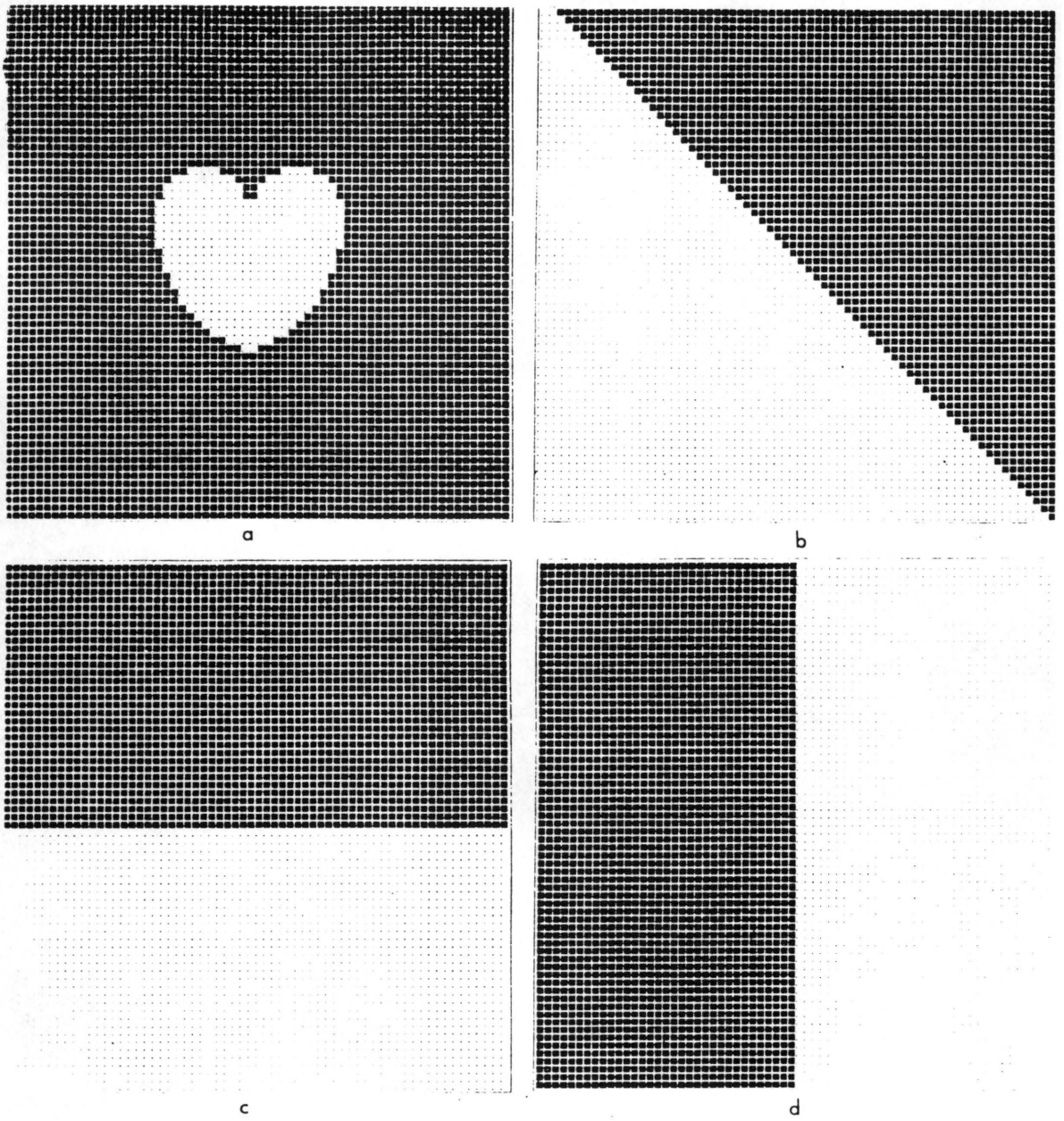

Figure 40. Geologic models used to test the resolving power of SVD: (a) Model 1: granitoid, (b) Model 2: eastward-dipping decollement (diagonal) above a horizontal sole reflector (the bottom of the geologic model), (c) Model 3: horizontal layer, (d) Model 4: vertical strike-slip fault with different rock physical properties on each side of the discontinuity. Note that for the SVD decomposition decribed herein, it is only necessary for raypaths to *cross* the vertical boundary; they do not have to reflect from it. Furthermore, as long as raypaths cross the vertical boundary reflectors are necessary only on one side, not both, of the reflecting boundary; i.e., as would be expected for a (major) strike slip fault, reflectors do not have to be continuous across the boundary.

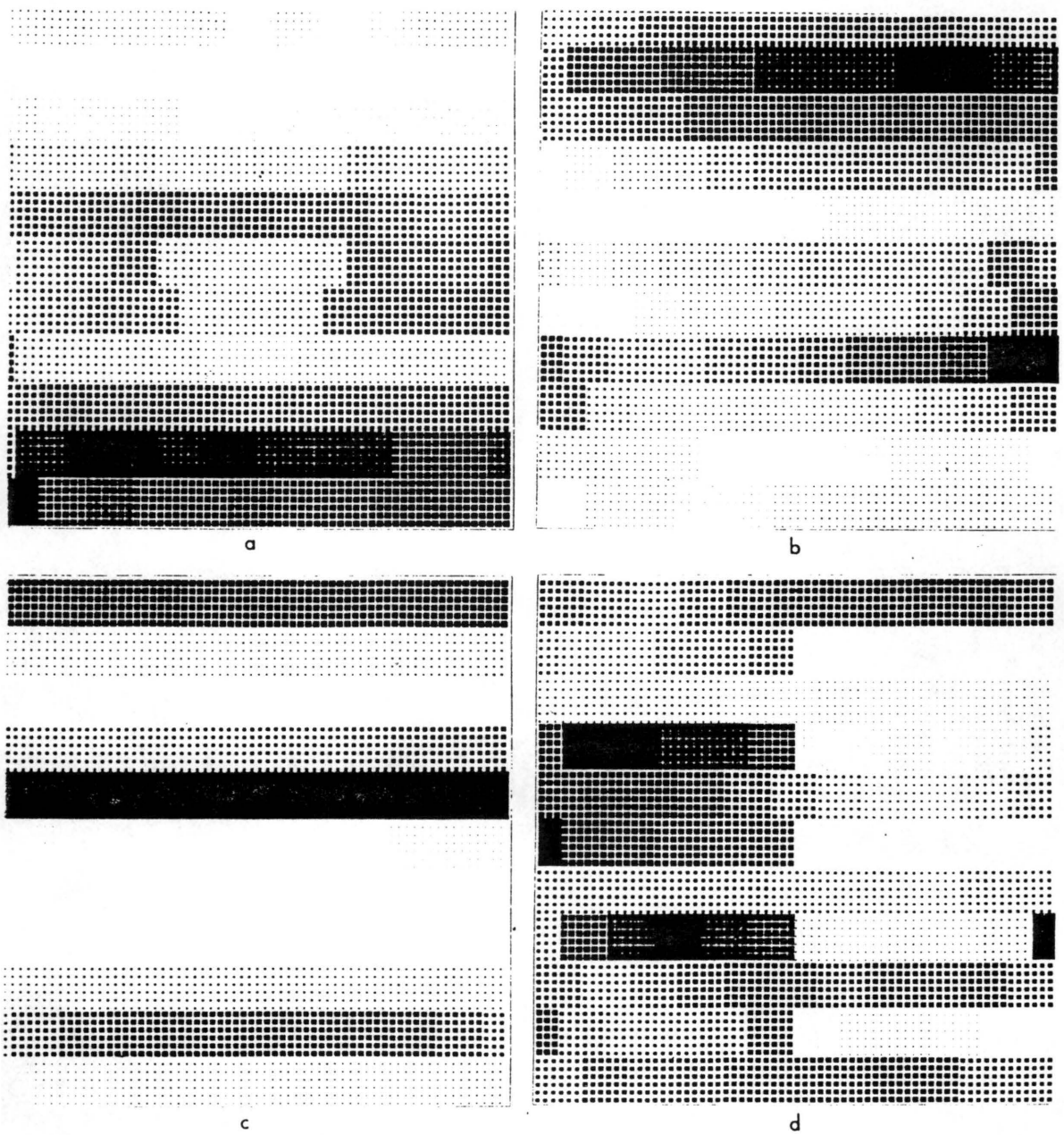

Figure 41. SVD solutions using square motifs: (a) Solution for Model 1, (b) for Model 2, (c) for Model 3, (d) for Model 4. Note (d) and the excellent recovery of the vertical boundary.

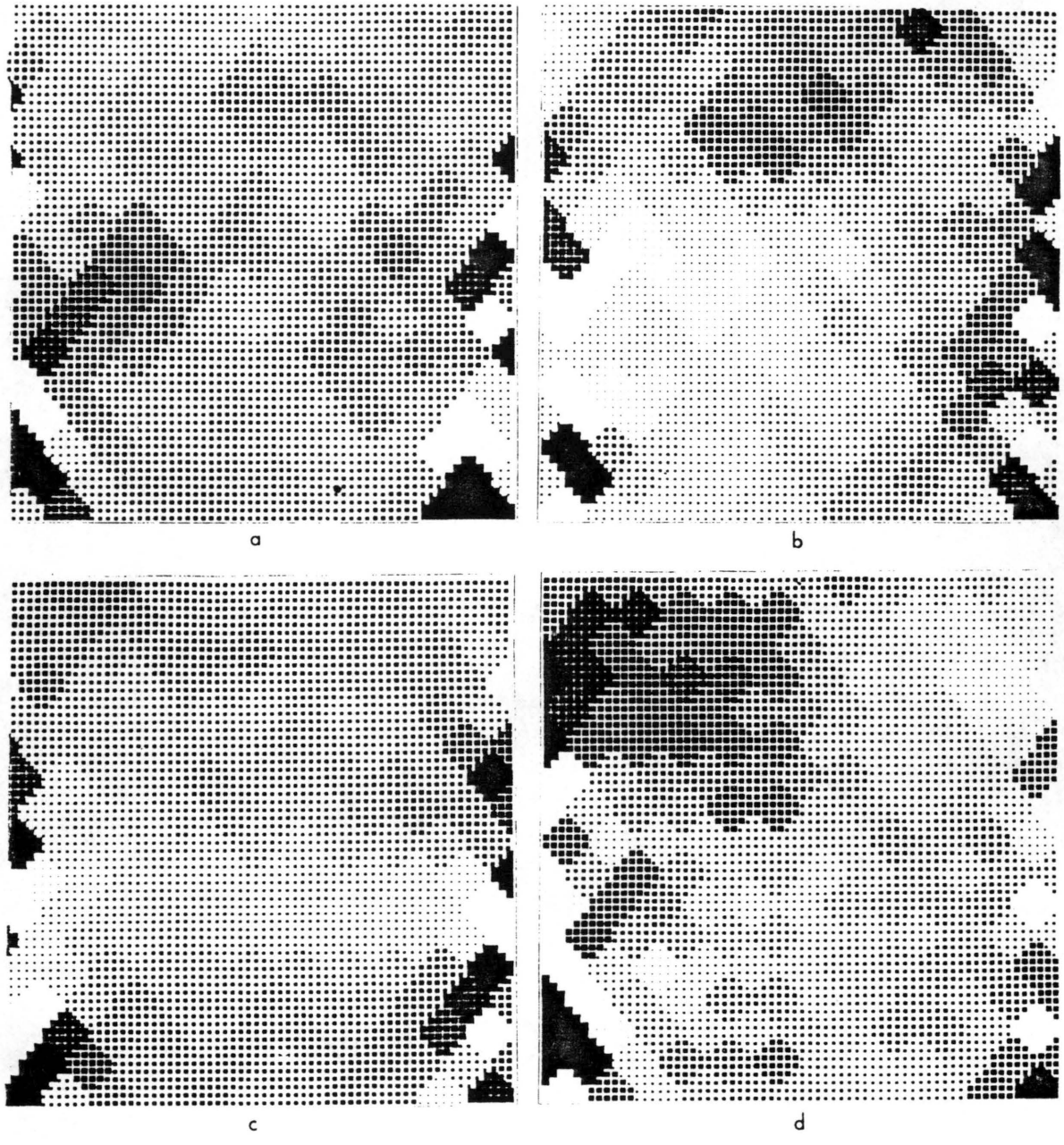

Figure 42. SVD solutions from diamond-shaped motifs: (a) Solution to Model 1, (b) Solution to Model 2, (c) Solution to Model 3, (d) Solution to Model 4.

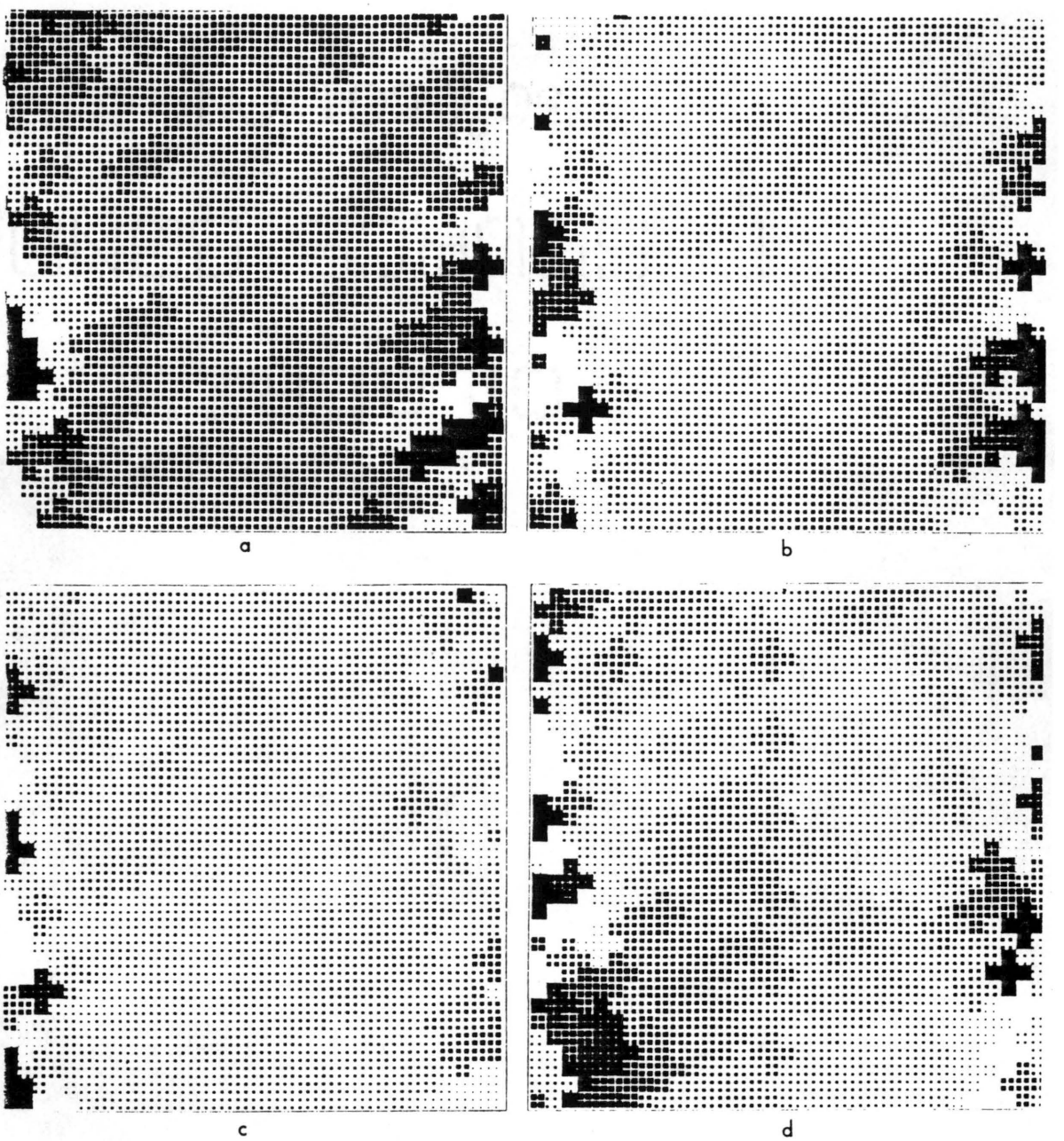

Figure 43. SVD solutions from cross-shaped motifs: (a) Solution for Model 1, (b) Solution for Model 2, (c) Solution for Model 3, (d) Solution for Model 4.

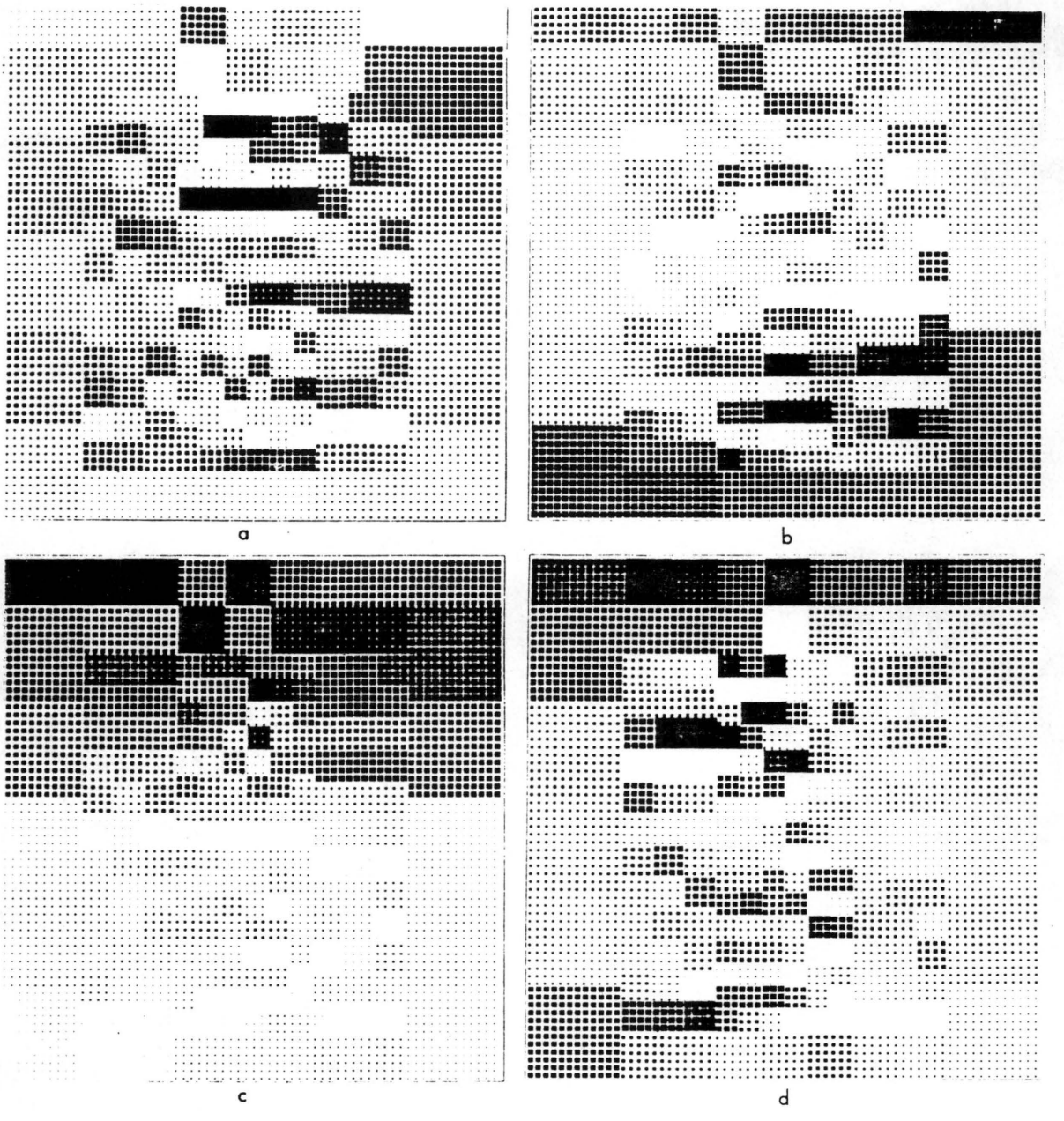

Figure 44. SVD Solutions using variable motifs: (a) for Model 1, (b) for Model 2, (c) for Model 3, (d) for Model 4. Again, the image enhancement process has magnified the errors. In addition, the fact that the motif boundaries do not coincide with the geologic boundaries contributes to error in the solution vector at the boundary. Note that for Model 2 no a priori information is supplied about model geometry. In spite of this SVD detects the contrast across the diagonal "fault". If the model geometry is supplied that the motif geometry can be designed so that the SVD solution is essentially perfect; i.e., values of Qc are perfectly recovered on both sides of the fault. Motif design is most easily accomplished by simple inspection of the stacked CDP data itself.

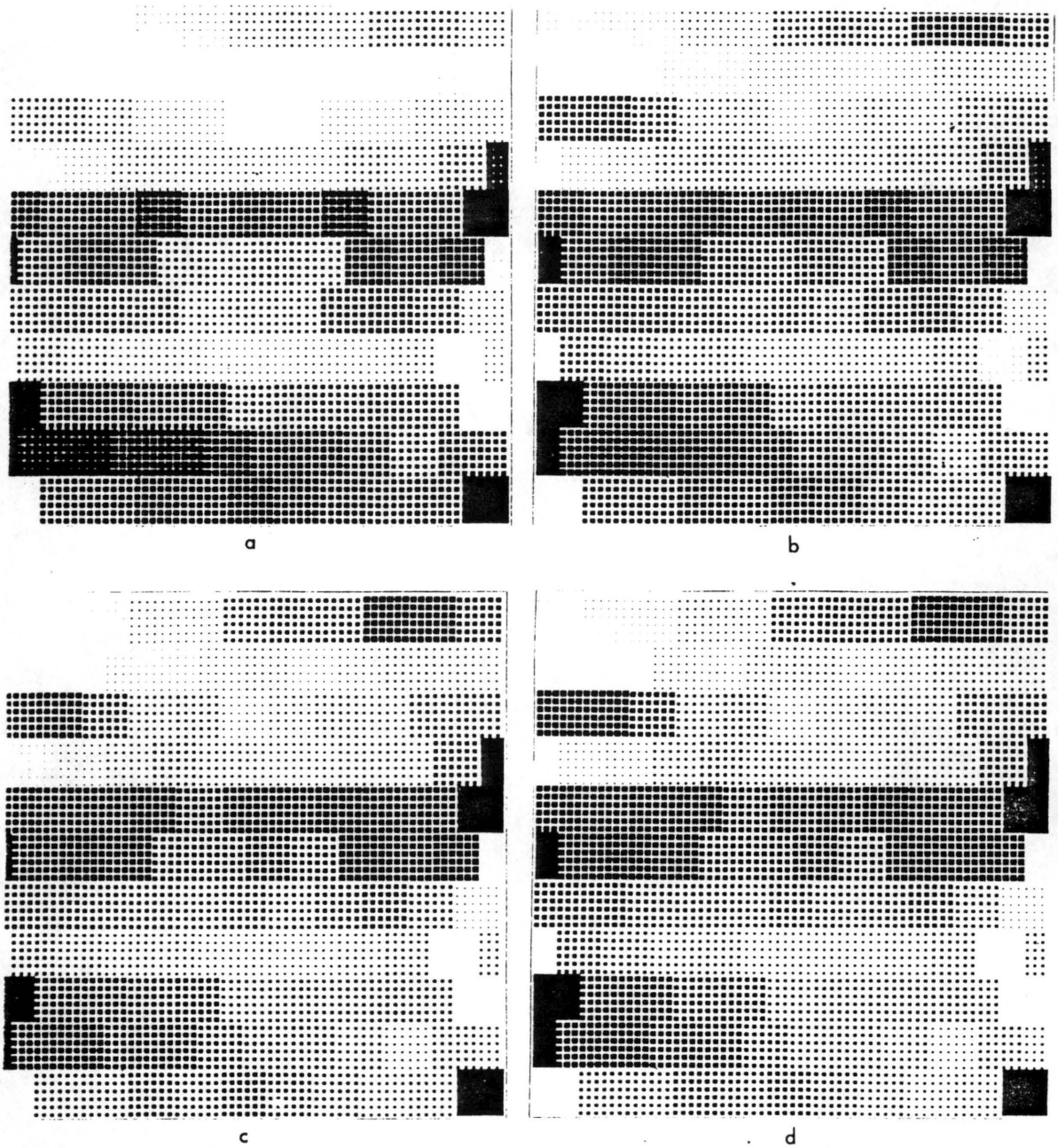

Figure 45. Solutions to Model 1 in the presence of random noise: (a) 10%, (b) 20%, (c) 30%, (d) 40%.

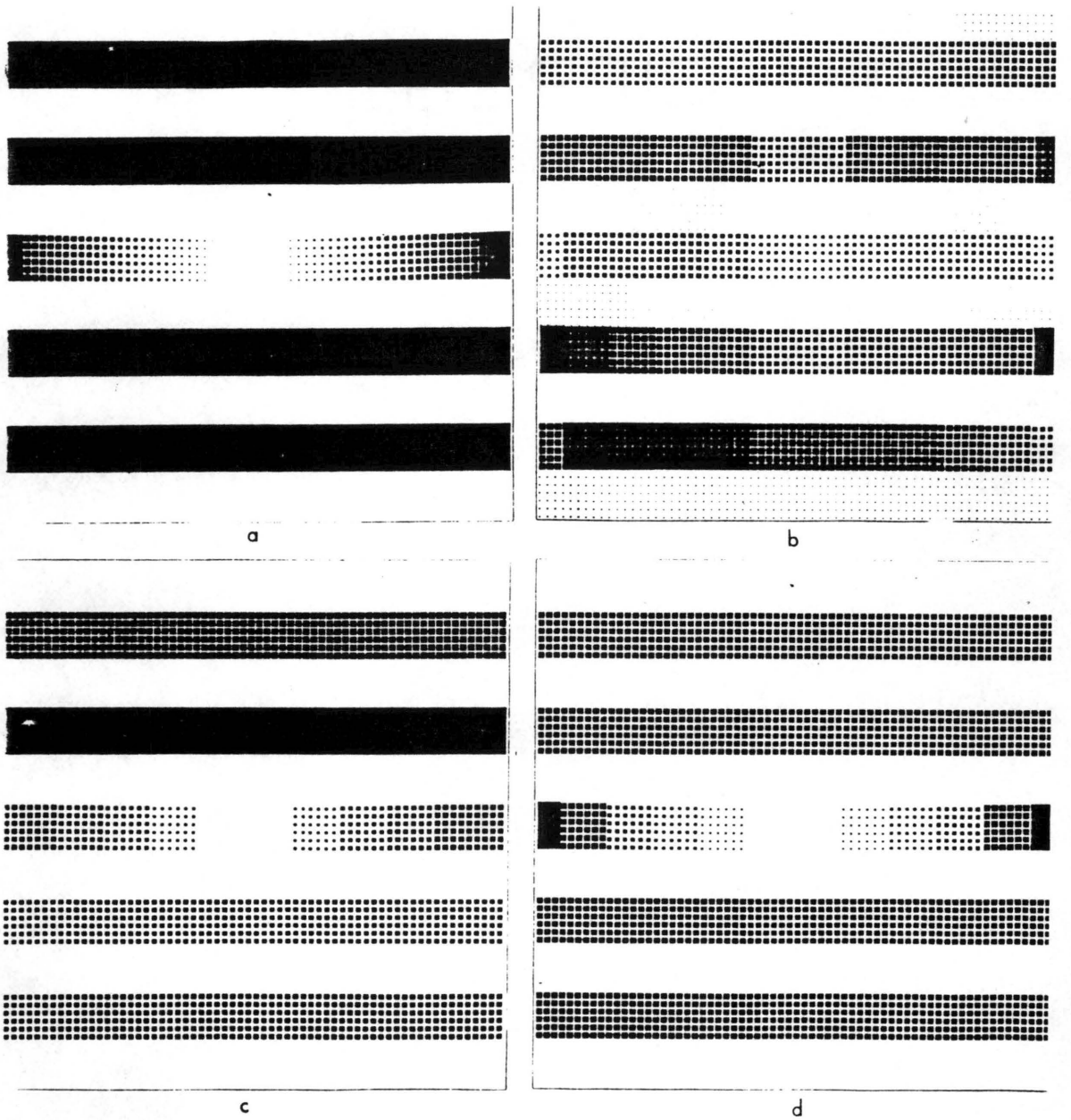

Figure 46. Solutions to the transitional zone model used in a priori information

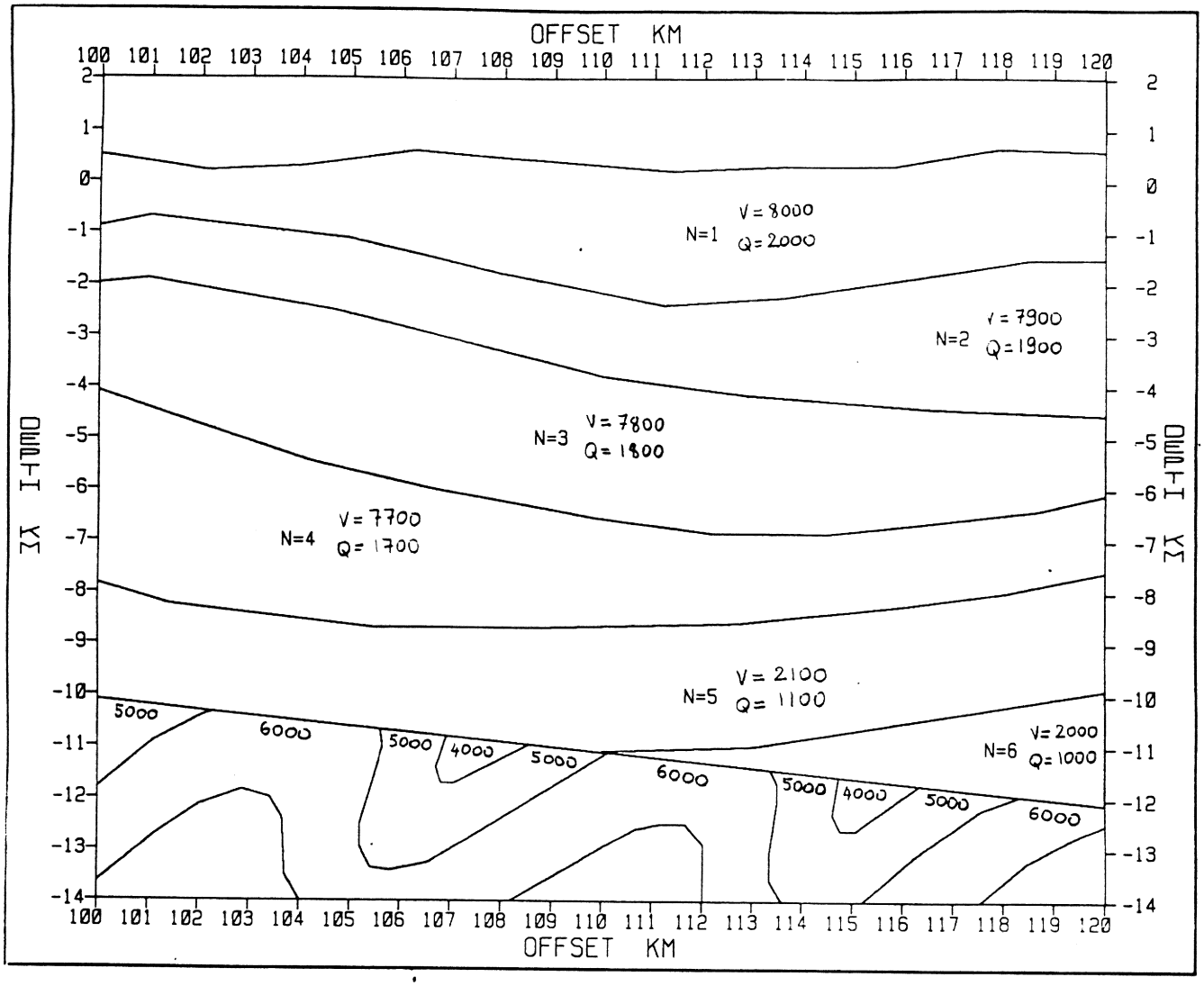

Figure 47. Input model and its corresponding physical parameters: :Velocity, Q, and lateral changes in reflectivity. The high values of Q (1000-2000) were used to test the ability of the SVD algorithms to recover 4-5 significant figures, and are not intended to carry geologic significance. If the software can recover 4-5 significant figures, then it will have no trouble in recovering lower (2 or 3 significant figures) values of Q. As is apparent from Figure 50 the high values of Q were successfully recovered.

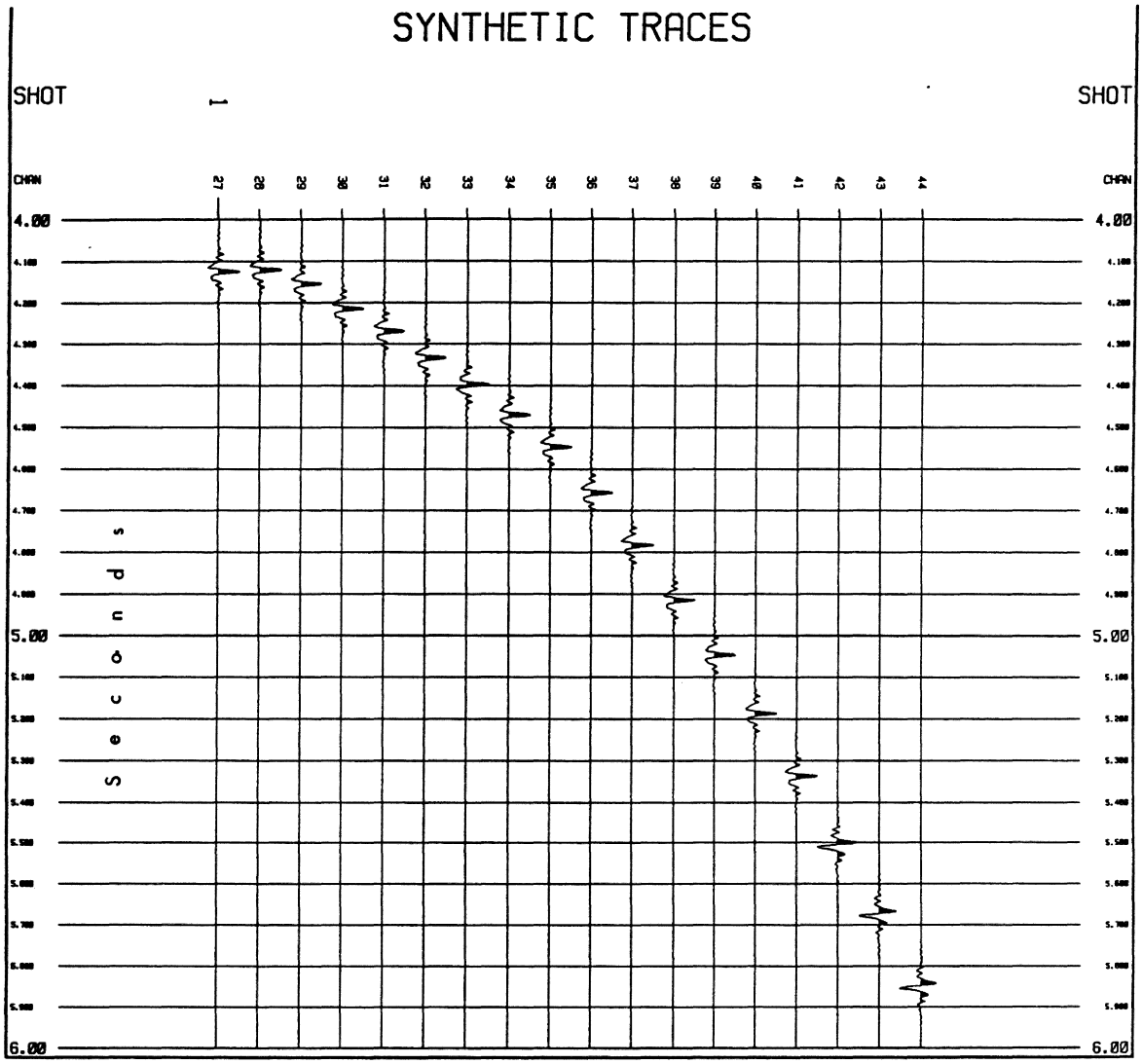

Figure 48. Synthetic seimogram: Traces generated from the synthetic model shown in Figure 47. Notify the occurrence of the critical angle between channels 41 and 42.

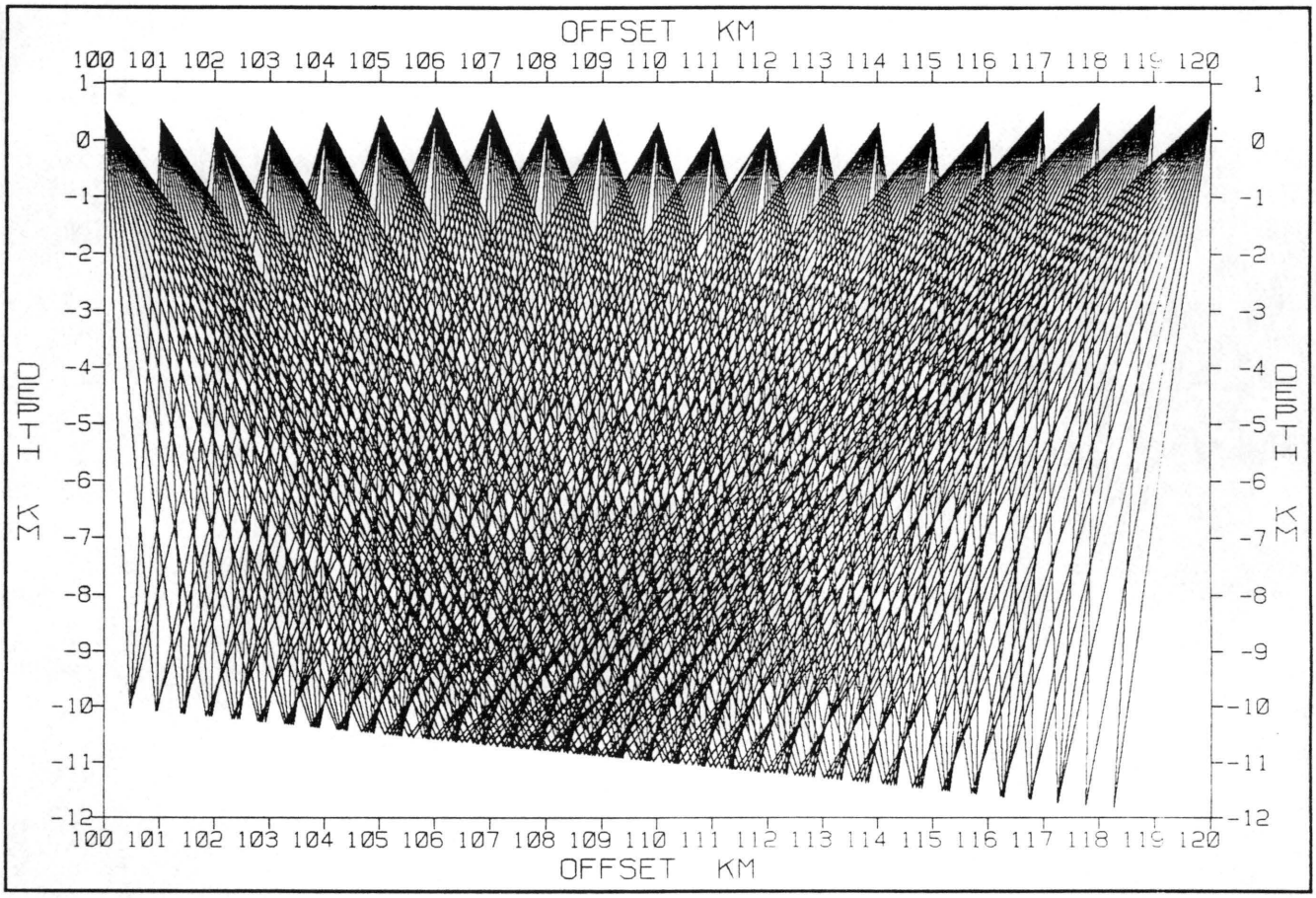

Figure 49. Seismic ray trace coverage of the synthetic model

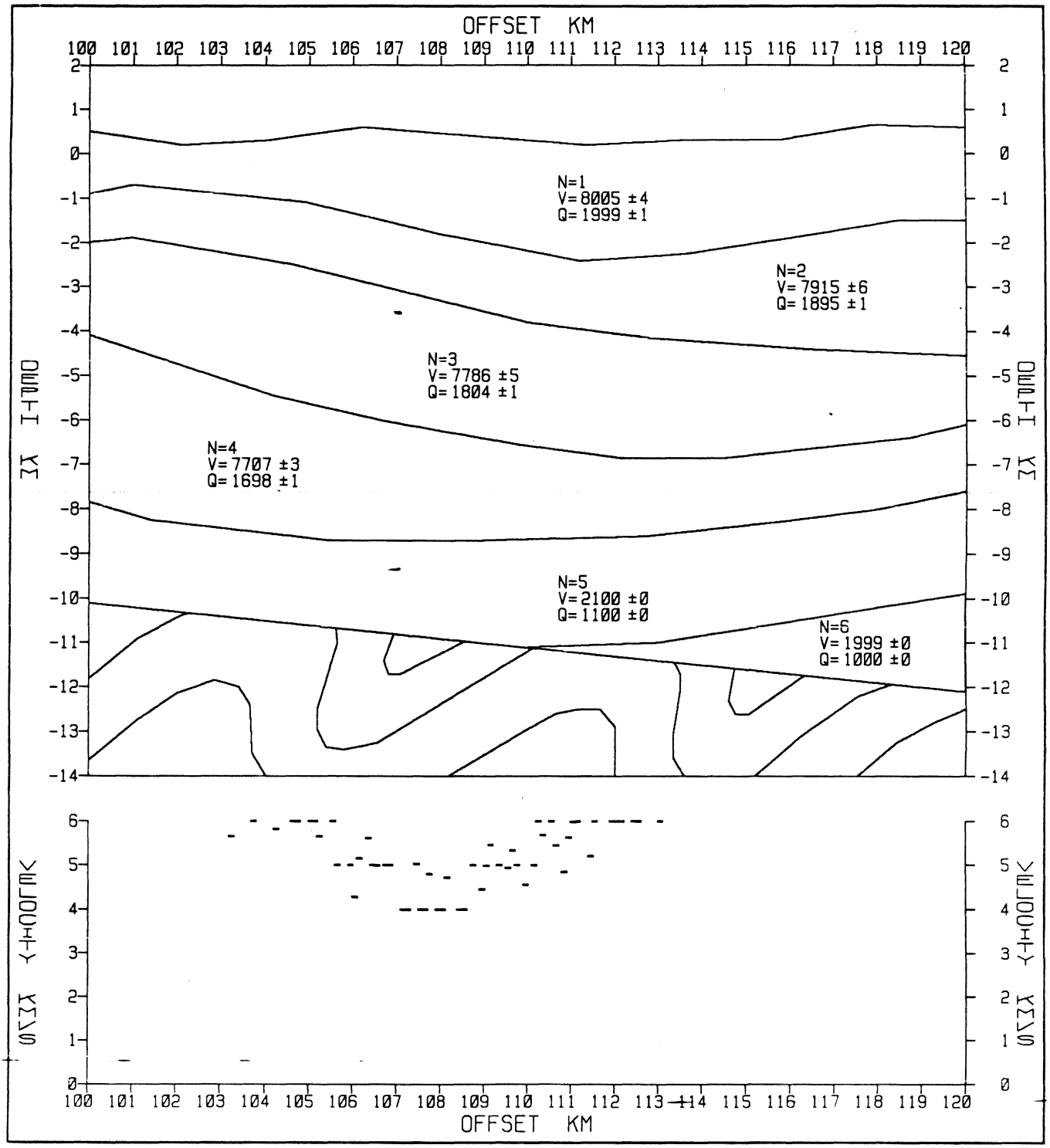

Figure 50. Solution to the synthetic model: Compare these solutions with the input data of Figure 47.

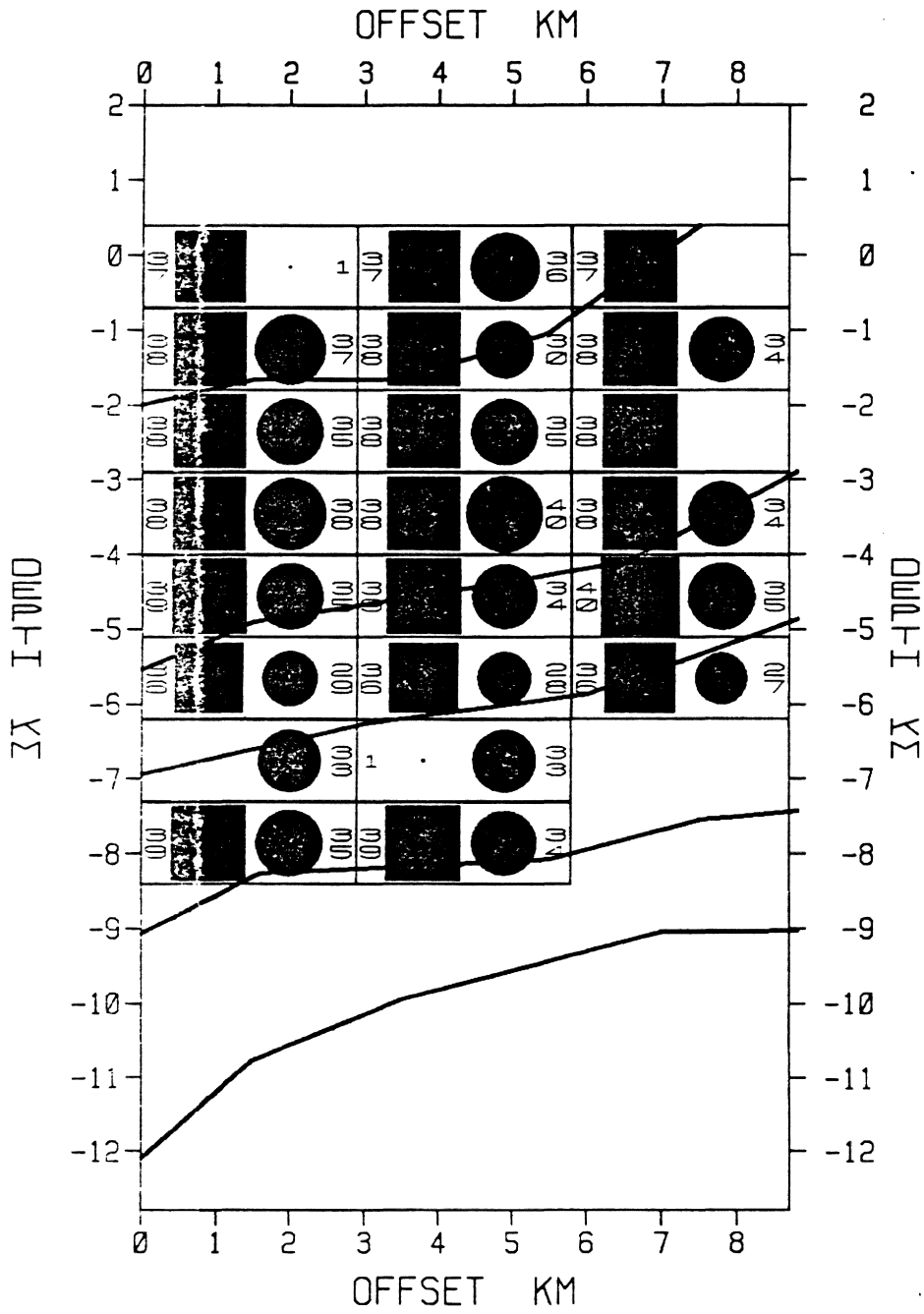

Figure 51. Reflector 4 segment 2 using amplitude only: Solutions obtained from SVD techniques using rectangular motifs

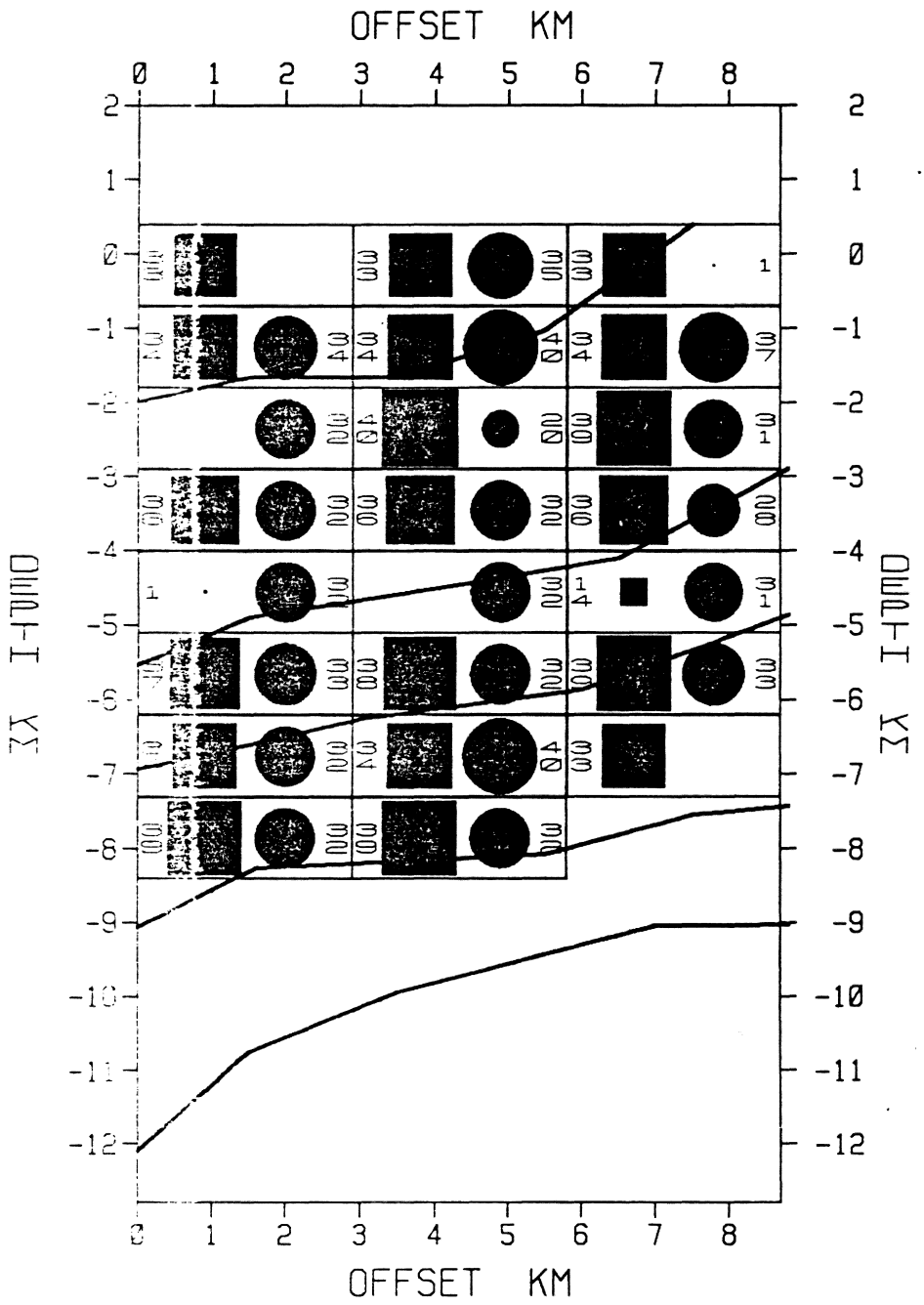

Figure 52. Reflector 4 segment 2 using phase only: Solutions obtained from SVD techniques using rectangular motifs

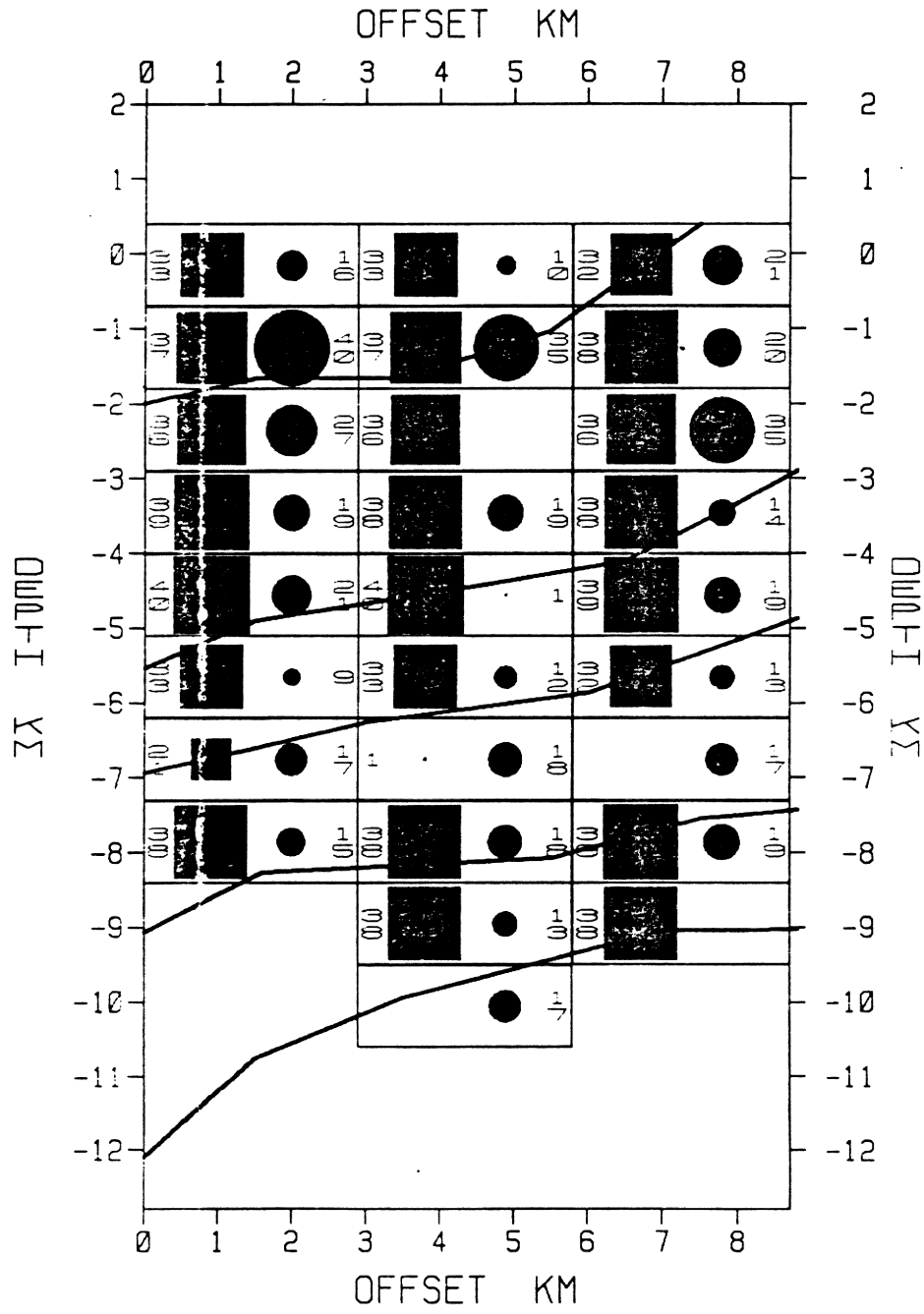

Figure 53. Reflector 5 segment 3 using amplitude only: Solutions obtained from SVD techniques using rectangular motifs

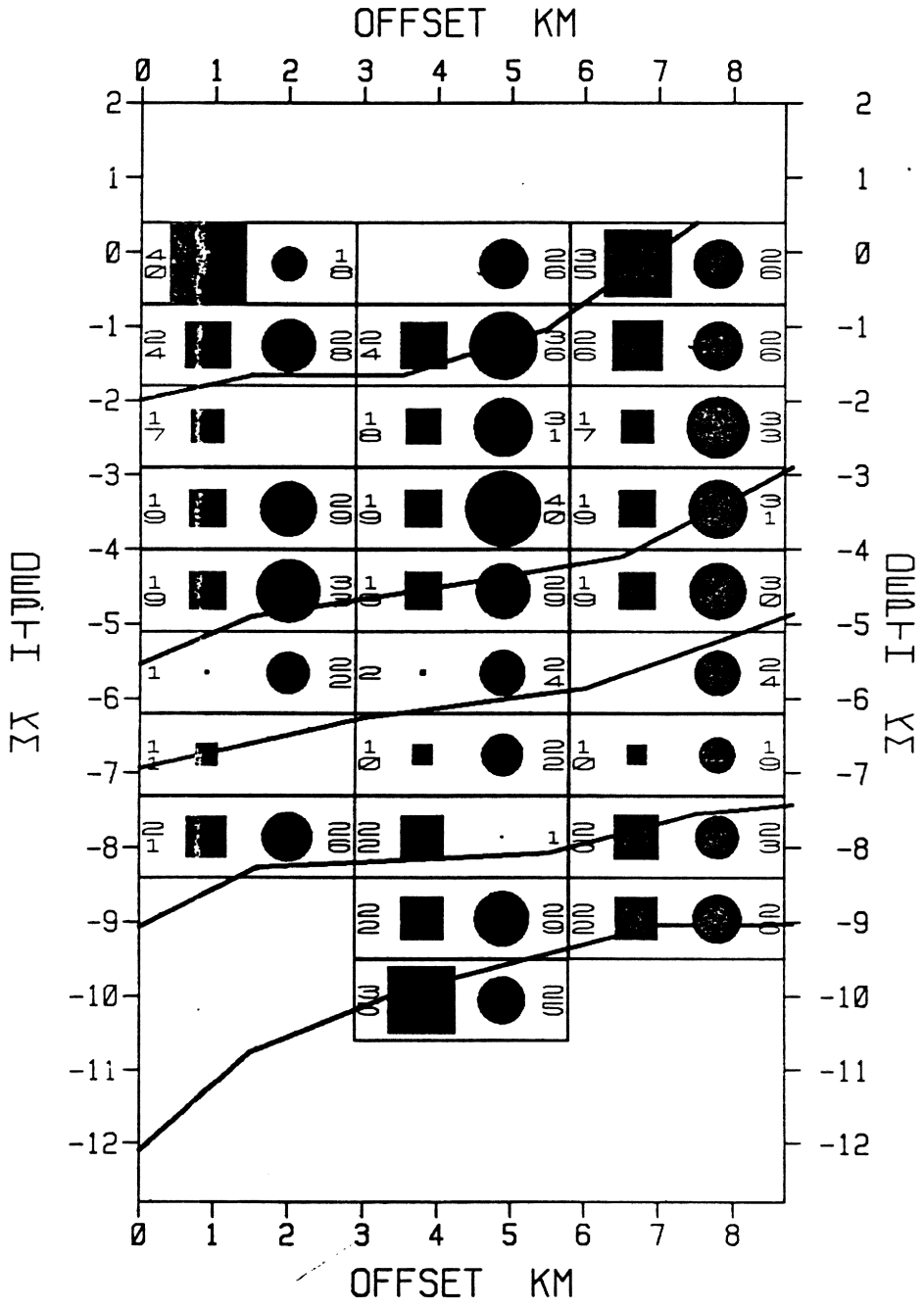

Figure 54. Reflector 5 segment 3 using phase only: Solutions obtained from SVD techniques using rectangular motifs Note the recovery of 5-7 km low-velocity, low-Q zone from amplitude techniques (Figure 53) and phase techniques (this Figure).

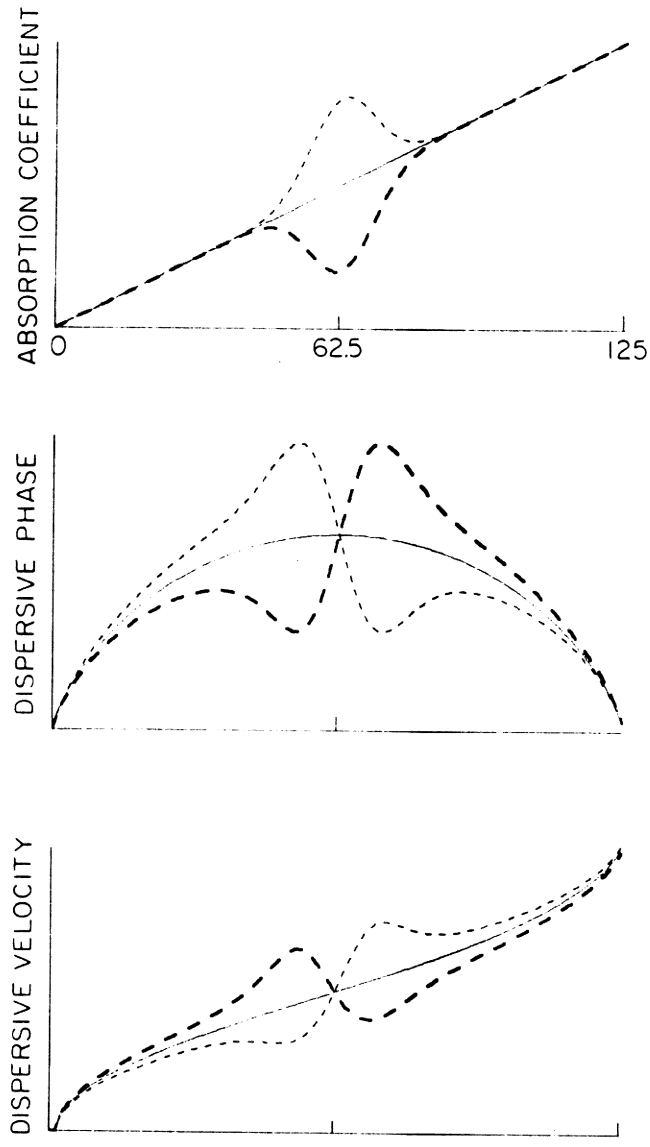

Figure 55. Effect of positive and negative hump: Note that maximum and minimum of the humps on the absorption coefficient curve are aligned with the inflection points on the dispersive phase and dispersive velocity curves. Observe the deviations of the humped curves from the reference (solid thin line) curves.

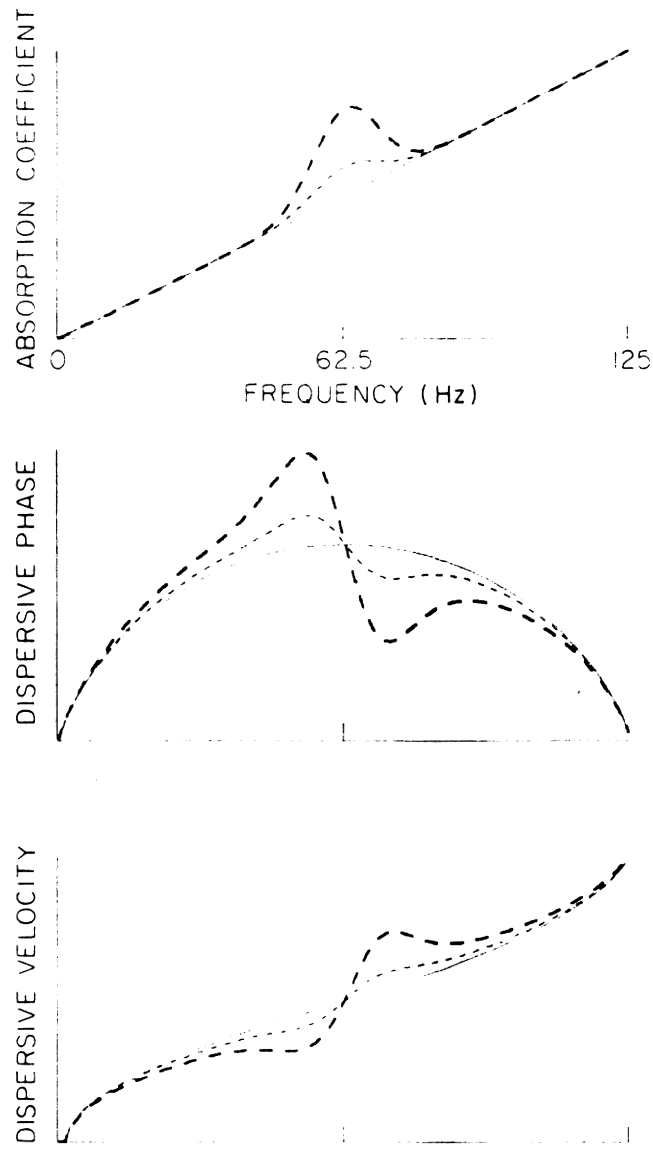

Figure 56. Effect of the magnitude of the hump.

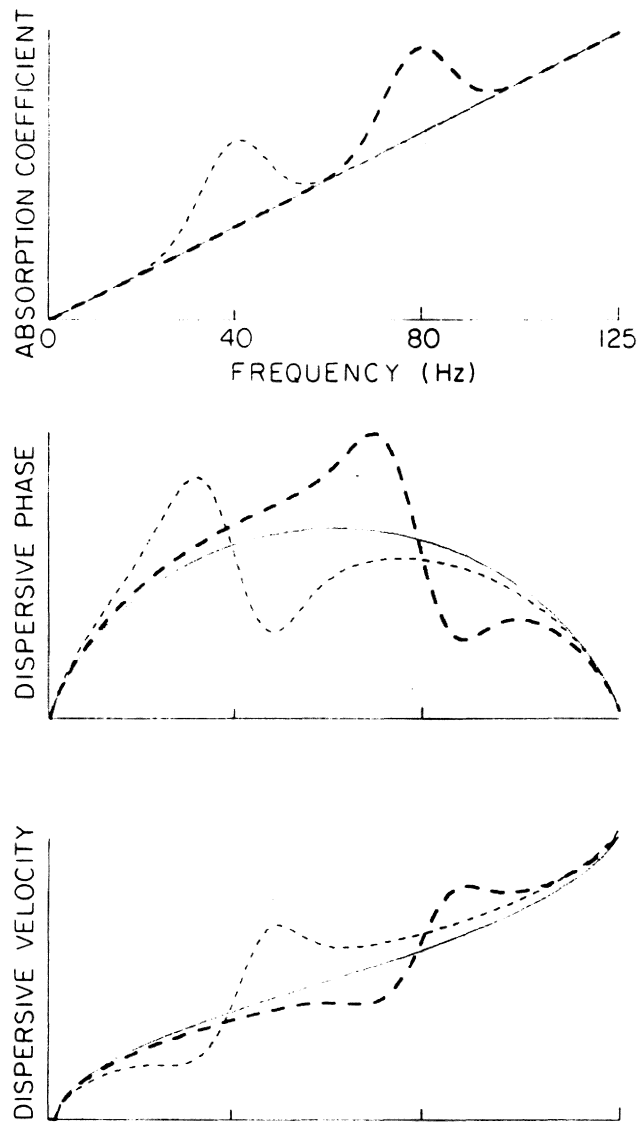

Figure 57. Effect of the location of the hump along the frequency axis.

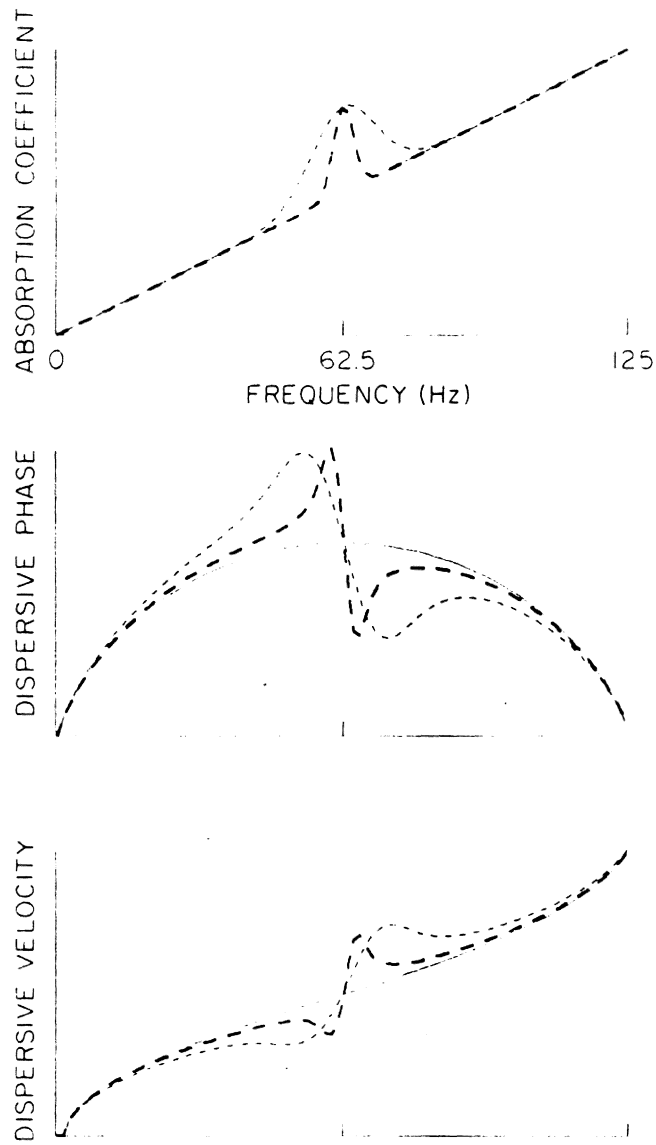

Figure 58. Effect of the width of the hump.

The vita has been removed from the scanned document